DUT

DURBAN UNIVERSITY OF TECHNOLOGY

INYUVESI YASETHEKWINI YEZOBUCHWEPHESHE

Green synthesis, characterization, biological and electrochemical studies of indole pyrazole capped nanomaterials

By:

Senzekile Majola

(Reg No. 21512348)

Submitted in compliance with the criteria for a Master's degree in Chemistry at the University of Technology in Durban.

01 February 2021

DECLARATION

I, **Senzekile Majola**, state that the thesis submitted for a Master's degree in Chemistry at the Faculty of Applied Science at the Durban University of Technology is the result of my inquiry and has not been approved in substance for any degree and is not being concurrently submitted for any other degree. All the work was done by the author, except when the work was used as part of the jointly authored publications. The candidate agrees that appropriate credit has been granted within the thesis where reference has been made to the work of others.

Student Name : Senzekile Majola

Supervisor Name : Dr M. Sabela

Co-Supervisor 1: Professor R.M. Gengan

Co-Supervisor 2: Dr. T.R. Makhanya

DEDICATION

Dedicated to my late mother, uThokazi uKamaCwele for her undivided support and love that she has given throughout my studies in both the physical and spiritual world. My mother was never educated but her drive and passion for education have brought me to where I am, without her strong teachings I believe I would have not been the Senzekile that I am today. She may be gone, but I will treasure her teachings forever.

Missing you always

‘You never said I am leaving, you never said goodbye. You were gone before I knew it and only God knows why. A million times I have cried and if love alone could have saved you, you never would have died. In life, I loved you dearly and in death, I love you dearly still, in my heart I hold a special place only you can fill’.

Rest in Peace Thokazi

I dedicate this thesis to her

ACKNOWLEDGEMENTS

I acknowledge the assistance and guidance from different domains of life for the fulfillment of this dream. Foremost, convey my deepest gratitude to God almighty for the wisdom, strength, peace and good health enabled me to tackle this research and all praise is directed to him. For he has said in *Jeremiah 29:11*

"For I know the plans I have for you,

declares the Lord,

plans to prosper you and not harm you,

plans to give hope and a future"

My sincere appreciation, a deep sense of gratitude to my supervisor, and my academic role model Dr. **M.I. Sabela** for his guidance, amazing patience, and endless encouragement throughout my course of study since 2018. Further, I also take this opportunity to express my deepest gratitude to my Co-supervisors Professor **R.M. Gengan** and Dr. **T.R. Makhanya**. I am very grateful for always making time to assist and guide me throughout the project, their shared experience and support is highly appreciated.

My sincere appreciation goes to all the members of the Computational Modelling and BioAnalytical Chemistry (CMBAC) Research Group and Organic Research Group especially to Matshidiso Lephalala, Benni Hloma, Kwanele Kunene, Lydon Nadooi, Thokozani Ndaba, and Luyanda Hlengwa for their constant words of encouragement and willingness to offer a helping hand at all times.

I am forever grateful to my family (Mzuvele Majola, Phelelani Majola, Mthandeni Majola, and Melusi Majola) who have never left my corner with every decision I have taken in my life and for always being my number one supporters. boMchunu boMacingwane ngiYabonga (Thank you).

Lastly, the research has been carried out with financial support from the National Research Fund (NRF).

ABSTRACT

Green nanomaterial synthesis has become more popular and, with the need for greener approaches to counter higher costs and higher energy usage for chemical and physical processes, scientists are searching for cheaper methods of synthesis. The use of plant extracts has been one of the popular methods because they are known to reduce metal ions from their surface. Green synthesized nanomaterials are relatively unstable compared to chemical and physical methods hence new stabilizing agents (indole pyrazole ligands) have been introduced in this study. The nanomaterials are being applied in electrochemical and biological systems, their behavior may not be as efficient as the new capped nanomaterials. Hence, a comparison of capped and uncapped nanomaterials was studied.

Indole pyrazole capped selenium nanoparticles (TRPIDC-CH_3 SeNPs), Indole pyrazole capped silver nanoparticles (TRPIDC-CH_3 AgNPs), and Indole pyrazole capped cadmium sulphide quantum dots (TRPIDC-CH_3 CdSQDs) were successfully synthesized using plant extracts of *allium sativum* cloves, *pelargonium,* and *moringa* leaves, respectively. Green synthesized TRPIDC-CH_3 capped nanomaterials were characterized by UV-vis spectrophotometry, HR-TEM, and FTIR analysis. The results revealed no differences in shape, color, functional groups involved, or wavelength, but an increase in average diameter as compared to uncapped nanomaterials.

Furthermore, green-fabricated synthesized nanomaterials were tested to evaluate their cytotoxicity against MCF-7, A549, and HEK293 cells. The overall cytotoxicity was low: a dose-dependent increase in cytotoxic activity was observed for each of the nanomaterials, as the concentration increased from 50 µg/ml to 100 µg/ml. Interaction of TRPIDC-CH_3 capped and uncapped nanomaterials with human serum albumin (HSA) was investigated under physiological conditions (PBS, pH 7.3) by UV–Vis, and fluorescence. Fluorescence analysis at different temperatures revealed the quenching of HSA. The results showed a single class of binding site and a static (uncapped) and dynamic (TRPIDC-CH_3 capped) quenching mechanism between nanomaterials and HSA.

The thermodynamic results indicated van der Waals forces and hydrogen bonds (uncapped) and hydrophobic interactions (TRPIDC-CH_3 capped) were dominant. Dual enzyme electrode for the indirect detection of adenosine triphosphate (ATP),using a redox probe as a reference peak, was developed by co-immobilization of the enzymes glucose oxidase (GO) and hexokinase (Hex) and nanomaterials. The implementation of a simple electrochemical technique to co-immobilize enzymes on electrode surfaces demonstrates a significant improvement in the sensitivity, reproducibility and ease of fabrication of ATP biosensors. However, the addition of the TRPIDC-CH_3 ligand to QDs affected the surface area and conductive activity of the sensor leading to a decrease in sensitivity and weakening the electrochemical stability of the QDs. The concept proposed provides the technological basis for a new generation of fast, responsive and robust biosensors for the detection of ATP through indirect detection.

Keywords: Adenosine triphosphate (ATP); Indole pyrazole ligand (TRPIDC-CH_3); Selenium Nanoparticles (SeNPs); Cyclic voltammetry (CV); Square wave voltammetry (SWV); Hexokinase (Hex); Glucose oxidase (GO); Human serum albumin (HSA); MTT assay; MCF-7, A549, and HEK293 cells.

TABLE OF CONTENTS

LIST OF TABLES

LIST OF ACRONYMS AND SYMBOLS

A549: Lung cancer cells .....

$AgNO_3$: Silver Nitrate .....

AgNPs: Silver nanoparticles .....

ATP: Adenosine triphosphate .....

$CdSO_4$: Cadmium sulfate .....

CdSQDs: Cadmium sulphide quantum dots .....

CV: Cyclic voltammetry .....

DMEM: Dulbecco's Modified Eagle Medium .....

FTIR: Fourier transform infared spectroscopy .....

GCE: Glassy acrbon electrode .....

HEK293: Human embryonic kidney cells .....

HR-TEM: High resolution Transmission Electron Microscopy .....

HSA: Human Serum Albumin .....

K_2HPO_4: Dipotassium hydrogen phosphate .....

$K_3Fe(CN)_6$: Potassium hexacyanoferrate .....

KH_2PO_4: Potassium dihydrogen .....

MCF – 7: Breast cancer cells .....

MWCNTs: Multi-Walled Carbon Nanotubes .....

Na_2SeO_3: Sodium selenite .....

PBS: Phosphate buffer solution.....

QDs: Quantum dots.....

SeNPs: Selenium nanoparticles.....

SPR: Surface plasmon resonance……

SWV: Square wave voltammetry.....

TRPIDC-CH_3: Indole pyrazole ligand .....

TRPIDC-CH_3AgNPs: Indole pyrazole capped silver nanoparticles.....

TRPIDC-CH_3CdSQDs: Indole pyrazole capped cadmium sulphide quantum dots.....

TRPIDC-CH_3SeNPs: Indole pyrazole capped selenium nanoparticles.....

UV-Vis: Ultraviolet-visible spectroscopy .....

VA: Voltammetry analysis .....

LIST OF FIGURES

LIST OF CONFERENCES AND PUBLICATIONS

Conference

S. Majola, M.Sabela, T.R Makhanya, and R.M Gengan, "Green synthesis of pyrazole based nanomaterials for the development of Adenosine Tri-phosphate (ATP) electrochemical sensor " **Faculty of Applied Sciences Research Day 2019** held in Durban, South Africa on the 11th of November 2019, **Poster Presentation.**

Manuscripts One

Authors: Sennzekile Majola, Myalowenkosi Sabela, Robert M. Gengan, Talent R. Makhanya

Year: January 2021

Title: Enzyme-indole pyrazole capped SeNPs based electrochemical biosensor for sensitive detection of ATP

Status: Submitted

Manuscripts Two

Authors : Sennzekile Majola, Myalowenkosi Sabela, Robert M. Gengan, Talent R. Makhanya

Year : January 2021

Title : Green Synthesis and Biological studies of indole pyrazole capped Cadmium Sulphide Quantum Dots

Status : In preparation

CHAPTER 1: INTRODUCTION

This chapter provides details about green chemistry and the role it plays in the green synthesis of nanomaterials using plant extract since plants are known to reduce certain metal ions. We also discuss the significance of plants such as *Allium sativum* (Garlic), *Pelargonium graveolens,* and *Moringa oleifera Lam* which will be used to synthesize new nanomaterials (SeNPs, AgNPs and CdSQDs) that will be capped using pyrazole ligand and its application study in the electrochemical determination of Adenosine triphosphate (ATP), and spectroscopic investigations on the interaction between nanomaterials and protein (HSA), in comparison to the uncapped nanomaterial. This chapter also presents the overall aim and objectives, followed by an outline of the thesis.

1.1 Green chemistry

Green Chemistry is the application of chemical expertise and information to limit or remove the use or generation of dangerous compounds during the preparation, manufacture and use of chemicals to minimize threats to human health and the environment (de Marco *et al.* 2019). It is important to establish a clean synthetic approach ('green chemistry') to obtain nanomaterials aimed at various applications in order to pursue an environmentally friendly space. The eco-friendly solvent system, reducing and capping agent are known to be three essential features for a green synthesis (Zhang *et al.* 2010). Green synthesis is becoming increasingly popular, and with the need for greener methods to counter higher costs and higher energy requirements of chemical and physical processes.

Conventional approaches for nanomaterial synthesis usually require dangerous reductants, such as sodium borohydride or hydrazine, which also contain unsafe by-products. Greener routes have been studied for more than a decade to reduce the environmental effects of nanomaterials synthesis. The principles of green chemistry were proposed by Anastas and Warner, who established 12 principles (Figure 1.1) defining green chemistry (Anastas *et al.* 1998). The three key principles for the preparation of nanomaterials in a green synthesis approach are the preference of a solvent medium ideally water, an environmentally safe reducing agent and a non-toxic material for stabilization (Rauwel *et al.* 2015). Synthesis processes should be

conducted close to ambient temperature and pressure and under neutral pH in which to be energy efficient.

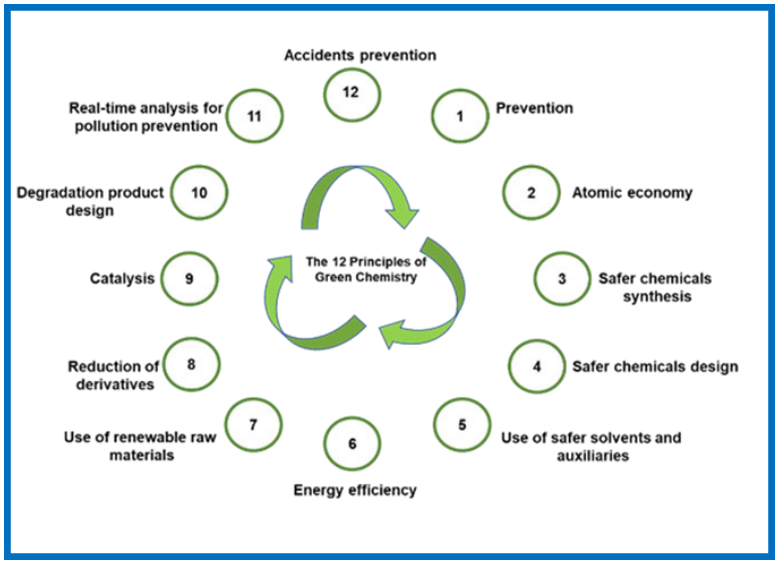

Figure 1.1: 12 principles of green chemistry by Anastas and Warne.

1.2 Plants

Plants are sources of many biologically active compounds that are being used in pharmaceutical, agricultural, and cosmetics industries (Machalova *et al.* 2015). Plants play important part in the development of vital environmental services. Without plants, humans and other living organisms cannot live in a way living should be. Plant extracts have been frequently used in medicine, food, nanomaterials synthesis, and biosensing to name a few, and offer stark advantages over other biomolecules (protein, enzyme, peptide, and DNA) (Ocsoy *et al.* 2018). Plants are known to reduce metal ions from their surface and their metabolites such as sugars, alkaloids, terpenoids, phenolic acids, polyphenols, flavonoids, and proteinsplay a vital role in the bioreduction of metal ions and capping of resulting nanomaterials (Makarov *et al.* 2014).

As a result, nanomaterial aggregation could be effectively prevented and post-surface alteration could be easily completed. Zhang and co-worker showed that the use of plant extract overshadows microorganisms in nanomaterial biosynthesis (Zhang *et al.* 2010). Therefore, the approach on based plant extracts are a green alternative to nanomaterials synthesis. The green synthesis of nanomaterials using plant extracts is advantageous because it is cost-effective, environmentally friendly, short

development, and production times. In this study plant extracts of *Allium sativum*, *Pelargonium graveolens,* and *Moringa Olieife* are used to synthesize nanomaterials.

1.2.1 Allium Sativum (Garlic)

Allium sativum (Garlic) is a plant species that is native to north-eastern Iran and Central Asia. It is a common vegetable that belongs to the *Allium* family, and is commonly used in many countries and cultures considering the potential health benefits and flavor (Phan *et al.* 2019). In countries such as the United States, the United Kingdom, Australia, and Germany *Allium sativum* is commonly used as herbal medicines. In the Mediterranean, it is economically important because it is the main agricultural product (Abbas *et al.* 2019; Chan *et al.* 2019). The *Allium sativum* plant's bulb (Figure 1.2) is the most commonly used part of the plant, is normally divided into numerous fleshy sections called cloves. *Allium sativum* cloves either cooked or raw is used for consumption and medicinal purposes. They have an overpowering, spicy flavor that mellows and sweetens noticeably with cooking (Abbas *et al.* 2019; Phan *et al.* 2019).

Figure 1.2: *Allium sativum* cloves.

1.2.2 Pelargonium graveolens

Pelargonium graveolens (Figure 1.3) which is commonly called *rose-scented geranium* or *rose geranium* is an aromatic plant that belongs to the *Geraniaceae* family, and is highly used in sanitary products, in cosmetics, and in food preparation because of their terpenoid-rich essential oil (Mohammadlou *et al.* 2017; Bergman *et al.* 2019). Most *Pelargonium* species are native to South Africa and neighboring

countries and have approximately 280 species with a wild variety of floral and leaf morphology variants, with approximately 30 species that are odoring, like *Pelargonium graveolens* (Blerot *et al.* 2018). Amongst the scented *Pelargonium* species, the *Pelargonium graveolens* is the most characteristic cultivars and it is often used to replace the expensive *Rosa damascena* essential oil when a hybrid with the *Pelargonium roast* (Blerot *et al.* 2018).

Figure 1.3: *Pelargonium graveolens* leaves.

1.2.3 Moringa Oleifera lam

Moringa oleifera Lam also known as horseradish tree, drumstick tree or tree of life is a drought-resistant tree that is native to the sub-Himalayan tracts of India, it belongs to the *Moringaceae* genus and it is the most cultivated among the species of the *Moringaceae* family (Oyeyinka *et al.* 2018). Almost all parts of this tree have been found to be very useful. The tree trunk is used to make gums, leaves (Figure 1.4) as forage, flower nectar in honey, and powdered seeds for water purification (Oyeyinka *et al.* 2018; Zhao *et al.* 2019). *Moringa Oleifera* leaves has been used as an alternative food source to fight malnutrition, and are reported to contain substantial amounts of vitamin A, C, and E, as well as appreciable amounts of proteins, iron, total phenols, magnesium, calcium, manganese, copper, and potassium (Hekmat *et al.* 2015; Tiloke *et al.* 2019). The flowers and fruits of *Moringa Oleifera* have also been found to contain appreciable amounts of carotenoids (Saini *et al.* 2014).

Figure 1.4: *Moringa Oleifera Lam* leaves.

1.3 Nanomaterials

The synthesis of nanomaterials using various plant materials is an emerging field of nanotechnology, which is critical for preventing the use of harmful chemicals and promotes the production of an eco-friendly technique. Nanomaterials (1-100 nm) of varying shapes and sizes have drawn significant interest due to their unique electronic, chemical and optical properties comparable to bulk materials (Kumar *et al.* 2017). Nanotechnology provides expanded research, such as reproductive science and technology, conversion of agriculture and food waste to energy and other valuable by-product through chemical sensors, disease prevention, cleaning of water, and treatment in plants using various nanocides (Siddiqui *et al.* 2015).

Nanoparticles are a broad class of materials of one dimension less than 100 nm, exhibiting characteristic colors and properties of different sizes and shapes that can be used in bioimaging applications. (Khan *et al.* 2019). Nanoparticles possess good physicochemical characteristics that cannot be found in a single molecule and a bulky metal. They have gained significant interest due to their remarkable chemical, physical and biological properties and are used in fields such as food processing, biolabelling and medicinal drugs (Mohammadlou *et al.* 2017).

Quantum dots (QDs) are fluorescent semiconductor nano-crystals with a normal size range of 1 to 12 nm. These types of nanomaterials have distinct tunable electrical and optical properties attributable to quantum containment effects such as high photostable, high quantum yield large absorption, long fluorescence life, and narrow and size-dependent emission spectra (Borovaya *et al.* 2015; Qin *et al.* 2018).

According to these unique characteristics, QDs have gained significant attention in the fields of bioimaging, biosensors, solar power generation and biomedical science, and periodic table groups II-VI have been used to create various forms of QDs, such as ZnS, CdS, CdSe, CdTe and PbS (Al-Shalabi *et al.* 2016; Jacob *et al.* 2017). In this study, the following nanomaterials were synthesized via a green method using plant extracts, Indole pyrazole capped selenium nanoparticles (TRPIDC-CH_3 SeNPs), Indole pyrazole capped silver nanoparticles (TRPIDC-CH_3 AgNPs), and Indole pyrazole capped cadmium sulphide quatum dots (TRPIDC-CH_3 CdSQDs).

1.4 Indole-Pyrazole ligand

Pyrazoles are five-membered aromatic heterocycles containing two adjacent nitrogen atoms. This platform is an important template for the creation and design of different medicinal drugs as it exhibits many biological properties such as hypoglycemic, analgesic, antipyretic, antibacterial, anti-inflammatory, anti-hyperglycemic and sedative-hypnotic activity (Dadiboyena *et al.* 2011). Pyrazoles are available from natural sources, but synthetic molecules dominate the pharmaceutical industry because they can be synthesized from basic substrates.

The problem with extracting pyrazoles from living organisms is their limited capacity to metabolize compounds that contain two nitrogen atoms adjacent to each other. The chemistry of fused pyrazoles has drawn considerable interest due to their pharmacological significance in the treatment of numerous health problems. Thus, one of our co-authors developed a method to synthesize indole pyrazole ligands (Makhanya 2019). In this research, we used the TRPDC-CH_3 ligand (Figure 1.5) and coated it with nanomaterials in the form of a capping agent and observed its behavior.

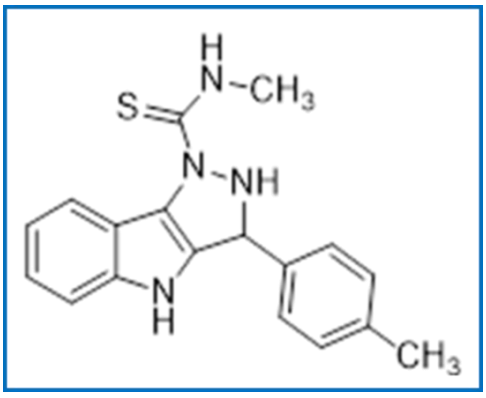

Figure 1.5: Structure Indole-Pyrazole ligand (TRPIDC-CH_3) used.

1.5 Adenosine triphosphate (ATP)

Adenosine triphosphate (ATP) is a multifunctional nucleotide, which is produced during cellular respiration and photosynthesis, and it acts as a primary energy source in living organisms (Freitas *et al.* 2017; Wang *et al.* 2018; Manjubaashini *et al.* 2019; Peteu *et al.* 2020). ATP plays an essential role in cellular metabolism, biosynthesis, and the regulation of biochemical pathways in DNA replication, cell physiology, and transcription, (Wang *et al.* 2018). It also act as a motioning mediator in the cascade for the modulation of the central and peripheral nervous systems.

Studies have shown that ATP can be used as an indicator for viability, proliferation, and cell injury (Zhu *et al.* 2018; Manjubaashini *et al.* 2019). ATP is a significant indicator in the pathogenies of some diseases such as hypoglycaemia, Alzheimer's disease hypoxia, ischemia and Parkinson's disease. Therefore, the detection of ATP is very useful for monitoring in the biochemical studies, clinic diagnosis, food quality control, and environmental analyses (Lu *et al.* 2015; Wang *et al.* 2018). Electrochemical detection of ATP will be studied by immobilizing the nanomaterials onto a bare glassy carbon electrode.

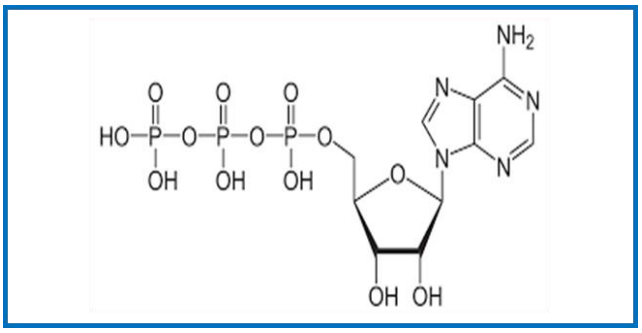

Figure 1.6: Structure of Adenosine triphosphate (ATP).

1.6 Electrochemical biosensors

Electrochemical sensors and biosensors are effective analytical instruments that are low-cost ,lightweight and self-contained. Advanced functional nanomaterials have a tremendous potential to boost both selectivity and sensitivity by tuned signal amplification. The design of nanomaterials with minimal toxicity and environmental effect is also needed for realistic applications in real-world biomedical applications. The synthesis of metal nanoparticles, bio-functional nanoparticles and nanocomposites or nanohybrids have intrigued the nature of biosensor.

(Maduraiveeran *et al.* 2018). Electrochemical techniques counteract the drawbacks of simple techniques since it is possible to create a biosensor that is quicker in reaction time, low cost, responsive and selective to the specific compound of interest. The goal is to create an electrochemical biosensor with excellent catalytic activity and conductivity by immobilizing nanomaterials on a bare electrode.

Nanomaterials based nanosensors provide significant advantages, including improved chemical, physical and biological properties. They have a higher surface-to-volume ratio, which makes for higher sensing responses as well as improved optical, magnetic and electrical properties. Nanomaterials possess major advantages over macro-scale materials for biological and biomedical applications (Maduraiveeran *et al.* 2018). Due to the growing importance of biosensors, the choice of biological recognition device/element/material is essential for the creation of a novel biosensor. Biosensing material has to be stable under the operation and storage conditions of the biosensor and there are various forms of nanomaterials, such as quantum dots, nanoparticles and carbon nanotubes, which can be used for biosensor development (Manjubaashini *et al.* 2019).

1.7 Human Serum Albumin (HSA)

Human Serum Albumin (HSA) is a multi-domain protein with a helical structure (Figure 1.7) with a molecular weight of approximately 66 kDa (585 amino acid residues) and a blood plasma protein concentration of roughly 35-50 mg/ml, making it an abundant protein in the blood (Chugh *et al.* 2019). HSA is an essential carrier protein in the human circulatory system and the key function of HSA is the transport and synthesis of bioactive molecules such as hormones, fatty acids, metals, vitamins and pharmaceuticals, it is used as a reference protein for numerous biochemical, biophysical and physicochemical research (Prasanth *et al.* 2017). HSA is known for its unique ligand-binding capacity due to its multiple hydrophobic binding sites which bind particularly medium-sized hydrophobic compounds (Khulu 2015). Spectroscopic methods have been used to investigate the interaction, such as FTIR, cyclic voltammetry (CV), UV-Visible and fluorescence spectroscopy and they are powerful tools for investigating the intra or intermolecular interactions in bio-macromolecules (Rezanejade Bardajee *et al.* 2017).

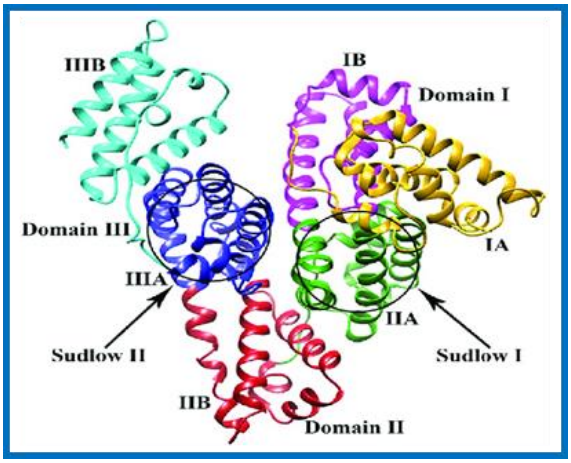

Figure 1.7: Helical structure of Human Serum Albumin (HSA)

1.7.1 Nanomaterial-Protein binding

HSA is noted for its extensive ligand-binding proteins, which can be both endogenous and exogenous. Complex interactions between nanoparticles and biological systems are required to ensure the safe and effective use of nanoparticles in biomedical applications. It is important to ensure the biocompatibility of nanoparticles developed (Chakraborti *et al.* 2013). When the nanoparticles enter into the biological fluids, they interact with the plasma proteins, and a protein corona is formed around the nanoparticles. The protein corona it significant roles in modulating nanoparticles toxicity and mobility, and interactions can alter the normal functioning and conformation of the proteins leading to unexpected biological reactions (Prasanth *et al.* 2017).

Human serum albumin interacts with the bulk of small molecules primarily by electrostatic, followed by hydrogen, hydrophobic, van der Waals and covalent interactions. In recent years, the emerging role of protein-nanomaterial interactions has been thoroughly studied in the field of nanomedicine and nanotoxicity, as nanomaterials are known to change the structure and functions of proteins (Mahanthappa et al. 2018). Such studies can provide insight into the definition of the effect of nanomaterials on proteins that play a pivotal role in biomedical applications. We will therefore carry out a spectroscopic investigation of the interaction between TRPIDC-CH_3 capped nanomaterials and HSA protein.

1.7.2 Binding sites and Domains of HSA

HSA consist of three similar domains I, II, and III which are further divided into two subdomains each A and B. The three domains design provides a variation of binding sites and the flexibility of its structure allows it to adapt readily to ligand (Chugh *et al.* 2019). The main ligand binding sites of HSA are located in the hydrophobic subdomains II-A and III-A, and subdomain III-A has a higher binding affinity (Prasanth *et al.* 2017). They are two Sudlow drug binding sites I and II, where Sudlow's I drug binding site is located in subdomain II-A and binds bulky heterocyclic anions such as warfarin. While Sudlow's II drug binding site is located in subdomain IIIA, it binds aromatic carboxylates like ibuprofen (Khulu 2015; Chugh *et al.* 2019).

1.8 Problem statement

Nanomaterials can be synthesized by chemical and physical methods, however, these methods are expensive, labor-intensive, and potentially hazardous to the environment and living organisms. Recently, there is a greater thrust towards green methods because they are eco-friendly, cost-effective, and involve a single-step synthesis. However, green synthesized nanomaterials are relatively unstable compared to chemical and physical methods. Hence new stabilizing agents are being sought after. Although nanomaterials are being applied in electrochemical and biological systems, their behavior may not be as efficient as the new capped nanomaterials. Hence a comparison of capped and uncapped nanomaterials will be studied.

1.9 Aim and Objectives

Aim

The aim is to synthesize indole pyrazole capped nanomaterials (AgNPs, SeNPs and CdSQDs) using plant extracts (*pelargonium graveolens*, *Allium sativum,* and *moringa oleifera*) and evaluate their biological and electrochemical properties in comparison to the uncapped nanomaterials.

The objectives are to:

- Prepare *moringa oleifera* leaf, *allium sativum cloves* and *pelargonium graveolens* leaf extracts.
- Characterize the plant extracts by UV-Vis, FTIR, and perform phytochemical analysis.
- Synthesize AgNPs, SeNPs, and CdSQDs using extracts of *pelargonium graveolens*, Allium sativum, and *Moringa oleifera,* respectively, *and* capped with an indole pyrazole ligand.
- Characterize the nanomaterials by UV-Vis, HR-TEM, and FTIR.
- Evaluate the biological and electrochemical activities of the nanomaterials

1.10 Thesis Outline

This thesis is divided into five chapters. Following the introduction (**Chapter 1**), further chapters in this thesis are divided as follows:

Chapter 2: Literature Review

The chapter describes the literature reviews of the study including an insightful understanding of green synthesis, Adenosine triphosphate (ATP), electrochemical biosensors, and protein binding.

Chapter 3: Methodology

A description of the materials and methods used in the design of the experimental works is presented in this chapter. The experimental study including, green synthesis using plant extract, cytotoxicity activity, protein interaction, fabrication of modified electrode, and characterization studies are presented.

Chapter 4: Results and Discussion

A discussion of the results obtained from the experimental methods is presented here. The assessment of the pyrazole capped and uncapped nanomaterials are discussed here.

Chapter 5: Concluding Remarks and Future Perspectives

A summary of the overall conclusions is presented in this chapter.

References

The last chapter comprises of a list of references cited throughout this thesis

CHAPTER 2: LITERATURE REVIEW

This chapter provides literature review of the study including an insightful understanding of plant extracts and nanomaterials used. It gives a brief overview of the applications of the green synthesized nanomaterials, the electrochemical determination of ATP by immobilizing the nanomaterials onto a bare electrode, its historical aspect. The interaction studies of the nanomaterial and Human serum albumin protein are presented here which can be helpful in drug delivery.

2.1 Plants used in this study

Green chemistry is an approach that has paved the way towards sustainable processes by minimizing the waste produced, usage of non-toxic starting materials, being more cost-effective and environmentally friendly. The use of plants in the process of nanomaterials synthesis is more beneficial than other processes since the nanomaterials are produced extracellular (Nabikhan et al. 2010). Plant extracts have been a source of inspiration for designing complex nanomaterials with high surface area and potent applications in commercial products, biosensors, catalysis, as well as environmental technologies (Sharma et al. 2016). *Allium sativum*, *Pelargonium graveolens,* and *Moringa Olieife* were used to synthesize TRPIDC-CH_3 SeNPs, TRPIDC-CH_3 AgNPs, and TRPIDC-CH_3 CdSQDs, respectively.

2.1.1 Allium Sativum

Allium sativum is important because of its therapeutic function and its biological activities such as antibacterial, antifungal, and antioxidant properties (Shrestha *et al.* 2016; Rose *et al.* 2018). The biological and health properties of allium sativum are derived from its polyphenols, flavonoids, saponins, Maillard reaction, enzymes, and organosulfur compound (vinyl dithiins, ajoene, diallyl polysulfides, S-allyl cysteine, alliin) (Chen *et al.* 2018; Rose *et al.* 2018). The sulfur-containing compounds are suggested to be responsible for the pungent aroma, are the main compounds responsible for its physiological effects (Abbas *et al.* 2019). *Allium sativum* has been used as traditional medicine for centuries to treat diarrhea, tumor, constipation, and aches. In modern times, the consumption of *Allium sativum* reduces the risk of type 2 diabetes, the risk of cardiovascular disease, and the risk of developing various cancers (Rose *et al.* 2018; Abbas *et al.* 2019).

Many studies have reported the synthesis of different nanomaterials using different parts of the *Allium sativum* plant. Modi *et al* synthesized zinc oxide nanoparticles (ZnONPs) with *allium sativum* skin extract having an average size of 7.77 nm (Modi *et al.* 2019). Anu *et al* synthesized SeNPs using *allium sativum* cloves and tested their cytotoxicity, the nanoparticles showed eco-friendly features and limited cytotoxicity if compared with chemically synthesized selenium nanoparticles (Anu *et al.* 2017). AgNPs synthesized using an aqueous extract of *Allium sativum* were found to have a significant antibacterial activity by Saha *et al* (Saha *et al.* 2019).

Satgurunathana *et al* reported that SeNPs synthesized from *allium sativum* cloves can be feed to the freshwater prawn Macrobrachium rosenbergii post-larvae and its improved the survival, growth, and concentrations of biochemical constituents in M. rosenbergii post-larvae (Satgurunathan *et al.* 2017). Ryavanaki *et al* synthesized sensitive detection of lead Ions (Ryavanaki *et al.* 2020). Amatya *et al* bio-synthesized of copper nanoparticles (CuNPs) using *allium sativum* cloves extract to investigate antibacterial activity (Amatya *et al.* 2020). Karunanithy *et al* reported the bio-synthesis of Zn doped AgTe materials with the help of *allium sativum* skin powder (Karunanithy *et al.* 2019).

2.1.2 Pelargonium graveolens

The *Pelargonium graveolens* is being used for its antimicrobial activity in the food industry and the medical field because of its antibacterial, antifungal, and antioxidant activity (Machalova *et al.* 2015; Hamidpour *et al.* 2017). Traditionally, the plant has been used to treat wounds, colds, and sore throats, inflammation, heavy menstrual flow, insomnia, asthma, nausea and vomiting (Hamidpour *et al.* 2017). Hydrosols of *Pelargonium graveolens* are still used as a remedy for the treatment of stomach ulcers, fatigue, breast inflammation, genital infection, and colds. The essential oils and organic extracts of the plant are used in pharmacological and food industries for their bioactive substance (Ennaifer *et al.* 2018). Besides terpenoid, the Pelargonium graveolens is reported to contain substantial amounts of flavonoids, alkaloids, phenolic acids, total phenols, and tennis (Pandian *et al.* 2013; Machalova *et al.* 2015; Mohammadlou *et al.* 2017; Ennaifer *et al.* 2018).

Many studies have reported the synthesis of different nanomaterials using *pelargonium graveolens* leaf extract, mainly for AgNPs. Mohammadlou *et al* reported the hydrothermal synthesis of AgNPs using the *pelargonium graveolens* leaf extract (Mohammadlou *et al.* 2017). Jafarizad *et al* synthesized gold nanoparticles (AuNPs) using *pelargonium* leaf extract and studied in-vitro on the nanoparticles (Jafarizad *et al.* 2015). Fardsadegh *et al* reported SeNPs using *pelargonium* leaf extract, the nanoparticles indicated higher antibacterial activities (Fardsadegh *et al.* 2019b). Vahidi et al synthesized zinc oxide (ZnONPs) nanoparticles using *pelargonium* leaf extract (Vahidi *et al.* 2019). Pawlowska and Sadowski reported the use of pelargonium leaf extract to synthsize copper nanoparticles. (Pawlowska *et al.* 2017).

2.1.3 Moringa Oleifera lam

Moringa Oleifera Lam tree is rich in nutrients such as proteins, fiber, and minerals and it plays a vital role in human nutrition (Oyeyinka *et al.* 2018). Numerous studies have shown the potential use of different parts *of Moringa Oleifera* in food applications such as in making amala, a stiff dough made from yam and plantain flour (Karim *et al.* 2015), soup making (Babayeju *et al.* 2014), yoghurt (Hekmat *et al.* 2015), bread (Chinma *et al.* 2014), and herbal biscuits (Alam *et al.* 2014). *Moringa Oleifera Lam* leaf extract has several properties including antioxidant, anti-inflammatory, anticancer, antifungal, and hypotensive activity (El-bakry *et al.* 2016; Tiloke *et al.* 2019). Due to the phytochemical constituents such as polyphenols, flavonoids, phenolic acids, carotenoids, fatty acids niazirin I and II, niazinin, and niazimicin, traditional healers use the *Moringa Oleifera Lam* leaves and addition of water to heal wounds, and treat headaches (El-bakry *et al.* 2016).

Moringa oleifera is reported to contain tannins, steroids, triterpenoids, flavonoids, saponins, and alkaloids which are known as alternative reducing agents in synthesizing nanomaterials when employing plant extracts (Pratiwi *et al.* 2019). Many authors have reported the use of different parts of the *Moringa oleifera* tree, Seetha *et al* used *Moringa oleifera lam* leaf extract to synthesize AgNPs and copper nanoparticles (CuNPs) (Seetha *et al.* 2020). Kalugendo and Kousalya synthesized AgNPs using the *Moringa oleifera* seed (Kalugendo *et al.* 2019). Aisida et al synthesized iron oxide nanorods using *Moringa oleifera* leaf extract (Aisida *et al.* 2020). Ezhilarasi *et al* reported the synthesis of nickel oxide nanoparticles (NiONPs)

using *Moringa oleifera* leaf extract and NiONPs showed better cytotoxicity and antibacterial activity (Ezhilarasi *et al.* 2016). Matinise et al reported zinc oxide nanoparticles using *moringa oleifera* extract (Matinise *et al.* 2017). Reddy *et al* did microwave-assisted iron oxide quantum dots using *moringa oleifera* leaf extract (Reddy *et al.* 2018).

2.2 Nanomaterials used in this study

Biosynthesis of nanomaterials has received increasing consideration due to the growing need to develop environmentally friendly nanomaterial (Shameli et al. 2012). Biosynthesis of nanomaterials has been proposed as a cost-effective and environmentally friendly way of fabricating nanomaterials. Synthesis of nanomaterials using plant extracts has emerged as an alternative approach. The method is advantageous because it is simple, cost-effective, gives high yields, and is environmentally friendly (Tippayawat *et al.* 2016). Green fabrication of metal and metal oxide nanomaterials using different parts of plants (e.g., flower, leaf, stem, and root) is an innovative part of nanotechnology and they have natural bioreductants and stabilizers, such as alkaloids, carbohydrates, polyphenols, proteins, flavonoids enzymes, and phenolic acids, which are key roles in the green synthesis of nanomaterials (Sheikhlou *et al.* 2020).

2.2.1 Selenium Nanoparticles (SeNPs)

SeNPs displayed numerous advantages, such as high drug loading capacity, low cytotoxicity, enhanced antitumor efficacy, and controlled size. Thus, SeNPs have been used as one pre-eminent antitumor drug delivery vehicle (Xia *et al.* 2020). SeNPs are reported to kill cancer cells owing to their pro-oxidant behavior inside the cancer cells and studies showed that SeNPs also target matrix metalloprotein, by inhibiting metastasis in cancer cells (Rajkumar *et al.* 2020). One promising area of research is the application of nanotechnology towards selenium fabrication and use. SeNPs are particularly suitable as they possess high surface area to volume ratios, increased surface area, and increased interactions with biological targets, leading to higher availability and absorption by the host. Also, SeNPs have lower toxicity than their elemental form (Chung *et al.* 2020).

Selenium metal is one of the overbearing trace minerals since it plays an essential role for human health. Selenium nanoparticles (SeNPs) received attention due to its biocompatibility and low toxic nature apart from its high specific surface area, high surface activity, abundant surface active centers, high catalytic efficiency and adsorbing ability (Anu *et al.* 2017). SeNPs have developed as potential novel therapeutic agents exhibiting good optical and photo-electric properties and high photo-conductivity, making them admirable as rectifiers and solar cells. Their high reactivity with other inorganic elements has been explored in the synthesis of other functional materials such as cadmium selenium (CdSe), lead selenium (PbSe) and zinc selenium (ZnSe) for the use in diagnostic and imaging studies (Maiyo *et al.* 2017). SeNPs are found to reduce alcohol-induced cardiomyopathy by reducing the lethal factors such as oxidative stress and apoptosis effects caused by alcohol consumption and are naturally found in the human body at around 5 nm to 200 nm in size (Chandramohan *et al.* 2018).

SeNPs have emerged as a novel form of selenium, finding a role in medicine as delivery vehicles, by advantage of their unique properties (Maiyo *et al.* 2017). Limited works have been reported about the green synthesis of SeNPs. Chandramohan *et al* synthesized hollow SeNPs using a potato extract. The results indicated that the potato extract reduces the toxicity of hollow SeNPs and lower concentrations of hollow SeNPs could be used for various biomedical applications in future (Chandramohan *et al.* 2018). Alagesan and Venugopal reported the green synthesis of selenium nanoparticle using leaves extract of *Withania somnifera* (poison gooseberry), SeNPs were spherical within the diameter range of 45 - 90 nm (Alagesan *et al.* 2019). Fardsadegh *et al* used an oleo vera leaf extract to synthesize spherical SeNPs, which had high antibacterial and antifungal activities (Fardsadegh *et al.* 2019a). Mellinas *et al* did a microwave-assisted synthesis of SeNPs using *theobroma cacao L*. bean shell extract (Mellinas *et al.* 2019). Kapur *et al* reported green Synthesis of SeNPs from Broccoli (Kapur *et al.* 2017).

2.2.2 Silver Nanoparticles (AgNPs)

Silver nanoparticles (AgNPs) have been receiving wide attention due to their numerous applications such as biomolecular detection and diagnostic, therapeutic, catalysis, micro-electronics fields, and sensing to name a few. Due to their nontoxicity

towards humans, they are a popular choice when compared to the other metals and materials (Ali *et al.* 2016). Due to their unique physical, chemical, and biological properties, AgNPs are applied in many different areas, such as bio labeling, medicine, electrochemistry and food packaging and AgNPs have been widely used in many different industries showing their excellent antibacterial, antiviral and antifungal activities (Mohammadlou *et al.* 2017).

Most methods for producing AgNPs require numerous chemicals, which not only is expensive but also could produce a hazardous residue. Therefore, green synthesis of AgNPs is desirable to provide an eco-friendly, and cleaner synthesis route. Plant extracts work so well in the green synthesis of AgNPs under mild experimental conditions and replacing hazardous chemicals by polyphenols, flavonoids, proteins, saponins or sugar as reducing agents (Ali *et al.* 2016; Baraka *et al.* 2017; Kumar *et al.* 2017). Synthesis of AgNPs attracts attention due to its numerous applications in different fields. Plants' extracts are usually used for the green synthesis of AgNPs as a suitable alternative to the chemical and physical methods (Baraka *et al.* 2017).

Sabela *et al* reported a one-pot biosynthesis of AgNPs using *Iboza Riparia* and *Ilex Mitis* extracts for cytotoxicity on human embryonic kidney cells (Sabela *et al.* 2018). Saha and Bandyopadhyay synthesized AgNPs using *allium sativum* (Saha *et al.* 2019). Ali and co-workers synthesized AgNPs using apple extract and evaluated its antibacterial properties:nanoparticles in suspension showed activity against Gram-negative and Gram-positive bacteria (Ali *et al.* 2016). Kumar *et al* synthesized AgNPs using Andean blackberry fruit extract. They observed spherical shaped AgNPs with an average size of 12 nm (Kumar *et al.* 2017). Mohammadlou *et al* used a hydrothermal green synthesis for AgNPs using *pelargonium* leaf extract and evaluated their antifungal activity (Mohammadlou *et al.* 2017). Baraka *et al* reported the synthesis of AgNPs using natural pigments extracted from Alfalfa leaves and its use for antimicrobial activity (Baraka et al. 2017).

2.2.3 Cadmium Sulfide Quantum Dots (CdSQDs)

Cadmium sulfide quantum dots (CdSQDs) have been identified as a potential candidate to diagnose cancerous cell and have been synthesized through a broad range of physical and chemical techniques such as microwave heating, microemulsion

synthesis, and ultrasonic (Shivaji *et al.* 2018). CdSQDs have attracted significant attention for electronics, photodiodes, sensors, and solar cells because of their wide bandgap energy that can be changed by varying their particle size and morphologies (Qin *et al.* 2018). They are the most vital semiconductors of groups II-VI among numerous semiconductor materials.

Due to their size-dependent photoluminescence tunable in the visible spectrum, the main interest of CdSQDs is their photoluminescent properties which make the quantum dots suitable for biological and biomedical research (Garmanchuk *et al.* 2019).The chemical synthesis of QDs produces a measure of toxic components that prevent them for biological applications and plant synthesis of quantum dots is very considerable due to their low costs, short production time, safety, and large production amounts (Gholami *et al.* 2020). QDs such as cadmium sulfide provides several advantages, such as ease of preparation, size-dependent emission wavelength, high-quantum yield, and photostability (Hsu *et al.* 2012).

The use of plant extracts for the preparation of QDs has gained more attention. Shivaji *et al* synthesized CdSQDs using tea leaf extract and explored the biological activity of the QDs in bioimaging and antibacterial activities (Shivaji *et al.* 2018). Qin *et al* developed a novel green route to prepare bio-compatible CdSQDs using the white-rot fungus *Trametes versicolor* (Qin *et al.* 2018). One-pot synthesis of CdSQDs from naturally available fruit sap *Opuntia ficus-indica* was synthesized by Kandansamy and co-workers (Kandasamy *et al.* 2019). Gholami *et al* biosynthesized spherical CdSQDs with a size distribution between 2 - 7 nm using aqueous extracts of the hairy roots of *rhaphanus sativus* (Gholami et al. 2020).

2.3 Nanomaterial-Protein binding

Spectroscopic investigations on the interaction between nanomaterials and protein have significance in the field of chemistry, materials science, and biology. The protein nano-conjugate possesses numerous potential applications related to bio-analytical science, bio-sensors, bio-catalysis, and bio-based nano-devices (Ambika *et al.* 2015). Since HSA is known to undergo different pH-dependent conformational transitions, it is an ideal candidate for studying protein-ligand interaction (Chatterjee *et al.* 2012). Structural characterization and binding energies of the complexes are the main

features in the understanding of biological and pharmaceutical properties since interactions occur via the binding sites of HSA (Khulu 2015). HSA holds some ligands in a stressed environment thereby allowing for their metabolic alteration and also reduces possible toxins by transporting them to disposal sites. HSA also acts as a nitric oxide carrier, leading to covalent alteration of macro-molecules (Khulu 2015). Here we perform spectroscopic investigations on the interaction between nanomaterials and HSA.

Beg *et al* reported spectroscopic interaction of AgNPs with human serum albumin and overall, the AgNPs show versatile biological activities and may be applied in the field of nanomedicine (Beg *et al.* 2017). Mahanmmadlou *et al* reported spectroscopic and electrochemical studies on the molecular interaction between copper sulfide (CuSNPS) nanoparticles and bovine serum albumin (BSA): the results revealed that the CuS NPs interact with BSA by inducing the conformational changes in secondary structure and reducing the a-helix content of BSA (Mahanthappa *et al.* 2018). Rezanejade Bardajee *et al* reported spectroscopic studies on the interactions of capped CdSQDs with HSA and BSA, the results affirmed the complex formation between the synthesized QDs and HSA or BSA (Rezanejade Bardajee *et al.* 2017). Prananth and Sudarsanakumar reported the spectroscopic and thermodynamic analysis on the interaction of L-cysteine-capped SeNPs and HSA (Prasanth *et al.* 2017).

2.4 Detection of ATP

There is a great demand for the determination of ATP, due to its role as universal energy sources for protein synthesis and metabolic activities (Manjubaashini *et al.* 2019). Multiple approaches have been developed to detect ATP, such as the isotope tracing method (Chen *et al.* 2012), high-performance liquid chromatography (HPLC) (Feng *et al*. 2020), photo-electrochemical aptasensor surface-enhanced Raman scattering, optomagnetic aptasensor (Tian *et al*. 2017), fluorescent spectroscopy (Liu *et al*. 2019), and chemiluminescence resonance energy transfer (Sang *et al*. 2019). Even though these methods provide satisfactory sensitivity and stability, they are time-consuming, expensive equipment and large background interferences are commonly involved, hence limit their potential application fields. (Wang *et al*. 2018; Liu et al. 2019). An electrochemical method for the determination of biological entities such as

ATP is advantageous due to it being cheaper, has high selectivity and sensitivity, and is more convenient (Manjubaashini *et al*. 2019).

Enzyme immobilization using electrochemically deposited polymers is well described in the literature and allows directed modification of electrode surfaces. A novel immobilization technique based on the electrochemically induced, localized deposition of enzyme-containing polymer suspensions has been reported (Kueng *et al.* 2004). This immobilization shows high selectivity for the immobilization site, sufficient control on the overall immobilization process, the potential to operate at miniaturized electrode surfaces, and excellent long-term stability of the protein within the polymer matrix. The skill has successfully been applied for the formation of a double layer biosensor with one layer containing glucose oxidase and one layer containing catalase (Kurzawa *et al.* 2002). Electrochemical biosensors based on glucose oxidase (GO) with hexokinase (Hex) seem to be a suitable method for the determination of ATP, due to its sensitivity, rapid response, and continuous monitoring (Zhu *et al.* 2018).

Herein we report the determination of ATP in nutritional supplements using a modified Glassy carbon electrode (GCE) modified with nanomaterials and dual enzyme composite as a working electrode. Enzymes are most frequently used in the construction of biosensors as their recognition is highly selective or even specific to their substrates and their conversion is of high catalytic efficiency (Weber 2014). Hence, if enzymes are combined with a transducer, the resulting biosensor offers high selectivity and sensitivity towards the targeted analyte. Enzymes operate at physiological conditions and can be therefore perfectly applied in *in vivo* and *in vitro* measurements.

Jiang *et al* reported the development of an electrochemical biosensor for sensitive detection of ATP in rat brain with *in vivo* microdialysis (Jiang *et al.* 2019). Xiao *et al* developed an electrochemical aptamer-based assay that is described for the ultrasensitive and highly specific determination of ATP (Xiao *et al.* 2019). Wang *et al* constructed a paper-based electrochemical biosensing electrode for rapid and accurate detection of ATP and verified assay of ATP in human serums, cancer cells, and normal cells with satisfactory results (Wang *et al.* 2018). Manjubaashini et al reported the electrochemical determination of ATP using rhodamine 6G capped gold nanoparticles (FCGN) modified carbon felt (CF) as a working electrode

(Manjubaashini *et al.* 2019). Shao et al reported a highly sensitive electrochemical biosensor for the detection of ATP, based on porous anodic alumina (PAA) and SiO_2 nanoparticles combining with several oligonucleotides to construct a sandwich structure (Shao *et al.* 2018).

CHAPTER 3: METHODOLOGY

This chapter focuses on major methodologies used in this study, which compromise of synthesis of pyrazole ligand and nanomaterials and their application. The first subsection describes the instrumentation, the characterization techniques that were used to confirm the nanomaterials followed cytotoxicity activity. This is followed by a descriptive section for the preparation of all the working standards and the preparation for enzyme activity for analysis. The second subsection is based on the application of the nanomaterials where the electrochemical determination of ATP using a GC electrode is modified with the nanomaterials and a dual enzyme reaction. Lastly, the spectroscopic investigations on the interaction between nanomaterials and protein (HSA).

3.1 Instrumentation

The characterization techniques used for synthesized nanomaterials were UV–Vis, HR-TEM and FTIR whilst the spectroscopic investigations on the interaction between nanomaterials and protein were performed using FTIR, UV-Vis, and fluorescence and for electrochemical detection of ATP, 797 VA computrace. pH meter was used to adjust the pH of the buffer solutions

3.1.1 UV-Vis spectroscopy

The Agilent Cary 60 UV-Vis Spectrophotometer was used to determine the UV-visible spectra of the synthesized nanomaterials and for the interaction between HSA protein and nanomaterials. UV- Visible spectra of all solutions were recorded in the range of 200 - 800 nm against a blank solution with a 1.0-cm quartz cell at room temperature.

3.1.2 pH meter

A pH/ion meter coupled with a stirrer (Hannan instruments Microprocessor) was used to adjust the pH of the buffer solutions.

3.1.3 Fluorescence spectrophotometer

The Varain cary eclipse Fluorescence spectrophotometer was used to determine the fluorescence quenching data HSA-nanomaterial complex. All the solutions were

recorded in the range of 290 - 500 nm against a blank solution with a 1.0-cm quartz cell at room temperature with excitation wavelength at 280 nm.

3.1.4 Fourier Transform Infrared spectroscopy

The analysis of functional groups of the nanomaterials. The Agilent Cary 630 FTIR spectrometer with a wide range of sample interfaces and high performing optics, including Agilent's unique and revolutionary DialPath (an easy to use liquid sample FTIR module) for measuring liquids was used at the range of 4000 to 400 cm^{-1}.

3.1.5 High resolution Transmission Electron Microscopy

A JEOL 2100 High-resolution Transmission Electron Microscope (brightfield, darkfield, diffraction STEM, EDX) was used for the optical microscopic viewing of the nanomaterials at 200 kV acceleration voltage, for the particle sizes and morphology of the nanomaterials. The samples were dissolved in ethanol and sonicated for an hour before being placed on a carbon film and then air-dried at room temperature.

3.1.6 Electrochemical technique

The 797 VA Computrace was used to perform all electroanalytical measurements (Metrohm Herisau, Switzerland). Voltametric curves were recorded at room temperature using a three-electrode system. The working electrode was a glass carbon electrode (GCE), an Ag/AgCl (saturated AgCl, 3M KCl) was used as a reference electrode and a platinum wire was used as a counter electrode. The 797 VA computrace performs both qualitative and quantitative measurements, qualitative measurements were done using cyclic voltammetry (CV) and quantitative measurements using Square Wave voltammetry (SWV).

3.2 Reagents and materials

Allium Sativum cloves (garlic) purchased from a local supermarket in Durban (South Africa), *Pelargonium graveolens* leaves purchased from a local market in Durban (South Africa), *Moringa Oleifera* leaves were collected from a nearby suburb Phoenix in Durban (South Africa), Multi-Walled Carbon Nanotubes (MWCNTs), supplied by Alfa Aesar chemical reagent company. Dimethyl sulfoxide ($(CH_3)_2SO$, ≥ 99.7 % purity for HPLC), Methanol (CH_3OH, ≥ 99.9 % purity for HPLC), and Human Serum Albumin lyophilized powder (≥ 97 % purity) were purchased from Sigma Aldrich (South Africa). Glucose Oxidase type x-s from aspergillus, Hexokinase sulfate-free from baker's yeast, Glutaraldehyde grade II, Glycerin, Adenosine 5′-triphosphate disodium salt hydrate ($C_{10}H_{14}N_5Na_2O_{13}P_3 \cdot xH_2O$), Silver nitrate ($AgNO_3$, ≥ 99.9 % purity) Cadmium sulfate ($CdSO_4$, ≥ 99.99 % purity), Sodium Sulfide (Na_2S, ≥ 98 % purity), Sodium selenite (Na_2SeO_3≥ 99 % purity), Potassium hexacyanoferrate trihydrate ($K_3Fe(CN)_6$), Potassium hexacyanoferrate ($K_3Fe(CN)_6$), Potassium dihydrogen phosphate (KH_2PO_4), Dipotassium hydrogen phosphate (K_2HPO_4) all purchased from Sigma Aldrich (South Africa), The human embryonic kidney cells (HEK293), Breast cancer cells (MCF – 7) Lung cancer cells (A549), Dulbecco's Modified Eagle Medium (DMEM), 20 µL MTT all purchased from Sigma Aldrich (USA),The Glassy Carbon electrode (GCE) was supplied by Metrohm Ion Analysis. All reagents were of analytical grade, were used without any further purification and deionized water was used for the preparation of samples.

3.3 Indole pyrazole ligand (TRPIDC-CH_3) synthesis

A [3+2] cycloaddition reaction was used by Makhanya et al to synthesize TRPIDC-CH_3 ligand by reacting p-tolualdehyde, 4-methyl-3 thiosemicarbazide and indole, under reflux, in the presence of indium chloride as a Lewis acid catalyst. The product obtained was 3-phenyl- 2, 3-dihydropyrazolo [3, 4-*b*] indole-1(4H)-carbothioamide (Makhanya 2019). A Plausible mechanism for this reaction is presented bellow.

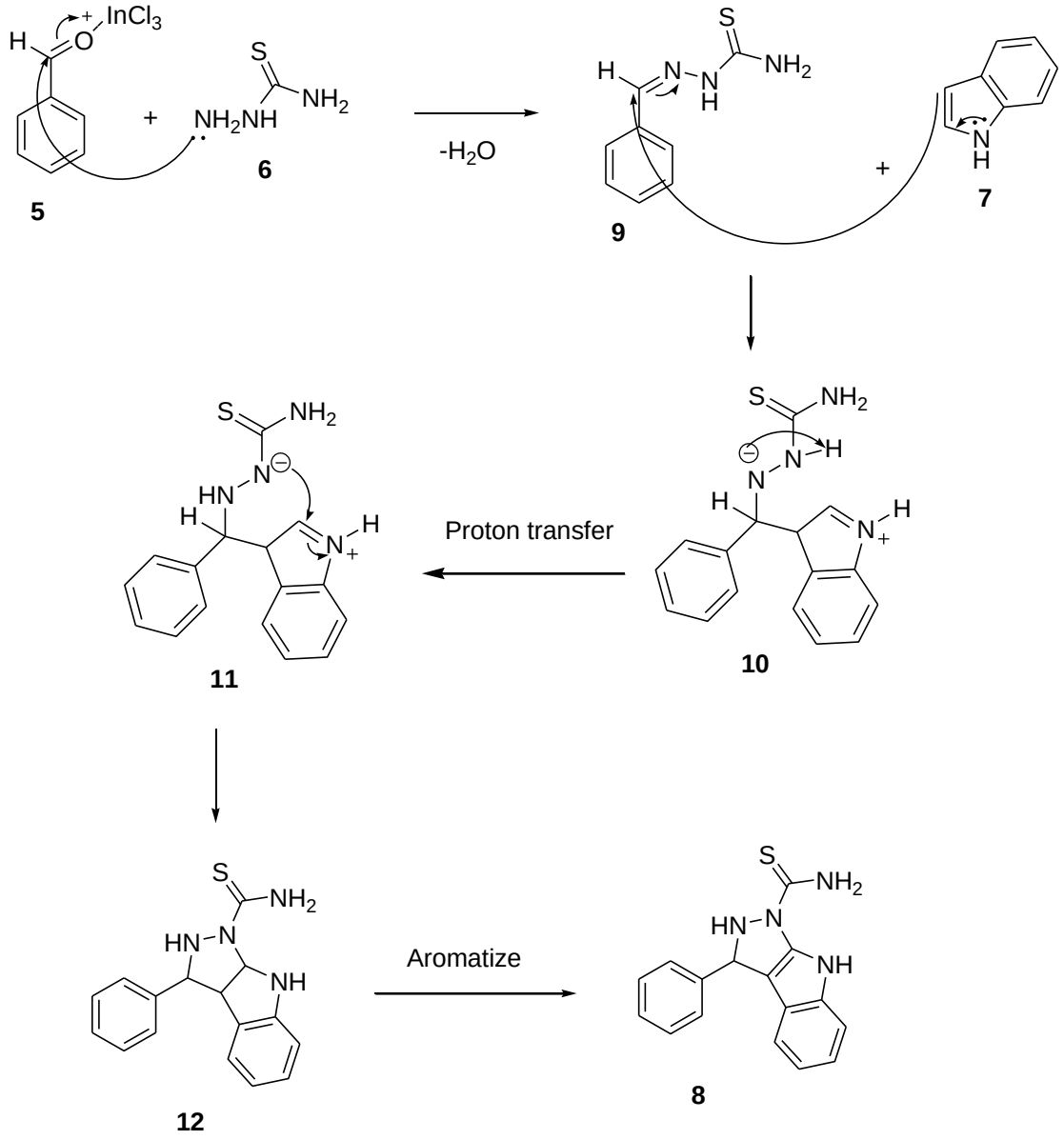

Figure 3.1: Plausible mechanism for [3+2] annulation reaction for the synthesis of TRPIDC-CH_3 ligand.

3.4 Plants extract preparation and nanomaterials synthesis

Three different plant extracts were used to synthesize both TRPIDC-CH_3 capped and uncapped nanomaterials. To synthesize the capped nanomaterial, TRPIDC-CH_3 ligand was used and for uncapped TRPIDC-CH_3, the ligand was omitted.

3.4.1 TRPIDC-CH_3 capped Selenium Nanoparticles synthesis

An accurate mass (5 g) of *Allium Sativum* cloves without an outer layer was weighed, then washed thoroughly with deionized water, dried and grounded using mortar and pestle. Approximately 10 ml of oil extract from the grounded *Allium Sativum* cloves was filtered using a muslin cloth thereafter with Whatman No. 1 filter paper and then stored in the refrigerator at 4 ^{o}C for further use. The nanoparticles were prepared by mixing 2 mL of *Allium Sativum* extract, 20 mL of 20 mM Na_2SeO_3 solution and 2 mL of TRPIDC-CH_3 solution in a 50 ml beaker. TRPIDC-CH_3 solution was prepared by dissolving the ligand in 10 % DMSO. The resulting pale yellow homogeneous mixture took 72 hrs to change to brick red when heated in a magnetic stirrer at 160 rmp at 60 ^{o}C. Figure 3.2 below is a schematic diagram for the plant extract preparation and synthesis of TRPIDC-CH_3 SeNPs.

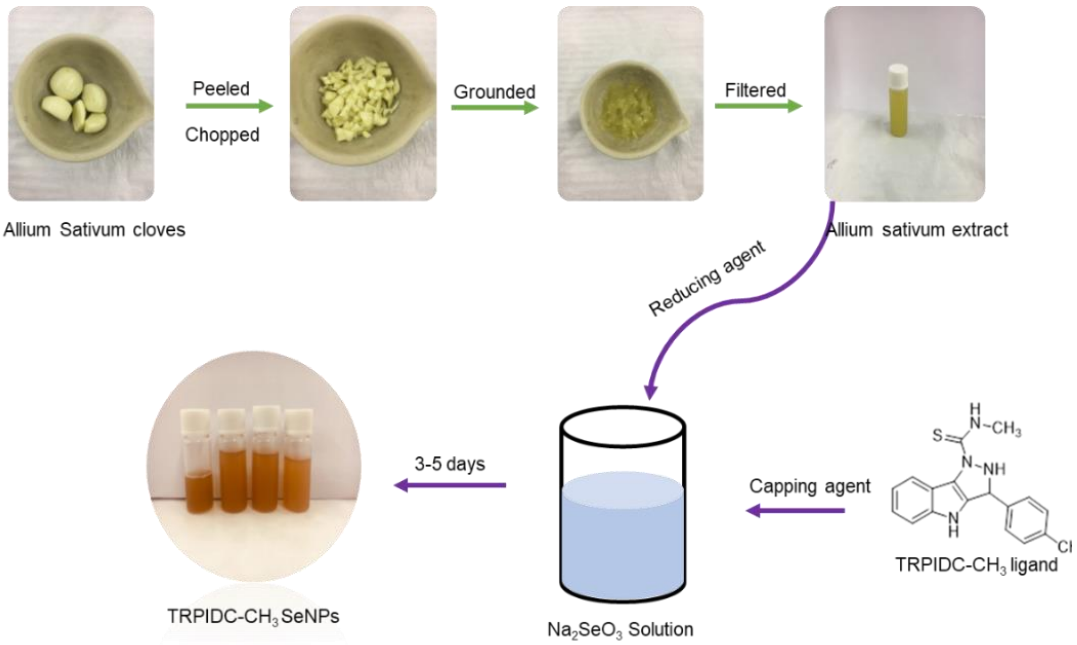

Figure 3.2: Schematic diagram for the plant extract preparation and synthesis of TRPIDC-CH_3SeNPs.

3.4.2 TRPIDC-CH_3 capped Silver Nanoparticles synthesis

The *Pelargonium graveolens* leaves were washed three times with tap water to remove the dirt from the surface followed by deionized water and dried in hot air overnight. The dried leaves were powdered using mortar and pestle: 1 g of the powdered leaves was added into 100 mL of deionized water and boiled for 5 minutes. The mixture was filtered using a Whatman No.1 filter paper and stored in the refrigerator at 4 ^{o}C for further use. To synthesis the TRPIDC-CH_3 capped Silver nanoparticles (TRPIDC-CH_3 AgNPs), 6 mL of pelargonium graveolens extract was mixed with 50 mL of 5 mM $AgNO_3$ and 6 mL of TRPIDC-CH_3 solution. The mixture was incubated at 37 ^{o}C until the color change to dark-brown as show in Figure 3.3.

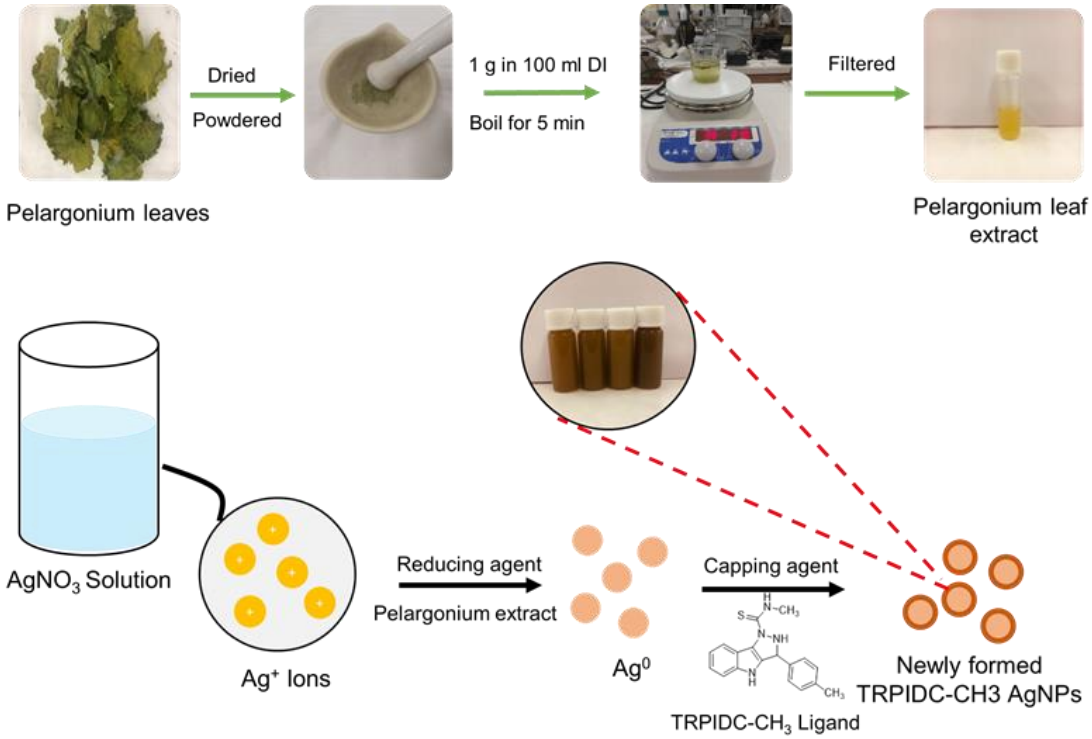

Figure 3.3: Schematic diagram for the plant extract preparation and synthesis of TRPIDC-CH_3AgNPs.

3.4.3 TRPIDC-CH_3 capped Cadmium Sulfide Quantum Dots synthesis

The *Moringa Oleifera* leaves leaves were washed with deionized water and air-dried for 3 days. Thereafter 3 g of the leaves were added to 30 mL of methanol and incubated in the dark for 24 hours. Then the *Moringa Oleifera Lam* extract was filtered through a Whatman No.1 filter paper and store at 4 ^{o}C for further use. 2 mL of 0.025 M $CdSO_4$ and 2 mL of TRPIDC-CH_3 solution was added to 30 mL of the *Moringa*

Oleifera extract and was incubated for 3 days in the dark. After the 3 days of incubation, 0.5 mL of 0.025 M Na_2S was added and incubated for another 4 days to produce TRPIDC-CH_3 capped cadmium sulfide quantum dots (TRPIDC-CH_3CdSQDs). The colour was bright yellow. The schematic diagram for the plant extract preparation and synthesis of TRPIDC-CH_3CdSQDs is shown in Figure 3.4.

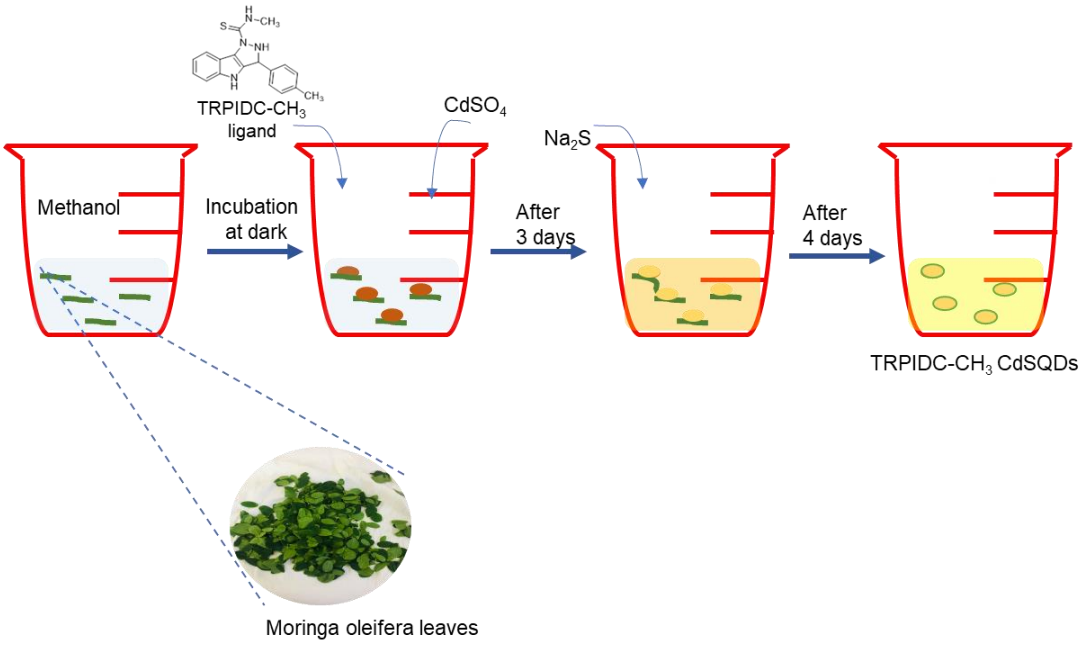

Figure 3.4: Schematic diagram for the plant extract preparation and synthesis of TRPIDC-CH_3CdSQDs.

3.5 Phytochemical analysis

3.5.1 Test for Alkaloids

2 mL of extract was added in 3 ml of 2% (v/v) HCl and then a few drops of Mayer's reagent was added. The presence of basic alkaloids suggests the emergence of the dull white precipitate.

3.5.2 Test for Saponins

2 mL of the extract was shaken vigorously in a test tube for 30 seconds. The consistency of thickness foam even after 30 minutes suggested the presence of saponins.

3.5.3 Tests for Flavonoids

2 mL of test solution was treated with a few drops of ferric chloride solution: the development of blackish-red color suggests the presence of flavonoids.

3.5.4 Tests for Tannins and Polyphenols

4 mL extract was treated with 4 mL $FeCl_3$: the formation of green colour indicated the presence of tannins and the dark-blue indicated the presence of polyphenols

3.5.5 Tests for Terpenoids

Test for terpenoids was conducted by mixing 3 ml of the extract with 2 mL of $CHCl_3$ in a test tube. Thereafter, 2 mL of concentrated H_2SO_4 was added gently to form a ring layer that interfaced with a reddish-brown colour, thus indicating the presence of terpenoids.

3.6 Determination of concentration for the nanomaterials

3.6.1 Calculation of the average number of atoms per nanomaterials

The average number of nanomaterials can be estimated using the HR-TEM images of nanomaterials. The average core diameters of the particles (D, nm) are calculated and summarized using ImageJ software. Assuming a spherical shape and a uniform structure; (Liu *et al.* 2007; Elnoby *et al.* 2018), the average number of nanomaterials atoms (N) for each type of nanosphere is calculated by Equation. (1) (Liu *et al.* 2007; Elnoby *et al.* 2018), where ρ is the density for nanomaterials (g/cm^3) and M stands for the atomic weight of the nanomaterial element.

$$N = \frac{\pi}{6}\frac{\rho D^3}{M} \quad (1)$$

3.6.2 Determination of molar concentrations of nanomaterials solution

The molar concentration of nanosphere solutions (C) was determined by dividing the (N_{Total}) total number of gold atoms (total, equal to the original amount of salt added to the reaction solution) by the average number of nanomaterial atoms per nanosphere (N) according to Equation (2), where V is the volume of the reaction solution in litre

and NA is the constant of Avogadro. It is believed that the reduction from nanomaterial ions to atoms is 100% complete. (Liu *et al.* 2007; Elnoby *et al.* 2018).

$$C = \frac{N_{Total}}{NVN_A} \quad (2)$$

3.7 Cytotoxic activity of the nanomaterials

3.7.1 1 Cell line

The cell lines used in this study are MCF-7 (breast), A549 (lung), and HEK293 (normal human embryonic kidney). These cells were stored in 25 cm^2 tissue culture flasks. On arrival, the cells were incubated at 37^oC in a humidified incubator (Snjiders Hepa, United Scientific, Cape Town, South Africa) in a 5% CO_2 environment. The cells were transferred to two different 75 cm^2 flasks (Greiner, Germany) after three days, once they were found to be 80% confluent.

3.7.2 Cell maintenance

All cell culture experiments were conducted in the laminar flow cabinet (Scientific Engineering INC) to maintain sterility. The laminar flow cabinet was sterilized by exposure to UV-light and swabbing with 70% ethanol before experimentation. MCF-7, A549, and HEK293 cells were grown in two separate monolayers in Dulbecco's Modified Eagle Medium (DMEM) (Sigma-Aldrich, Inc) (glucose (4.5 gL^{-1}), one mM L-glutamine, and one mM sodium pyruvate). The DMEM was supplemented with 1% antibiotic (penicillin/streptomycin) solution (Sigma-Aldrich, Inc) and 10% heat-inactivated foetal calf serum (FCS). MCF-7, A549, and HEK293 cell lines were sub-cultured every 2-3 days, once the flasks had become 80% confluent, to maintain them in the exponential growth phase.

3.7.3 Cytotoxicity assay

The MTT assay was carried out in 96 well, flat-bottom microtiter plates (Costar, Corning, USA) according to the protocol described by Majeed *et al*. and Wu *et al*., with minor modifications. For the MTT assay, doxorubicin was used as a standard. The MTT assay was commonly used to determine the rate of cell proliferation dependent on the mitochondrial reduction of tetrazolium salt. The synthesized nanomaterials' anticancer activity was assessed against two cancer cell lines, which include breast

(MCF-7) and lung (A549), and normal human embryonic kidney cell lines. Different concentrations (50 and 100 µg / mL) of A1-A6 nanoparticles were evaluated in triplicates for 48 h in this study, and findings are expressed as an average ± standard deviation.

An aliquot of 90 µL (1 x 104 cells) of the MCF – 7, A549, and HEK293 cell suspension was transferred to the microtiter plates. Sterile distilled water was added to the outer wells to prevent evaporation of the medium. The plates were incubated in a 37°C humidified incubator for 24 h to allow the cells to attach to the wells. An aliquot of 10 µl of the test nanoparticles was added to the wells at two concentrations (100 µg/mL and 50 µg/mL). In control wells, 10 µl of DMSO (1%), DMEM (medium control), and the positive control 10 µl doxorubicin was added to the well. The plates were incubated at 37°C for 48 hours in a humidified incubator with 5% CO_2. After incubation, 10 µl of MTT reagent (Sigma, St Louis, USA) were added to the plates, and they were incubated for a further 4 hours at 37°C in a humidified incubator with 5% CO_2.

After incubation, 100 µl of DMSO was added to the wells and the plates were incubated for an additional 1 hour. DMSO was added to dissolve the insoluble formazan crystals that will be formed by the MTT reagent once it enters the cells. The Absorbance of the plates was read at a wavelength of 590 nm on an ELISA microplate reader (Digital Analogue Systems, Italy) (Wu *et al.* 2014; Majeed *et al.* 2016). The percentage of cytotoxicity will be determined using the following equations:

% Cell Viability = Absorbance of treated cells x 100 (3)

The Absorbance of untreated cells

% Cytotoxicity = 100 - % Cell Viability (4)

3.7.4 Statistical analysis

Each experiment was done in a triplicate and the results are described as mean ± standard deviation (SD). The statistical significance of the variations between the groups was evaluated using a one-way ANOVA test followed by a post-hoc Bonferroni test and mean values with a probability value of $p<0.05$ were deemed statistically important.

3.8 Protein interaction

3.8.1 Binding

HSA was dissolved in a PBS (0.10 M, pH 7.3) and was stored in the dark at 4 ˚C for further use. An exact 50 µL of stock solutions of HSA was added to a 2000 µL centrifuge tubes, successive additions of the nanomaterial while varying the volumes of nanomaterials from 0 to 30 µL (Table 3.1) and top up with phosphate buffer. All test solutions were incubated for 40 min at 37 ºC before each measurement and the interaction between HSA and the nanomaterials was monitored using UV-Vis spectroscopy and FTIR.

Table 3.1: Volumes of HSA, Nanomaterials, and buffer used for interaction studies.

Volume of HSA (µL)	Volume of Nanomaterials (µL)	Volume of Phosphate Buffer (µL)
50	0	1950
50	5	1945
50	10	1940
50	15	1935
50	20	1930
50	25	1925
50	30	1920

3.8.2 UV-Vis absorption studies

The UV-Vis measurements were studies using the following equation (5) (Prasanth *et al.* 2017).

$$\frac{1}{(A_0-A)} = \frac{1}{(A_c-A_0)} + \frac{1}{(A_c-A)} \times \frac{1}{K_b[Q]} \quad (5)$$

where A is the absorbance of HSA at various concentrations of the nanoparticles A_0 is the absorbance of HSA alone, and A_C is the absorbance of HSA - nanoparticles complex. $[Q]$ is the concentration of the nanoparticles. The binding constant (K_b) is determined from the slope of the plot of $\frac{1}{(A_0-A)}$ versus $\frac{1}{[Q]}$.

3.8.3 Fluorescence quenching studies

Fluorescence was determined by exciting HSA at 280 nm and the emission spectrum was measured at 290–450 nm since tryptophan fluorescence is used as a local

environment probe for protein structure, dynamics and ligand binding. The change in fluorescence intensity at a specific wavelength was calculated using Stern−Volmer equation (6) to analyze the fluorescence quenching data (Pansare *et al*. 2018)

$$\frac{F_0}{F} = 1 + KSV[Q] = 1 + KqTo[Q] \quad (6)$$

Where F_0 and F are the fluorescence intensity of HSA in the absence and presence of the quencher [Q], respectively, K_{SV} is the Stern–Volmer quenching constant, K_q is the bimolecular quenching constant, and τ_0 is the lifetime of the fluorophore in the absence of the quencher(~ 10^{-8} s). where K_b is the binding constant and *n* is number of binding sites

$$log\ [\ (\frac{F0 - F\ )}{F}] \ = \ log\ Kb \ + \ n\ log\ [Q] \quad (7)$$

3.8.4 Mode of binding

The thermodynamic parameters change in enthalpy (ΔH) and change in entropy (ΔS) were determined after measuring K_b at different temperatures and the results were analyzed according to van't Hoff equation (8)

$$ln(Kb) \ = \ -\ (\frac{\Delta H}{T}) \ + \ (\frac{\Delta S}{R}) \quad (8)$$

Where R (8.314 J mol^{-1} K^{-1}) and T represent the universal gas constant and absolute temperature, respectively. For hydrogen bonding or van der Waals interactions, Δ*H,* and Δ*S* are negative, for hydrophobic interactions Δ*H* and Δ*S* are positive, and for electrostatic interactions, Δ*H* is positive or negative, and Δ*S* is positive (Prasanth *et al.* 2017). The change in Gibbs free energy (ΔG) can be further calculated from different terms of enthalpy change (ΔH) and entropy change (ΔS) according to the equation (9).

$$\Delta G \ = \ -\ RT\ lnKb \ = \ \Delta H \ - \ T\Delta S \quad (9)$$

The positive sign of Δ*H* and negative sign of ΔG indicates that the binding process is an endothermic and spontaneous and the negative sign of Δ*H* and ΔG indicates that the binding process is exothermic and spontaneous (Mahanthappa *et al.* 2018).

3.9 Preparation of standard, supporting electrolyte, and spiked samples.

The supporting electrolyte of phosphate buffer (PBS) was prepared from K_2HPO_4 (0.1 M) and KH_2PO_4 (0.1 M) salts. The salts were dissolved in deionized water at room temperature and different volumes of each solution were mixed to adjust the pH accordingly as shown in Table 3.2. The 5 mM ATP standard solution was dissolved in PBS of pH 7 at room temperature. The Vita-thion and Swanson peak tablets samples dissolved in PBS were spiked with ATP standards (0.02 mM, 0.05 mM and 0.07 mM).

Table 3.2: Volumes of K_2HPO_4 and KH_2PO_4 used for different pH values

pH	The volume of 0.1 M K_2HPO_4 (mL)	The volume of 0.1 M KH_2PO_4 (mL)
5	8.5	91.5
6	13.2	86.8
7	61.5	38.5
8	90.8	9.2
9	94	6

3.10 Preparation and fabrication of GO:Hex/TRPIDC-CH_3 capped Nanomaterial /MWCNTs/GCE composite

The GCE was manually cleaned by polishing with alumina and electrochemically by cycling 50 times in the potentials range 0.0 to 2.0 V in 5 % nitric acid. This assured the elimination of any physiosorbed or chemisorbed materials from the electrode surface. The MWCNTs (5 mg) were dispersed in 1 mL of N,N-dimethylformamide (DMF), and sonicated until a paste was formed. A 1:1 mixture of MWCNTs paste and TRPIDC-CH_3 capped nanomaterial was sonicated for 45 min forming a runny paste. Thereafter it was manual deposited onto the electrode surface followed by air dried at 40 ^oC for 30 min and then allowed to cool to room temperature. The enzyme solution containing 8 mg/mL hexokinase, 2 mg/mL glucose oxidase and 1 µL glycerine was prepared in 1 mL PBS. Lastly, the enzyme solution was drop casted onto the TRPIDC-CH_3 capped nanomaterial/MWCNTs/GCE and allowed to dry in 4 hrs, followed by addition of glutaraldehyde (25%) for a 17 min enzymes cross-linkage

3.11 Electrochemical measurements

Approximately 10 mL of PBS supportive electrolyte was applied to the electrochemical cell under which either a bare glass carbon electrode or a modified glass carbon electrode was submerged prior to electrochemical measurements. An aliquot solution (ATP) was then injected into the electrochemical cell and the working electrode was given a pre-concentration potential while the solution was swirling at 400 rpm. Stirring was stopped at the end of the pre-concentration cycle and the balance time of 5s permitted the solution to be silent. Voltammograms were then recorded using a scanning rate of 100 mV/s by scanning the potential in a positive direction.

After each measurement, the working electrode was separated from the instrument and rinsed with deionized water. The electrochemical characterization of different modified electrodes was investigated using CV and SWV. The CV was carried out in 10 mL PBS (pH=7.0) containing 1 mM $K_4[Fe(CN)_6]/K_3[Fe(CN)_6]$ (redox probe) with a potential range of −0.2 V to 0.8 V and scan rate of 100 mV. The optimization of experimental conditions, calibration curve, selectivity and sample analysis were investigated using SWV in a potential range of - 0.2 V to + 0.8 V (SeNPs and CdSQDs) and -0.1 V to 0.4 V for the AgNPs with support electrolyte of 10 mL of 0.1 M PBS (pH=7.0) with 1 mM redox probe.

CHAPTER 4: RESULTS AND DISCUSSION

This chapter presents the results and discussion of the experimental analysis involving the synthesis and characterisation of the nanomaterials, application of capped pyrazole nanomaterials in the fabrication of the GCE, and the use of enzymes for the development of a biosensor. The various electrode was used to study the electrochemical behavior of both the ATP. Cytotoxicity activity using MTT assay and protein interaction were studied using UV-Vis absorption and Fluorescence quenching. This chapter is divided into three case studies presenting results of Silver nanoparticles, Selenium nanoparticles, and Cadmium sulfide quantum dots respectively.

4.1 CASE STUDY 1: Selenium Nanoparticles

In this sub-section, the results of capped and uncapped TRPIDC-CH3 SeNPs is discussed. Furthermore, the biological activities using HSA and anticancer activity against MCF-7 and A549, separately, are elaborated. The electrochemical behavior of ATP was determined using cyclic and square wave voltammetry using a glassy carbon electrode (GCE) modified with TRPIDC-CH_3 SeNPs and uncapped SeNPs. This decorated GCE was further evaluated in conjunction with glucose oxidase (GO) and hexokinase (Hex) enzymes.

4.1.1 Characterization of *allium sativum* extract

4.1.1.1 Phytochemical screening

Allium sativum has been reported to contain phytochemicals such as polyphenols, flavonoids, saponins, and terpenoids (Chen *et al.* 2018; Rose *et al.* 2018). To determine which phytochemicals will be able to reduce and stabilize the SeNPs , a phytochemical screening test was performed. The qualitative phytochemical screening test that was performed indicated the presence of alkaloids, flavonoids, saponins, and terpenoids. The FTIR results (Figure 4.1, page 43), showed presence of O-H (flavonoids and saponins), C-N (alkaloids), and C=C (terpenoids) in their chemical structures, confirming that the main reducing and stabilizing compounds were the phytochemicals that tested positives as shown in Table 4.1. These results are in agreements with literature.

Table 4.1: Characteristics of phytochemicals found in the *allium sativum* extract.

Compound class	Phytochemical test	Literature	Reference
Alkaloids	+ +	+	(Yee 2019; Maccelli *et al.* 2020)
Flavonoids	+ +	+	(Yee 2019; Maccelli *et al.* 2020; Sut *et al.* 2020)
Saponins	+ +	+	(Phan *et al.* 2019; Yee 2019)
Terpenoids	+ +	+	(Yee 2019)

++ positive current study; + literature

4.1.1.2 FTIR Studies

The FTIR spectrum (Figure 4.1) of pure *allium sativum* cloves extract, shows many absorption bands thereby indicating various biomolecules that are present. The absorption peak at 3311.74 cm^{-1} is attributed to O-H group stretch. The absorption peak at 2848.32 cm^{-1} is assigned to the C-H stretch. The peak at 1628.86 cm^{-1} is attributed to the C=C group stretch. The absorption peak at 1412.12 cm^{-1} is attributed to the O-H group bend. The absorption peak at 1038.08 cm^{-1} is due to the stretching of the C-N group. Satgurunathan *et al* reported the presence of C=C and C-H groups in the *allium sativum* cloves extract (Satgurunathan *et al.* 2017). Ezhuthuparakkal *et al* reported that O-H, C-N, and C-H groups were present (Ezhuthupurakkal *et al. 2017)*.

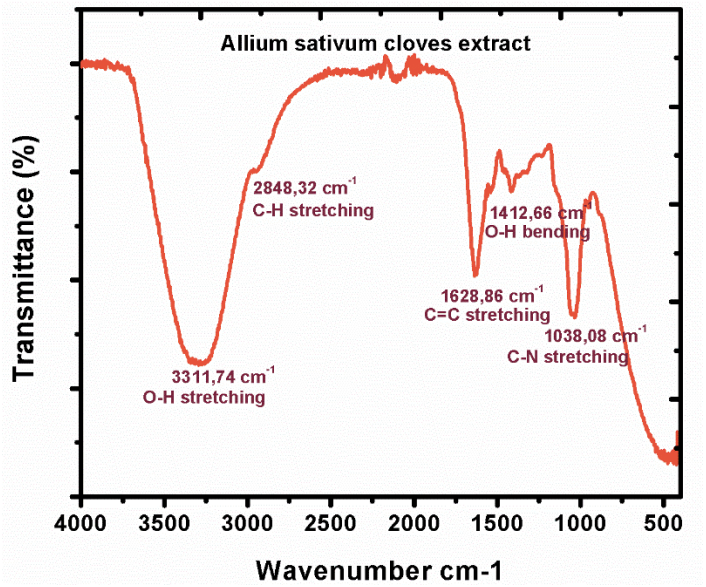

Figure 4.1: FTIR spectrum of *allium sativum clove* extract.

4.1.2 Characterization of TRPIDC-CH_3SeNPs

TRPIDC-CH_3 SeNPs (Figure 4.2) were synthesized through a simple and eco-friendly method from Na_2SeO_3 using *allium sativum* cloves extract as an effective reducing agent and TRPIDC-CH_3 ligand as a stabilizing agent. *Allium sativum* cloves extract was a clear yellow solution. Na_2SeO_3 appeared as a colourless solution. Upon the addition of *allium sativum* cloves extract and TRPIDC-CH_3 ligand, the Na_2SeO_3 solution changed to pale yellow, and finally, the colour changed to brick red there by indicating the formation of TRPIDC-CH_3 SeNPs. Similar colour changes were obsovered for the uncapped SeNPs. Also, Fardsadegh *et al* synthesized SeNPs from Na_2SeO_3 with aloe vera extract and produces brick red colored SeNPs (Fardsadegh *et al.* 2019a). It has also been reported that *wathania somnifera* leaf extract (Alagesan *et al.* 2019), cabbage extract (Gunti *et al.* 2019) and potato extract (Chandramohan *et al.* 2018) produced brick red coloured SeNPs**.**

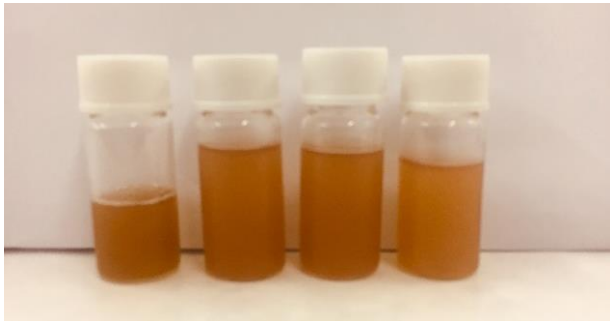

Figure 4.2: Green synthesized TRPIDC-CH_3 SeNPs.

4.1.2.1 UV-Visible

The formation of TRPIDC-CH_3 SeNPs using *allium sativum* cloves extract was confirmed by UV–Visible spectroscopy scanned in the range of 200 – 800 nm. A strong absorption band was observed at 270 nm which showed the reduction of selenite into selenium nanoparticles (Figure 4.3). The TRPIDC-CH_3 SeNPs showed an increase in absorbance by 1 %. In other studies where *allium sativum* cloves were used, the maximum absorption band was recorded at 260 nm (Anu *et al.* 2017) and 267 nm (Satgurunathan *et al.* 2017). Chandramoham *et al* reported a synthesis of SeNPs using potato extract with an absorption band seen at 200-300 nm region (Chandramohan *et al.* 2018). To assess their stability, the nanoparticles were allowed to stand for 30 days and observed daily for any colour changes: no colour changes

were observed. The sample was run by UV-Visible and there was no change to the absorption thereby indicating good stability of the nanoparticles.

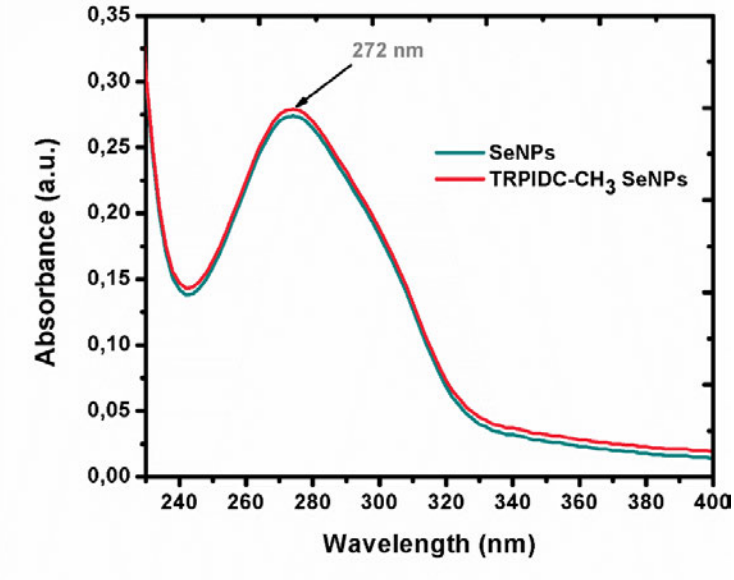

Figure 4.3: UV-Vis spectrum of TRPIDC-CH_3 SeNPs (**red**) and uncapped SeNPs (**dark cyna**) synthesized from Na_2SeO_3 using *allium sativum* cloves extract.

4.1.2.2 Morphology and Particle Size Analysis

The formation of TRPIDC-CH_3 SeNPs and the morphology was confirmed by HR-TEM analysis. The HR-TEM image of TRPIDC-CH_3 SeNPs, (Figure 4.4a) shows spherical nanoparticles that are monodispersed in nature. This particle size non-homogeneity may be attributed to the agglomerated shape of nanoparticles. The HR-TEM image and their size distribution (Figure 4.4c) showed that the average diameter and standard deviation of TRPIDC-CH_3 SeNPs (22 ± 9.0 nm), with a size distribution of particles with a diameter in the range of 6 – 75 nm. *Allium sativum* contains saponins (Chen *et al.* 2018), which produce smaller nanoparticles because structurally they have more hydrophilic glycoside moieties (Sabela *et al.* 2018). The results are consistent with previous studies on the use of plant extracts to synthesize SeNPs (Anu *et al.* 2017; Ezhuthupurakkal *et al.* 2017; Satgurunathan *et al.* 2017). Uncapped SeNPs (Figure 4.4b and d) showed with an average diameter of 20 nm synthesized parallel with TRPIDC-CH_3 SeNPs.

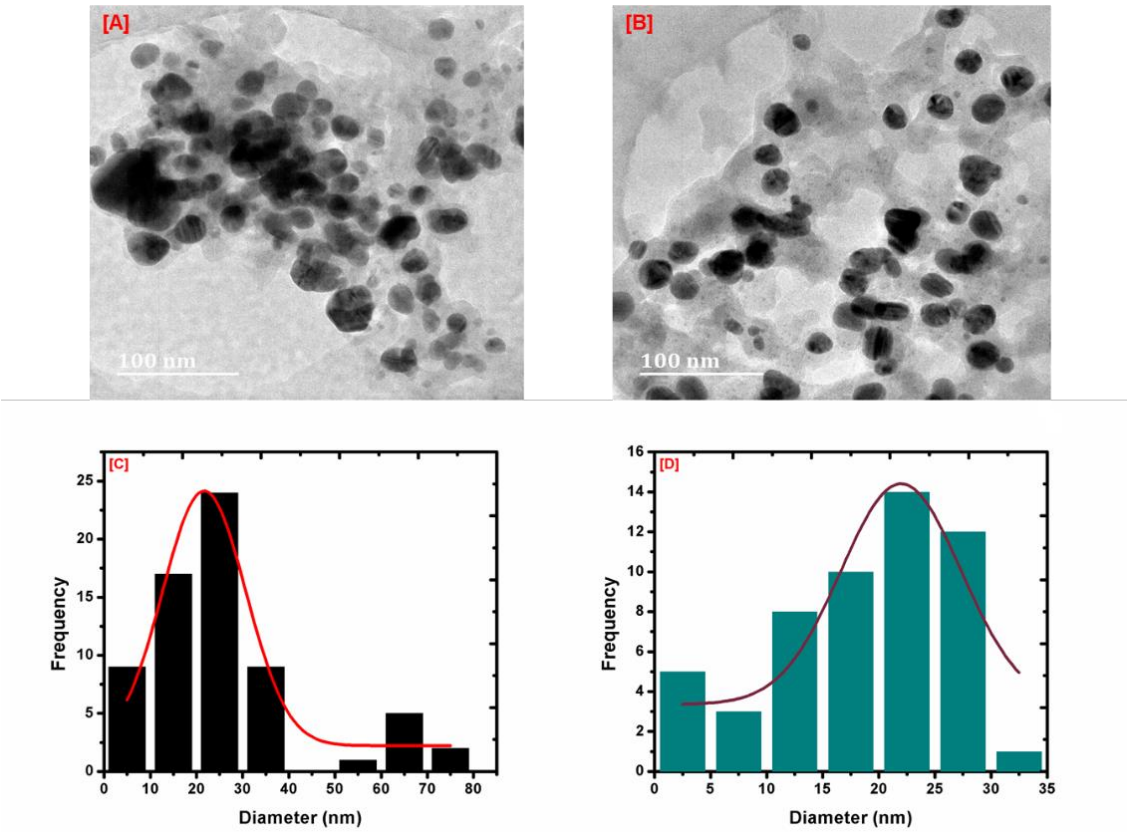

Figure 4.4: HR-TEM images of **(A)** TRPIDC-CH_3 SeNPs, **(B)** SeNPs and Size distribution histogram prepared by image j software of **(C)** TRPIDC-CH_3 SeNPs and **(D)** SeNPs.

4.1.2.3 FTIR studies

The FTIR spectrum of synthesized TRPIDC-CH_3 SeNPs in Figure 4.5 (pink) in comparison with uncapped SeNPs (violet), shows a broad absorption peak at 3240.92 cm^{-1}, which shifted from 3255.83 cm^{-1}, and is assigned to O-H stretch. The peak positioned at 2933.741 cm^{-1},shifted from 2937.14 cm^{-1} ,corresponds to C-H stretching vibrations of the alkane group. The peak at 1623.56 cm^{-1} shifted from 1630.71 cm^{-1} is attributed to the C=C stretching of the alkene group. The peak at 1397.75 cm^{-1} shifted from 1394.02 cm^{-1} can be assigned for the bending of the O-H group. The peak at 1017.56 cm^{-1} shifted from 1019.43 cm^{-1} can be assigned for stretching of the C-N group. Further, the peaks in the fingerprint region positioned at 624.33 cm^{-1} indicates the organosulfur compounds which are known to responsible for the aroma of *allium sativum* (Ezhuthupurakkal *et al.* 2017). The absorption peaks that showed shifts suggests that the addition of the TRPIDC-CH_3 ligand was adsorbed on the surface of SeNPs. These results confirm the formation of the TRPIDC-CH_3 SeNPs, accomplished

by the presence of various flavonoids, saponins, alkaloids, terpenoids, and other biopolymeric agents in *allium sativum* clove extract in *allium sativum* clove extract.

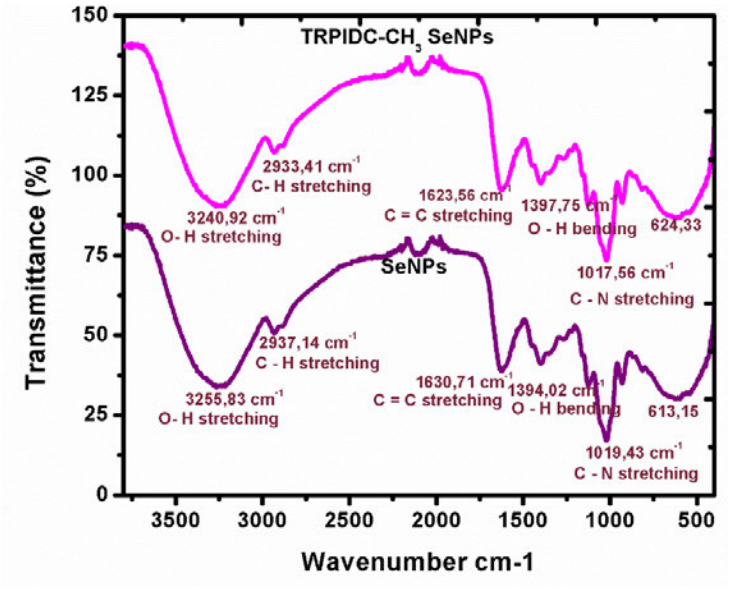

Figure 4.5: FTIR spectrum of TRPIDC-CH_3 SeNPs (**pink**) and uncapped SeNPs (**violet**).

4.1.3 Cytotoxicity activity

The cytotoxicity effects of TRPIDC-CH_3 SeNPs and uncapped SeNPs against MCF-7, A549, and HEK923 cells were determined by the MTT assay. Investigating the cytotoxicity of these nanoparticles to a cancer cell line was necessary to examine how the nanoparticles affected the viability and proliferation of the cells. The percentage cytotoxicity of the nanoparticle was investigated at concentrations of 100 µg/ml and 50 µg/ml, as indicated in Appendix K (Tables 17.1, 17.2, and 17.3.) All experiments were conducted in triplicate and the average absorbance readings were calculated according to the negative solvent control (at 1 % DMSO). The results are displayed in Tables in Appendix K.

There was an overall low cytotoxic effect of the synthesized nanoparticles against MCF-7, A549, and HEK293 cells: the highest percentage activity of 56.9±0.016 % was observed with TRPIDC-CH_3 SeNPs at a 100 µg/ml Appendix K (Table 17.1) against MCF-7. Furthermore, cell growth inhibition of 60.9±0.13 % was seen with uncapped SeNPs against A549. Although overall cytotoxicity was low, a dose-dependent increase in cytotoxic activity was observed for each of the nanoparticles,

as the concentration increased from 50 µg/ml to 100 µg/ml. Low cytotoxic activity was observed with all the screened nanoparticles against HEK293.

The results obtained are comparable to those of Shaheen *et al*., who reported the cytotoxicity activity of GO-ZnO nanocomposites assessed using the MTT assay against MCF-7. Various concentrations of the synthesized nanoparticles ranging from 10 to 100 µg/ml were used. Cell viability was decreased in dose depended approach to 37 %, 47 %, 55 %, 62 %, 79 % and 90 % for MCF-7 cells at the concentrations of 100, 80, 60, 40, 20, and 10 µg/mL, respectively (Shaheen et al. 2018). El-Sayed *et al* synthesized the culture extract of *Monascus purpureus* ATCC16436 grown on sugarcane bagasse under solid-state fermentation and assessed their anticancer activity against MCF-7, HepG2, and normal cell lines NHEM. The results showed that the synthesized samples were less toxic to normal cells (El-Sayed *et al.* 2020).

The microscopic analysis showed the morphological characteristics of untreated or treated cells. The control cells appeared in normal form and were bound to the surface. Nevertheless, the MCF-7 cells that were exposed to TRPIDC-CH_3 SeNPs (Figure 4.6a) lost their normal shape and cell adhesion ability, shrinking and decreasing in cell density (Figure 4.6). Such changes have also been documented using plant-synthesized AgNPs in various cancer cell lines (Vivek *et al*. 2012), indicating that the cytotoxic effect of synthesized AgNPs could be due to the antineoplastic properties and their ability to cause cell death by multiple molecular mechanisms (Farah *et al*. 2016).

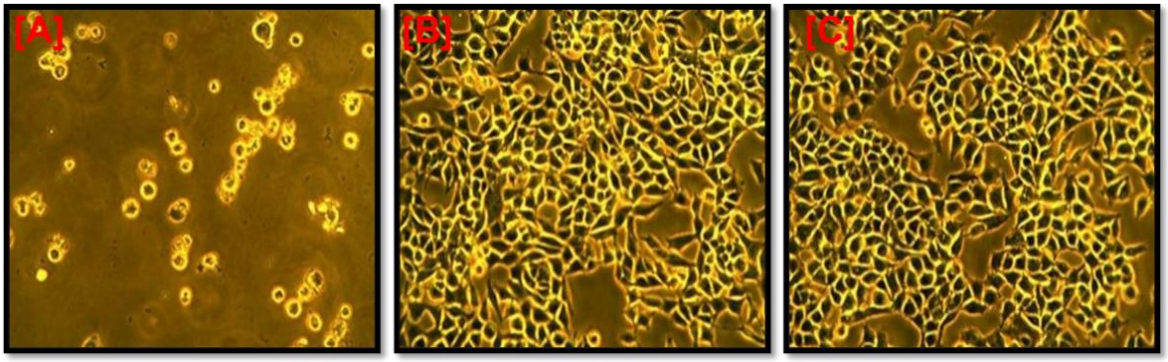

Figure 4.6: morphology of MCF-7 cell (100x magnification), treated with **(A)** TRPIDC-CH_3 SeNPs, **(B)** DMSO (1%), **(C)** untreated.

4.1.4 Protein interaction

In this sub-section, we discuss the spectroscopic interaction of TRPIDC-CH_3 SeNPs with HSA protein in comparison with the uncapped SeNPs. Its UV-Vis, Fluorescence, FTIR investigation are discussed and the modes of binding involved in the complex formation.

4.1.4.1 UV-Vis absorption studies

UV-Vis absorption is a simple and relevant measurement to study structural changes and to prove the formation of a complex. As shown in Figure 4.7, there is a strong absorption band at around 280 nm which was primarily due to $\pi \rightarrow \pi^*$ transition (Pansare *et al.* 2018). HSA shows an absorption peak at 280 nm which is mainly due to the absorption of tryptophan residue (Ishtikhar *et al*. 2015; Mahanthappa *et al*. 2018). Absorbance of this peak (280 nm) gradually increases, without any change in peak position, upon increasing the concentration of TRPIDC-CH_3 SeNPs (or uncapped SeNPs). These observations indicate that there is a structural change (micro-environment) in HSA and the formation of a ground-state complex between HSA and TRPIDC-CH_3 SeNPs (or HSA and uncapped SeNPs) (Prasanth *et al.* 2017; Pansare *et al.* 2018).

Figure 4.7b shows the linear fits of increasing concentration of TRPIDC-CH_3 SeNPs and uncapped SeNPs at 280 nm which confirms the positive correlation between the concentration of TRPIDC-CH_3 SeNPs and uncapped SeNPs The equilibrium established between HSA and TRPIDC-CH_3 SeNPs (or HSA and uncapped SeNPs) during the complex formation is distinct by the chemical equation (10), where K_b is the binding constant. K_b can be obtained according to the method described by Hildebrand group equation (5). The values of $1/(A-A_0)$ were calculated and plotted against quencher concentration 1/[Q] according to equation (5) as shown in Figure 4.7A and B. After the linear fit, the calculated value of K_b is based on the slope, and the intercept of the plot is about 6.75×10^5 M^{-1} for TRPIDC-CH_3 SeNPs (1.20×10^6 M^{-1} uncapped SeNPs). Based on these results uncapped SeNPs showed better interaction.

$$\text{HSA} + \text{TRPIDC-CH}_3\text{ SeNPs} \xleftrightarrow{K_b} \text{HSA}\ldots\text{TRPIDC-CH}_3\text{ SeNPs} \qquad (10)$$

$$K_b = \frac{[\text{HSA}.....\text{TRPIDC}-\text{CH3 SeNPs}]}{[\text{HSA}]\ \text{x}\ [\text{TRPIDC}-\text{CH3 SeNPs}]} \qquad (11)$$

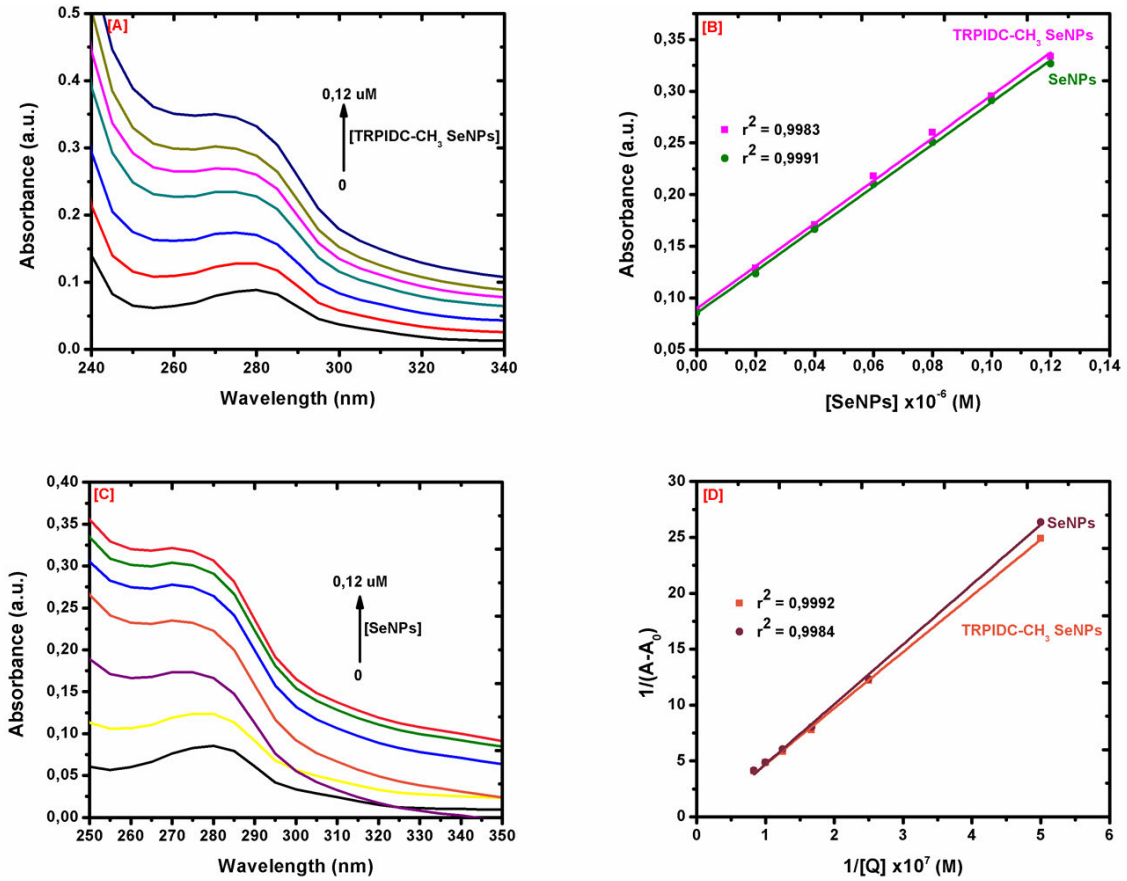

Figure 4.7: **(A)** Absorbance spectrum of HSA upon the addition of TRPIDC-CH_3 SeNPs **(B)** Linear fit for both the systems **(C)** Absorbance spectrum of HSA upon the addition of SeNPs **(D)** Plot of 1/(A - A_0) versus 1/[Q] for both systems.

4.1.4.2 Fluorescence quenching study

Figure 4.8a shows fluorescence of HSA with fixed increasing concentrations of TRPIDC-CH_3 SeNPs at 310 K. The fluorescence intensity of HSA at the characteristic broad emission band at 345 nm decreased when the concentration of TRPDC-CH_3 SeNPs increased and no obvious wavelength shift was observed: this indicated a strong interaction between HSA and TRPIDC-CH_3 SeNPs. Comparable results for the uncapped SeNPs at Appendix A: were observed. The fluorescence intensity of HSA is mostly from the tryptophan residues when the excitation wavelength is 280 nm (Bardajee *et al.* 2016). Thus, the decrease is due to the interaction between TRPDC-CH_3 SeNPs and tryptophan, the adding of TRPDC-CH_3 SeNPs causes a change in the structure of HSA and it exposes the tryptophan to the aqueous solution, therefore the molecular conformation of the HSA was effected, which agreed to the recent studies (Bardajee *et al.* 2016).

The Stern−Volmer equation (6) was used to analyze the fluorescence quenching data. The Stern-Volmer plots of F_0/F vs [Q] at three different temperatures (298, 304, and 310 K) is presented in Figure 4.8c, and values of K_{SV} and K_q estimated by slope, K_q was calculated from fluorescence lifetime (10^{-8} s) of HSA. The estimated K_{SV} and K_q at three different temperatures are assembled in Table 4.2. Fluorescence quenching processes are generally categorized as either dynamic quenching or static quenching and can be distinguished by their varying temperature dependency. The quenching constants decrease with the rise in temperature for static quenching, and the reverse trend for dynamic quenching is observed (Prasanth *et al.* 2017).

Based on Table 4.2 results of the K_{SV} and K_q, it can be implied that the essence of the quenching is not static, but probably dynamic, resulting in forming complexes between TRPDC-CH_3 SeNPs and HSA. Static quenching for uncapped SeNPs. By plotting the double logarithm curve log $(F_0-F)/F$ versus log[Q] (Figure 4.8d), K_b and *n* were calculated from intercept and slope (Table 4.2). The value K_b decreased with increasing temperature, showing the instability of the HSA-SeNPs system at higher temperatures, and the reverse effect was observed for HSA-TRPIDC-CH_3 SeNPs. The value of *n* also indicated that there was one independent class of binding site on HSA for the abovementioned systems which were ~ 1 (Table 4.2).

Table 4.2: The K_{SV}, K_q, K_b, and n of the HSA-TRPIDC-CH_3 SeNPs (and uncapped SeNPs).

SeNPs	T (K)	K_{sv} (10^6 M^{-1})	K_q (10^{14} M^{-1} S^{-1})	r^2	K_b (M^{-1})	n	r^2
TRPIDC-CH_3	298	5,87	5,87	0,997	$5,46x10^7$	1,13	0,995
	304	6,78	6,78	0,999	$1,56x10^9$	1,37	0,998
	310	6,89	6,89	0,996	$1,92x10^9$	1,37	0,998
Uncapped	298	7,53	7,53	0,996	$8,17x10^7$	1,17	0,999
	304	6,74	6,74	0,995	$7,94x10^7$	1,16	0,999
	310	5,38	5,38	0,991	$1,23x10^7$	1,07	0,998

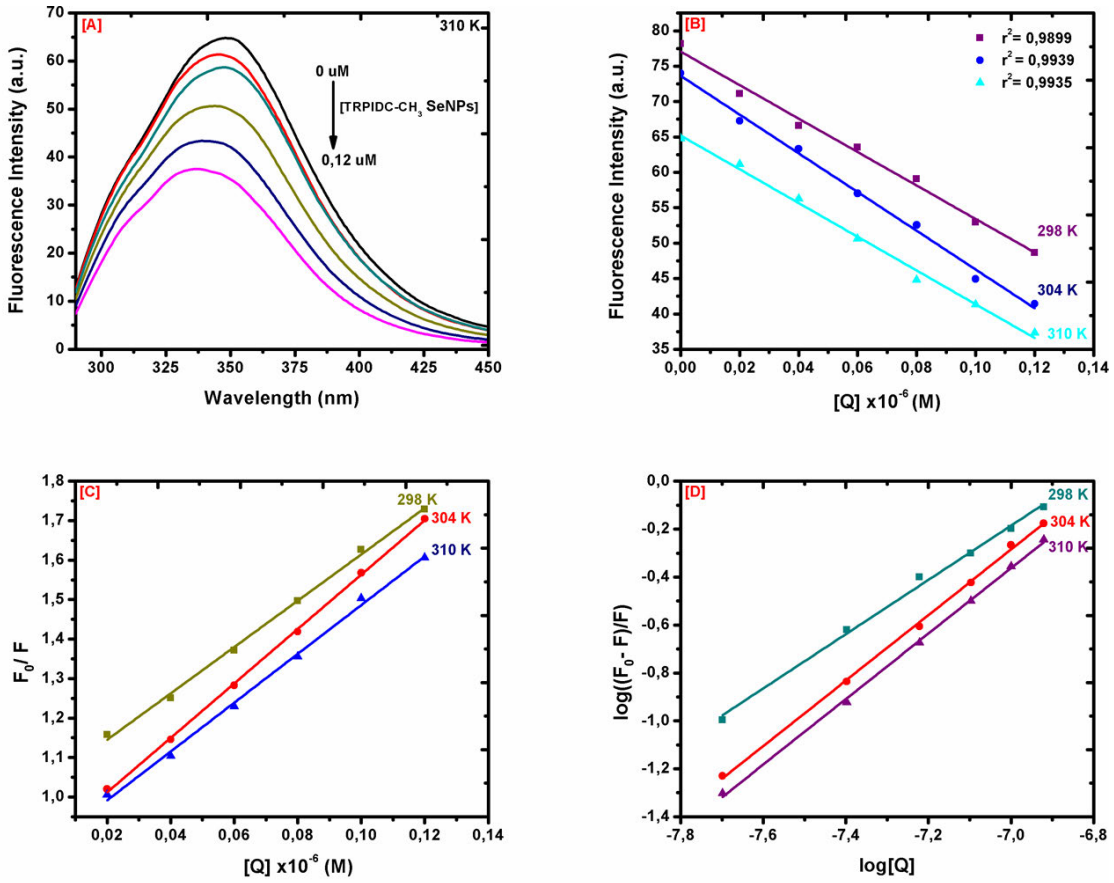

Figure 4.8: **(A)** Fluorescence spectrum of HSA in the presence of different concentrations of TRPIDC-CH_3 SeNPs. **(B)** a linear fit of the complex intensities vs increasing concentration sof TRPIDC-CH_3 SeNPs at 345 nm at different temperatures. **(C)** Stern–Volmer curves for the binding of HSA with TRPIDC-CH_3 SeNPs at different temperatures. **(D)** log[(F_0 / F)/F] versus log[Q] plots for HSA versus TRPIDC-CH_3 SeNPs at different temperatures.

4.1.4.3 Mode of binding

Biological molecules bind with smaller molecules through interactions like hydrogen bonding, van der Waals forces, electrostatic, hydrophobic and hydrophilic interactions (Pansare *et al.* 2018). Thermodynamic properties like change in entropy (ΔS), change in enthalpy (ΔH), and change in free energy (ΔG) were employed to determine the strategic forces involved in the formation between HSA and TRPIDC-CH_3 SeNPs (or uncapped) complex. Using equation (8), ΔH and ΔS values were attained by the van't Hoff plot ln(K_b) vs 1/T (Figure 4.9), and change in free energy (ΔG) is determined from the Gibbs–Helmholtz equation (9) (Mahanthappa *et al.* 2018).

Table 4.3 shows the thermodynamic parameters (ΔH, ΔS, and ΔG) of HSA-TRPIDC-CH_3 SeNPs and HSA-SeNPs complexes. Based on Table 4.3, the positive sign of ΔH

and negative sign of ΔG indicates that the binding process is endothermic and spontaneous. The positive signs of Δ*H* and Δ*S* indicate the involvement of hydrophobic interactions HSA -TRPIDC-CH_3 AgNPs complex formation. For HSA-SeNPs complex formation, van der Waals or hydrogen bonding were involved because of the negative sign of Δ*H* and Δ*S* with the binding process that is exothermic and spontaneous. The hydrophobic interactions are relatively stronger than van der Waals forces or hydrogens bond (Atkins *et al.* 2011).

Table 4.3: Thermodynamics parameters of HSA and nanoparticles interaction.

Parameters	TRPIDC-CH_3 SeNPs	Uncapped SeNPs
Δ***H*** (kJ mol^{-1} K^{-1})	226,46	-170.97
Δ***S*** (J mol^{-1} K^{-1})	908,98	-415,33
Δ***G***(kJ mol^{-1} K^{-1})	-44,00	-47.30
Forces	hydrophobic interactions	hydrogen or van der Waals

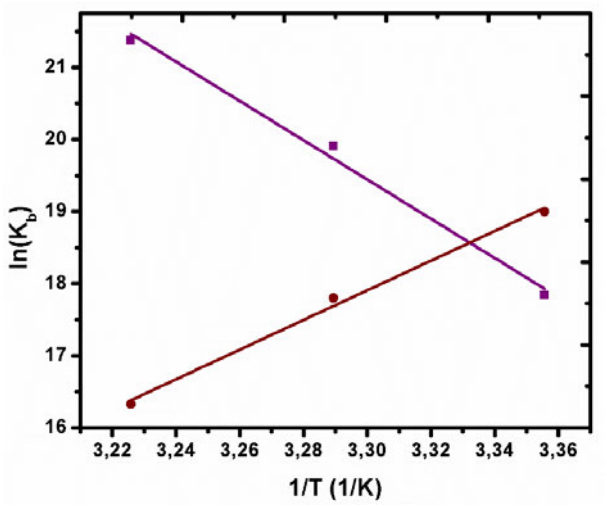

Figure 4.9: Van't Hoff plot of (**Purple**) HSA-TRPIDC-CH_3 SeNPs and (**Brown**) HSA-SeNPs.

4.1.4.4 FTIR studies

FTIR spectroscopy was used to track changes in the secondary structure of HSA and its dynamics when interacting with SeNPs, as the FTIR spectrum can reflect changes in the three-dimensional structure of proteins and the conformation of secondary structures in the protein-nanoparticle complex. The FTIR spectrum of HSA comprises several amide I and amide II bands. Amide I with a peak in the 1600 – 1700 cm-1 region associated with the C=O section is responsive to changes in the HSA secondary structure (Bardajee *et al.* 2016; Rezanejade Bardajee *et al.* 2017). The

amide I peak of HSA before and after interaction with TRPIDC-CH_3 SeNPs are shown in Figure 4.10. The peak position of amide I shifted from 1638.16 cm^{-1} to 1641.89 cm^{-1} after the addition of TRPIDC-CH_3 SeNPs. These results confirm the changes in the secondary structure of HSA, hence the complex formation (HSA -TRPIDC-CH_3 SeNPs).

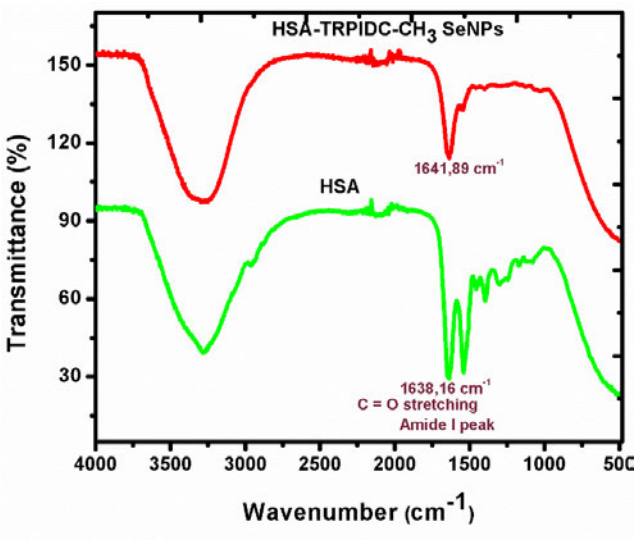

Figure 4.10: FTIR spectra of HSA before and after interactions with TRPIDC-CH_3 SeNPs.

4.1.5 Electrochemistry

Herein we are looking at the electrochemical behavior of ATP under indirect quantification whereby a more electroactive species ($K_3[Fe(CN)_6]/K_4[Fe(CN)_6]$) peak in used to determine the electrochemical behavior of the desired analyte. Glassy carbon electrode (GCE) was modified by immobilizing TRPIDC-CH_3 SeNPs with Dual enzyme composite (GO:Hex) in comparison to the uncapped SeNPs.

4.1.5.1 Electrochemical characterization

The CV of the response of ATP on a bare and modified GC electrode in 10 mL PBS (0.1 M, pH 7) containing 1 mM of $K_3[Fe(CN)_6]/K_4[Fe(CN)_6]$ at different stages were recorded at a scan rate of 100 mV/s (Figure 4.11a.). The CV of bare GCE (curve i) showed a well-defined reversible peak of $[Fe(CN)_6]^{3-/4-}$ with I_a = 3.98 µA and I_c = −4.43 µA peak currents. There was an increase in the anodic peak current by 69 % (12.99 µA) at the MWCTNs/GC electrode (curve ii) and and a shift in peak potential from 0.40 V to 0.23 V. When using SeNPs/MWCNTs/GC electrode as shown in curve iii, there

was a further increase in peak current by 46 % (24.18 µA) and peak potential from 0.23 V to 0.26 V. At the TRPIDC-CH_3SeNPs/MWCNTs/GC electrode there was a further increase in peak current by 23 % (31.20 µA) with a shift back in peak potential from 0.26 V to 0.23 V shown in curve iv.

The modification of TRPIDC-CH_3 SeNPs on the GCE increased the surface area and thus electron transfer between the electrode and solution was improved with incremental changes in peak current. When GO:Hex enzyme composite was introduced on the GCE, I_a increased further to 41.30 µA (24 %) as shown in curve v. This was a clear indication that electrode modification by enzyme effectively enhance the conductive activity of electrode (Sarpong *et al.* 2020). The introduction of TRPIDC-CH_3 SeNPs and GO: Hex enzyme composites on GCE recorded the highest peak current of 54.93 µA an increament of 28 % (curve vi) owing to the synergistic effect of TRPIDC-CH_3 SeNPs, GO: Hex and GCE with excellent electrical conductivity and high surface area. The average shift in peak potential for curves was ± 0.025 V.

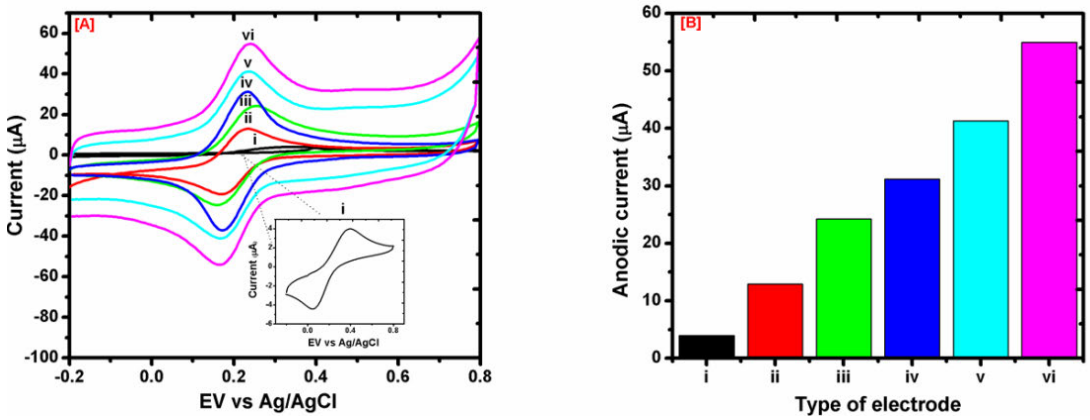

Figure 4.11: **(A)** Cyclic voltammograms of 0.02 mM ATP at (i) bare GCE, (ii) MWCNTs/GCE , (iii) SeNPS/MWCNTs/GCE,(iv) TRPIDC-CH_3 SeNPs/MWCNTs/GCE, (v) GO:Hex/SeNPs/MWCNTs/GCE and (vi) GO:Hex/TRPIDC-CH_3 SeNPs/MWCNTs/GCE. **(B)** histogram displaying the current responses at corresponding electrodes.

4.1.5.2 Effect of pH

To evaluate the electrochemical behavior of GO:Hex/SeNPs/MWCNTs/GC and GO:Hex/TRPIDC-CH_3SeNPs/MWCNTs/GC electrodes in different pH, we conducted the CV measurement with ATP (0.02 mM) in 0.1 MPBS containing 1 mM $K_4[Fe(CN)_6]/K_3[Fe(CN)_6]$ at pH ranging from 5 to 9 under the scan rate of 100 mV/s. In its oxidized form, ATP has a furan moiety, where the redox couple of furan

molecules are shifted with the rise in pH to less positive values as seen in Figure 4.12a and c (Manjubaashini *et al.* 2019). As the pH values of supporting electrolyte were increased, the oxidized species of ATP became more stable as indicated by the increasing ratio of Ip_c/Ip_a accumulated in Appendix J (Table16.1) (Dar *et al.* 2016). There was a decrease in the anodic peak currents and a shift in peak potentail to the more positive values in this pH range (Figure 4.12b and d), which is due to deprotonation (Manjubaashini *et al.* 2019).

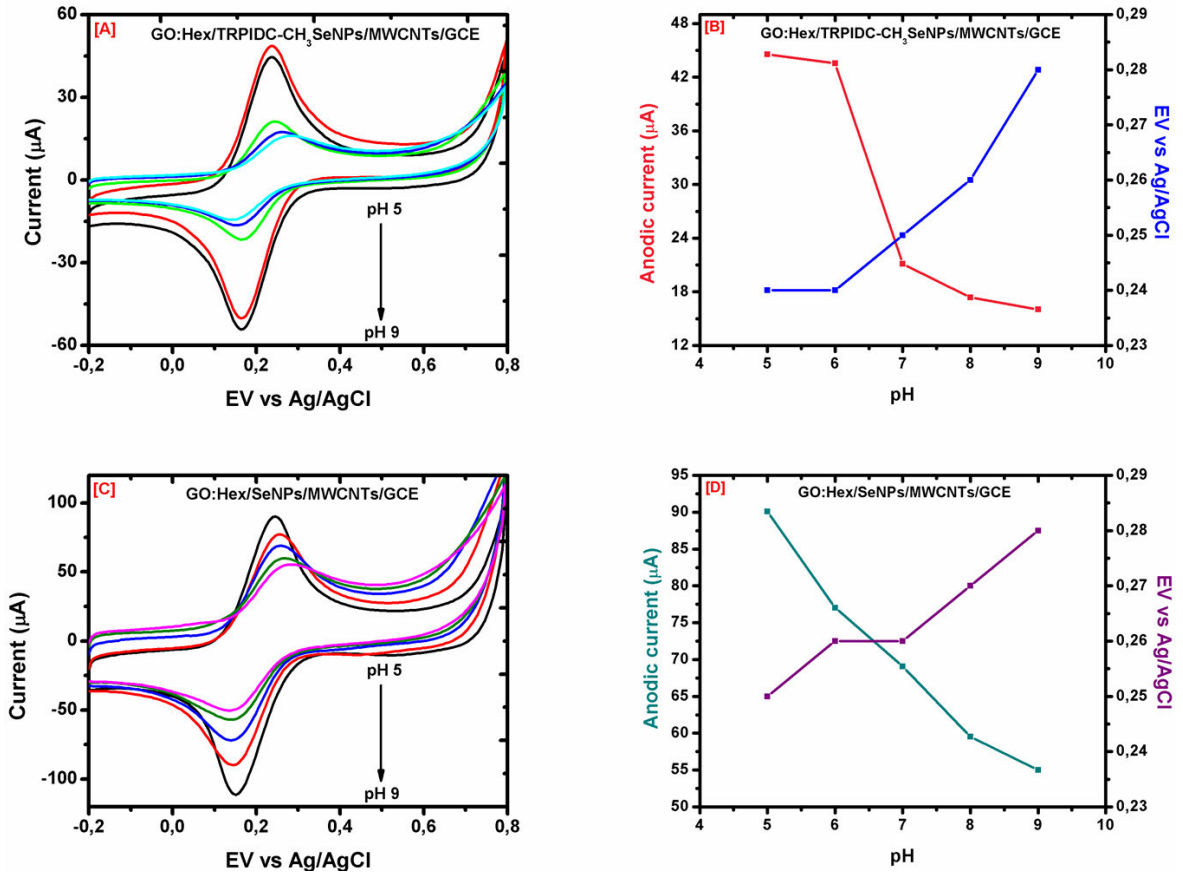

Figure 4.12: Effects of pH in 0.1 M PBS using **(A)** GO:Hex/TRPIDC-CH_3 SeNPs/MWCNTs/GCE **(B)** corresponding plot of current vs pH, **(C)** GO:Hex /SeNPs/MWCNTs/GCE using 0.02 mM ATP and **(D)** corresponding plot of current vs pH.

4.1.5.3 Effect of Scan Rate

The effect of scan rate on anodic and cathodic peak current of GO:Hex/TRPIDC-CH_3SeNPs/MWCNTs/GC and GO:Hex/SeNPs/MWCNTs/GC electrodes upon addition of 0.02 mM ATP in 0.1 M PBS containing 1 mM $K_4[Fe(CN)_6]/K_3[Fe(CN)_6]$ at pH 7 was analyzed at a scanning rate of 10–100 mV/s. The current (I) vs. voltage (V) function indicates the change in peak potential to more positive and negative in the

reverse scan as the scan rate is increased (Figure 4.13a and c). The electrochemical activity of PBS at pH 7 is also observed to be quasi-reversible. In addition, both oxidation and reduction peak currents were increased with increasing scan rate Excellent linearity was observed when plotting current against the scan rate (Figure 4.13b and d).The relationship between the redox peak currents and the scan rates were correlated at anodic peak = 0.9993 and cathodic peak = 0.9995 for GO:Hex/TRPIDC-CH_3 SeNPs/MWCNTs/GCE and for the anodic, and cathodic peaks was 0.9969 and 0.9886, respectively for GO:Hex/SeNPs/MWCNTs/GCE.

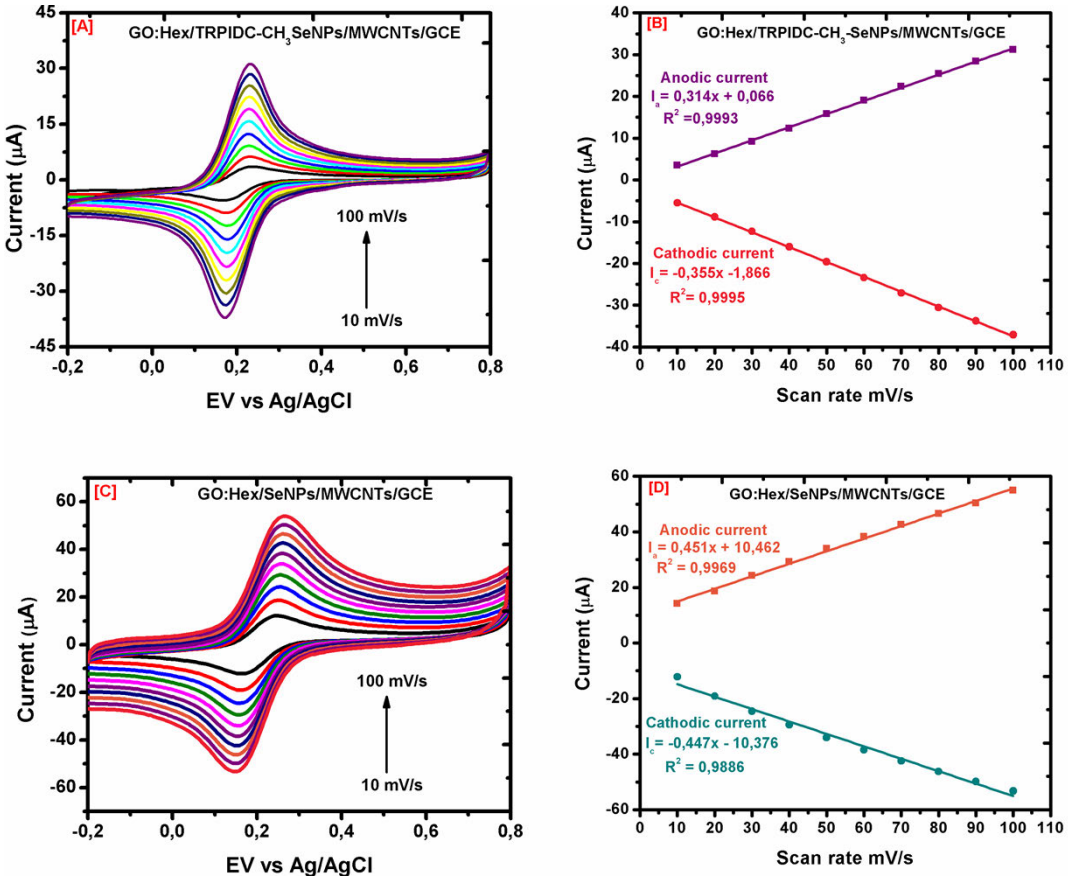

Figure 4.13: Effects of scan rate from 10 to 100 mV/s **(A)** GO:Hex/TRPIDC-CH_3 SeNPs/MWCNTs/GCE **(B)** corresponding plot of current vs scan rate, **(C)** GO;Hex/SeNPs/MWCNTs/GCE using 0.02 mM ATP and **(D)** corresponding plot of current vs scan rate.

4.1.5.4 Effect of Deposition Time

The effects of deposition time were investigated on anodic peak current of GO:Hex/TRPIDC-CH_3SeNPs/MWCNTs/GC and GO:Hex/SeNPs/MWCNTs/GC electrodes upon addition of 0.02 mM ATP in 0.1 M PBS containing 1 mM $K_4[Fe(CN)_6]/K_3[Fe(CN)_6]$ at pH 7, under the time interval of 30 to 150 s. For the

GO:Hex/SeNPs/MWCNTs/GC electrode (Figure 4.14b) the current was stable up to 60s and for the GO:Hex/TRPIDC-CH_3SeNPs/MWCNTs/GCE electrode in Figure 4.14a, the current decreased with the increase in deposition time.

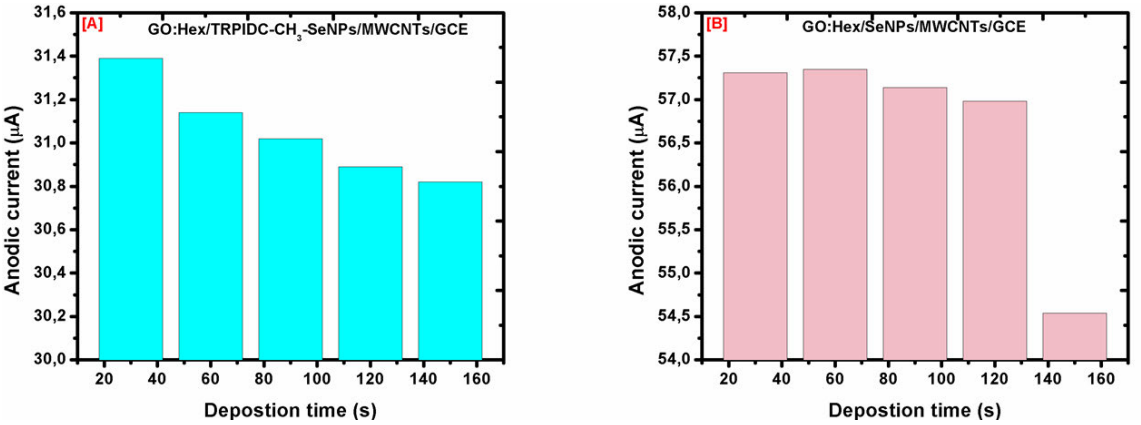

Figure 4.14: Effects of deposition time on the oxidation current from 30 to 150 s in 0.02 mM ATP **(A)** GO:Hex/TRPIDC-CH_3 SeNPs/MWCNTs/GCE **(B)** GO:Hex/SeNPs/MWCNTs/GCE.

4.1.5.5 Indirect SWV Technique Quantitative Detection of ATP

Indirect electrochemical detection requires strong electroactive species like $[Fe(CN)_6]^{3-/4-}$, where the analyte of interest will be studied by monitoring the current peak of the electroactive species upon addition of analyte. The electrochemical activity of ATP using the $[Fe(CN)_6]^{3-/4-}$ peak involves at least two enzyme reactions, the enzyme conversion may be based on a competitive reaction of the common substrate, or the enzyme conversion may appear sequentially, which is related to the The two enzymes hexokinase (Hex) and glucose oxidase (GO) enzymes competing for the glucose substrate were used to build the biosensor.

The square wave voltammograms (SWV) of the response of ATP on the GO:Hex/TRPIDC-CH_3 SeNPs/MWCNTs/GC and GO:Hex/SeNPs/MWCNTs/GC electrodes in 10 mL PBS (0.1 M, pH 7) containing 1 mM of $K_3[Fe(CN)_6]/K_4[Fe(CN)_6]$ were recorded at a scan rate of 100 mV/s (Figure 4.15a and c). Figures 4.15a and c shows an increase in the $[Fe(CN)_6]^{3-/4-}$ peak as the ATP concentration increases from 0.02 to 0.12 mM, it can be seen that the electrode senses the ATP response. Enzymes operate under physiological conditions and can thus be perfectly applied in in vitro measurements. When ATP is present in the solution, Hex converts ATP to reduce the local glucose concentration. The decreased glucose concentration is detected by GO

and results in a current signal that is proportional to the ATP concentration (Weber 2014). Hence, the increase in the peak current of $[Fe(CN)_6]^{3-/4-}$.

The SWV response of ATP different concentrations, displayed a linear relationship (Figure 4.15b and d) between the concentrations of ATP and the peak currents of $[Fe(CN)_6]^{3-/4-}$, with correlation coefficients of $R^2 = 0.9729$ and a limit of detection (LOD) of 0,05 mM and a limit of quantification (LOQ) of 0,17 mM for the GO:Hex/TRPIDC-CH_3 SeNPs/MWCNTs/GC electrode. A correlation coefficients of $R^2 = 0.9814$ and a limit of detection (LOD) of 0,04 mM and a limit of quantification (LOQ) of 0,14 mM for the GO:Hex/SeNPs/MWCNTs/GC electrode. Li et al and Liu et al successfully detected ATP indirectly using a redox probe with LOD of 0.03 pM and 3 nM respectively (Li *et al.* 2019; Liu *et al.* 2020).

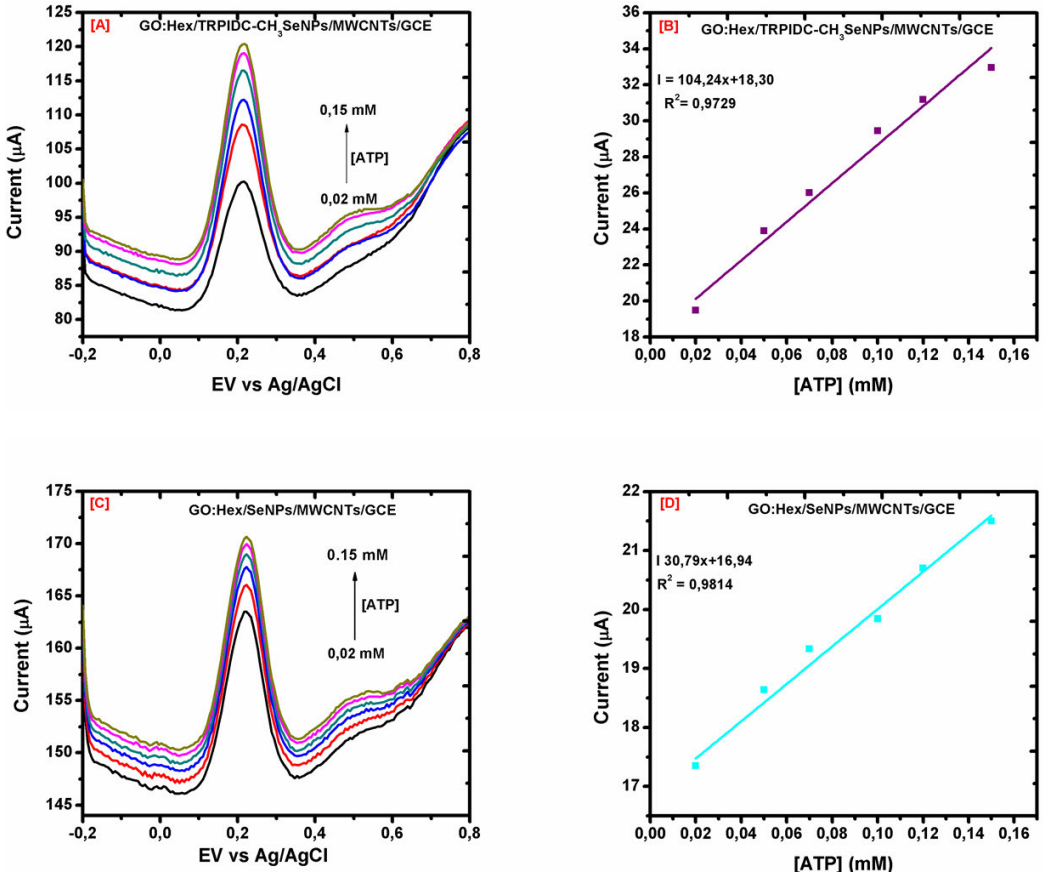

Figure 4.15: **(A)** SWV voltammogram GO:Hex/TRPIDC-CH_3 SeNPs/MWCNTs/GCE at different concentrations (0.02 – 0.15 mM), **(B)** Corresponding calibration curve showing linear dependence of the peak currents versus concentration of ATP, **(C)** SWV voltammogram GO:Hex/SeNPs/MWCNTs/GCE and **(D)** Corresponding calibration curve.

4.1.5.6 Reproducibility and Stability

The lifetime of the formed electrochemical biosensor is of particular significance, as the coating will wear off during the stirring and cleaning time. Hence the stability was observed over a range of 11 runs for one day using the same electrode coating. The current response of GO:Hex/SeNPs/MWCNTs/GCE and GO:Hex/TRPIDC-CH_3SeNPs/MWCNTs/GCE and, on the $[Fe(CN)_6]^{3-/4-}$ peak was observed over the addition of 20 uM ATP (n = 11) to access the stability of the biosensors. As the number of runs and the concentration of ATP increased (Figure 4.16a and b), the sensitivity decreased due to deterioration of the performance of the biosensor. It also confirmed that the system is primarily driven by an irreversible adsorption process. (Mpanza *et al.* 2014). Resulting in the saturation of the electrode's surface.

The insert of Figure 4.16a shows that the GO:Hex/TRPIDC-CH_3 SeNPs/MWCNTs/GCE biosensor maintained a non-linear direct co-relationship response from run 1 to 5 and a drop in current after 5^{th} run, therefore the electrochemical enzymatic biosensor developed was stable up to 5 runs on the same day with the same coating. The GO:Hex/SeNPs/MWCNTs/GCE biosensor maintained a positive co-relation response from runs 1 to 7 and after the 7^{th} run current dropped shown in the of insert of Figure 4.16b. The GO:Hex/SeNPs/MWCNTs/GCE was more stable in terms of runs than GO:Hex/TRPIDC-CH_3 SeNPs/MWCNTs/GCE, the addition of the pyrazole ligand to the SeNPs weaken its electrochemical stability.

The reproducibility of the biosensor was examined by doing the three different runs with three different electrodes with the same coating and ATP concentration range (0-12 mM) under optimum condition. Figure 4.16c and d shows the effect of current for each concentration. The biosensors showed good reproducibility with an average relative standard deviations (n=3) of 1.17 for the GO:Hex/SeNPs/MWCNTs/GCE and 2.30 for GO:Hex/TRPIDC-CH_3 SeNPs/MWCNTs/GCE. The excellent reproducibility and sensitivity could be associated with the most stable metal nanoparticles formed by selenium. These results tell us that the data is closely gathered around the mean and GO:Hex/SeNPs/MWCNTs/GCE is more precise, because of the smaller the RSD (Owen 2010).

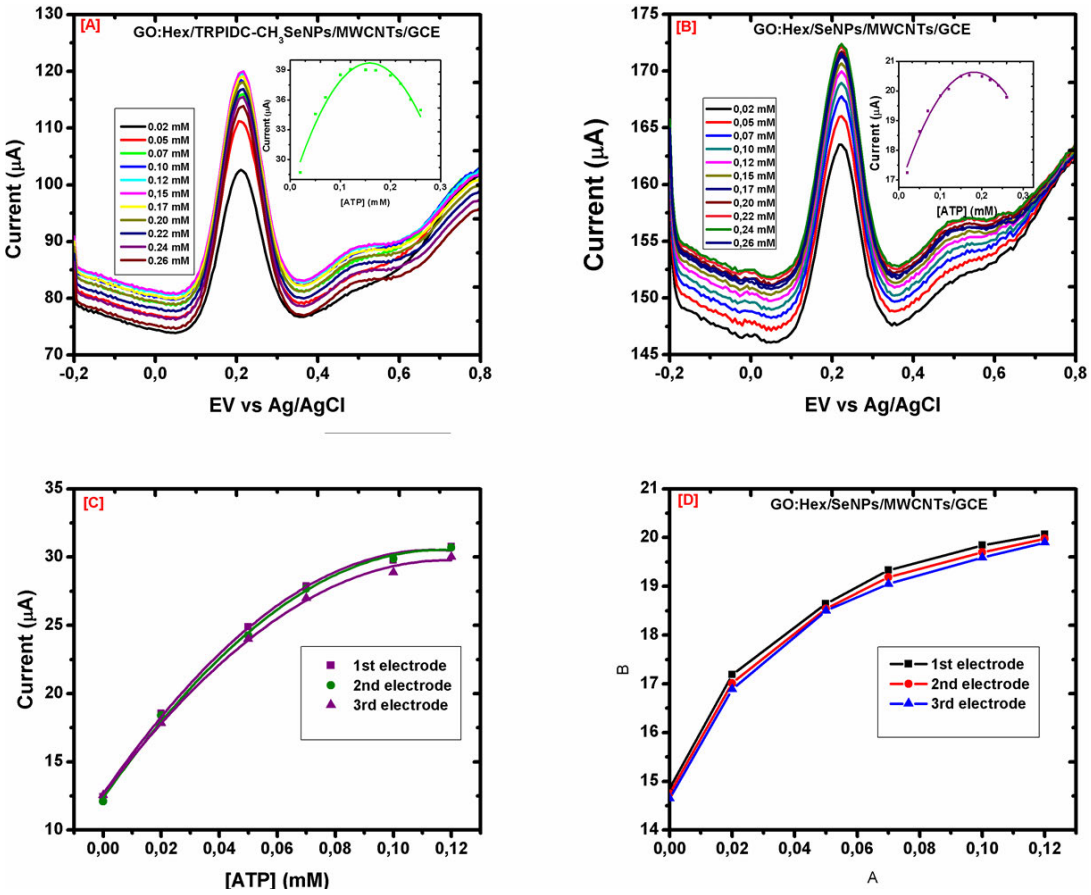

Figure 4.16: Square wave voltammograms of **(A)** GO:Hex/TRPIDC-CH_3 SeNPs/MWCNTs/GCE and insert of line graph showing the effect of current and **(B)** GO:Hex/SeNPs/MWCNTs/GCE with insert of line graph showing the effect of current. The repoduciblity line graphs **(C)** GO:Hex/TRPIDC-CH_3 SeNPs/MWCNTs/GCE and **(D)** GO:Hex/SeNPs/MWCNTs/GCE.

4.1.5.7 Real Sample analysis

The developed enzymatic biosensors were used for the detection of ATP in commercially available, Swanson peak ATP and Vita-thion tablet samples. The tablets were crushed and dissolved with deionized water and adjusted to the relevant pH. The samples were spiked with three different concentrations (0.05, 0.07, and 0.10 mM) of the standard solution of ATP and then quantified with SQW method (Table 4.4). The GO:Hex/TRPIDC-CH_3 SeNPs/MWCNTs/GCE had high recovery percentage compared to GO:Hex/SeNPs/MWCNTs/GCE.

Table 4.4: Results for the detection of ATP in spiked samples analysed using the electrodes.

	GO:Hex/TRPIDC-CH_3SeNPs/MWCNTs/GCE				GO:Hex/SeNPs/MWCNTs/GCE			
Samples[a]	**[ATP] (mM)**	**Recovery (%)**	**RSD (%)**	**Relative Error[b]**	**[ATP] (mM)**	**Recovery (%)**	**RSD (%)**	**Relative Error[b]**
Swanson								
Spiked 1	0,07	97	1,92	-2,67	0,07	89	4,42	-11,12
Spiked 2	0,05	94	1,35	-4,04	0,05	87	4,62	-12,93
Spiked 3	0,1	95	1,33	-4,85	0,1	88	5,87	-11,54
Vita-thion								
Spiked 1	0,07	91	0,49	-8,78	0,07	85	3,03	-14,54
Spiked 2	0,05	84	2,8	-16,16	0,05	82	2,89	-18,08
Spiked 3	0,1	87	0,43	-12,68	0,1	87	6,57	-13,41

[a] Average of three measurements, [b] relative error = (absolute error/true value)*100

4.2 CASE STUDY 2: Silver Nanoparticles

The findings of TRPIDC-CH_3 AgNPs (capped) are discussed in this subsection in relation to uncapped AgNPs. We review its interaction studies with HSA proteins, which have the potential to be used in the drug delivery sector, assess its anticancer activity and also the electrochemical actions of ATPs using a glassy carbon electrode (GCE) modified with TRPIDC-CH_3 AgNPs and uncapped AgNPs in combination with glucose oxidase (GOD) and hexokinase (Hex) composite enzymes.

4.2.1 Characterization of extract

4.2.1.1 Phytochemical screening

The *pelargonium graveolens* plant is reported to contain significant amounts of flavonoids, alkaloids, phenolic acids, tennis, and terpenoids (Machalova *et al.* 2015; Mohammadlou *et al.* 2017; Ennaifer *et al.* 2018). The phytochemical screening test was conducted to classify the active biomolecules in the leaf extracts responsible for the synthesis of AgNPs.The leaf extract tested positive for flavonoids, phenolic acids, terpenoids and tannins (Table 4.5), which may influence the mechanism of reduction and stabilization of the synthesized AgNPs. These findings indicate that the major reducing and stabilizing compounds (flavonoids, phenolic acids, terpenoids and tannins) of the leaf extract had OH and C=C groups in their chemical structures.

Table 4.5: Characteristics of phytochemicals found in the *allium sativum* extract.

Compound class	Phytochemical test	Literature	References
Phenolic acids	+ +	+	(Mohammadlou *et al.* 2017)
Flavonoids	+ +	+	(Mohammadlou *et al.* 2017; Ennaifer *et al.* 2018)
Tannins	+ +	+	(Mohammadlou *et al.* 2017; Ennaifer *et al.* 2018)
Terpenoids	+ +	+	(Mohammadlou *et al.* 2017; Ennaifer *et al.* 2018)

++ positive current study; + literature

4.2.1.2 FTIR studies

FTIR was conducted to classify the biomolecules responsible for the reduction and stabilization of AgNPs in the *pelargonium graveolens* leaf extract. The FTIR spectrum (Figure 4.17) showed a widest absorption at 3322.92 cm^{-1}, which is attributed to the stretching vibrations of O-H. Furthermore, the suppressed bands at 1634.44 cm^{-1}, stretching vibration of alkane groups (C=C), the peak at 1455.52 cm^{-1} is assigned to the O-H bending and the absorption peak at 1332.52 cm^{-1} corresponded to the C-N stretching of aromatic amine. The presence of these functional groups in the FTIR spectrum of *pelargonium graveolens* leaf extract has been also reported by Pandian *et al* and Mohammadlou *et al* (Pandian *et al.* 2013; Mohammadlou *et al.* 2017).

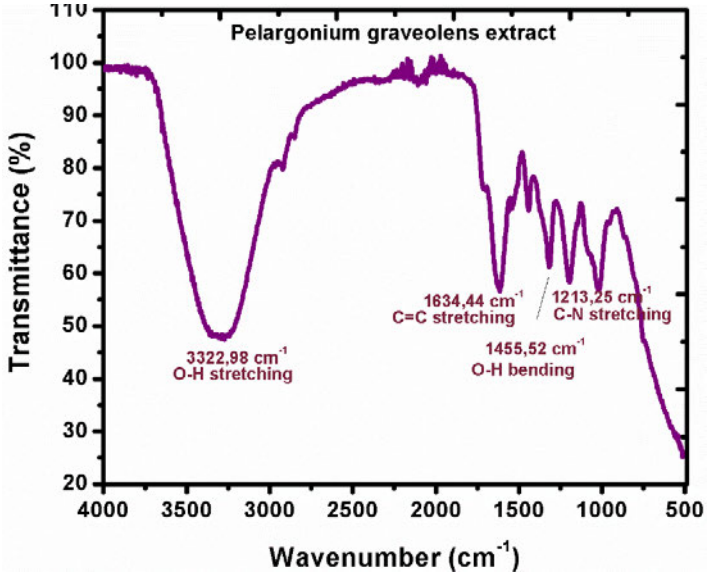

Figure 4.17: FTIR spectrum of *pelargonium graveolens* leaf extract.

4.2.2 Characterization of AgNPs

Figure 4.18 shows the visual studies of the synthesized TRPIDC-CH_3 AgNPs using *pelargonium graveolens* leaf extract. The colour changed from pale yellow to dark brown due to the reduction of silver ions to silver metal after 24 hours of incubation at 37 ^{o}C. This reduction is due to the surface plasmon resonance (SPR), that strongly depends on the particle size, dielectric medium and chemical surroundings (Kumar *et al.* 2017). The formation of the colour dark brown is a formal indication of the formation of TRPIDC-CH_3 AgNPs synthesized using *pelargonium graveolens* leaf extract. Mohammadlou *et al* and Pandian *et al* also produce dark brown coloured AgNPs using *pelargonium graveolens* leaf extract (Pandian *et al.* 2013; Mohammadlou *et al.* 2017).

Medda *et a*l also reported dark brown using aloe vera leaf extract (Medda *et al.* 2015). Also, colours such as yellow-brown (Baraka *et al.* 2017) and yellowish-orange (Kumar *et al.* 2017) have been reported for the formation of AgNPs using different plant extracts.

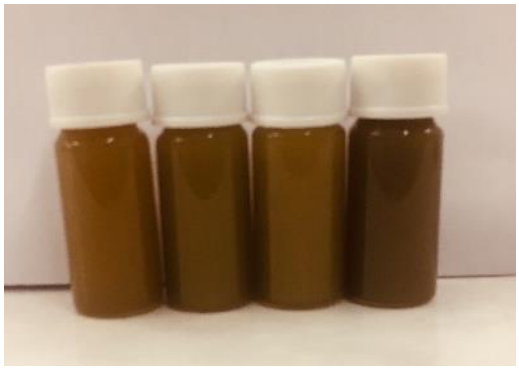

Figure 4.18: Green synthesized TRPIDC-CH_3 AgNPs.

4.2.2.1 UV-Visible Spectroscopy

TRPIDC-CH_3 AgNPs were detected by a UV-Vis spectrophotometer in the range of 200 to 800 nm. The maximum absorption spectra of TRPIDC-CH_3 AgNPs showed a sharp absorbance maximum peak at 445 nm as shown in Figure 4.19. The TRPIDC-CH_3 AgNPs exhibits dark brown colour in aqueous solution due to the excitation of surface plasmon vibrations. The colour exhibited by metallic nanoparticles is due to the coherent excitation of all the “free” electrons within the conduction band, leading to an in-phase oscillation which is known as SPR (Ali *et al.* 2016; Saha *et al.* 2019). Here TRPIDC-CH_3 AgNPs synthesized using *pelargonium graveolens* leaf extracts were stable for at least one month when stored at 4 ^{o}C. In the present study the uncapped AgNPs had the same result. Mohammadlou *et al* and Pandian *et al* reported a maximum absorption peak at 440 nm of AgNPs using *pelargonium graveolens* leaf extracts (Pandian *et al.* 2013; Mohammadlou *et al.* 2017). Tippayawat *et al* report 420 nm using aloe vera leaf extract (Tippayawat *et al.* 2016).

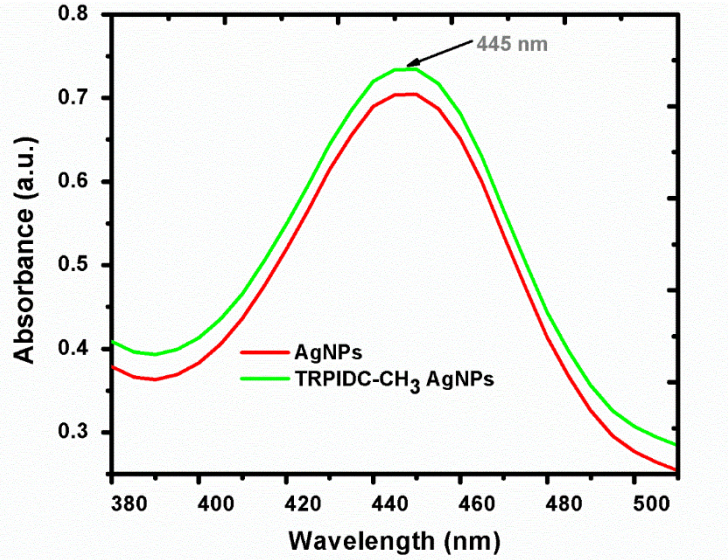

Figure 4.19: UV-Vis spectrum of TRPIDC-CH_3 AgNPs (**lime**) and uncapped AgNPs (**red**) synthesized.

4.2.2.2 Morphology and Particle Size Analysis

The HR-TEM results suggested that the average diameter of TRPIDC-CH_3 AgNPs of spherical nanoparticles, which are monodispersed in nature, was found to be 45 nm (Figure 4.20a), which is double the size of uncapped AgNPs 18 nm (Figure 4.20b). Figure 4.20c and d, are the size distribution histograms formulated using image j software, the size distribution ranges from 5 – 95 nm for both capped and uncapped AgNPs. Capped nanoparticles are expected to be higher in size when compared to the uncapped (Satgurunathan *et al.* 2017; Saha *et al.* 2019). However, the TRPIDC-CH_3 AgNPs were double in size, as we can see from (Figure 4.20a) that agglomeration played a big part in the size of TRPIDC-CH_3 AgNPs. The addition of TRPIDC-CH_3 ligand may be the main cause of agglomeration since (Figure 4.20b) can be seen that the particles are less agglomerated and are well dispersed.

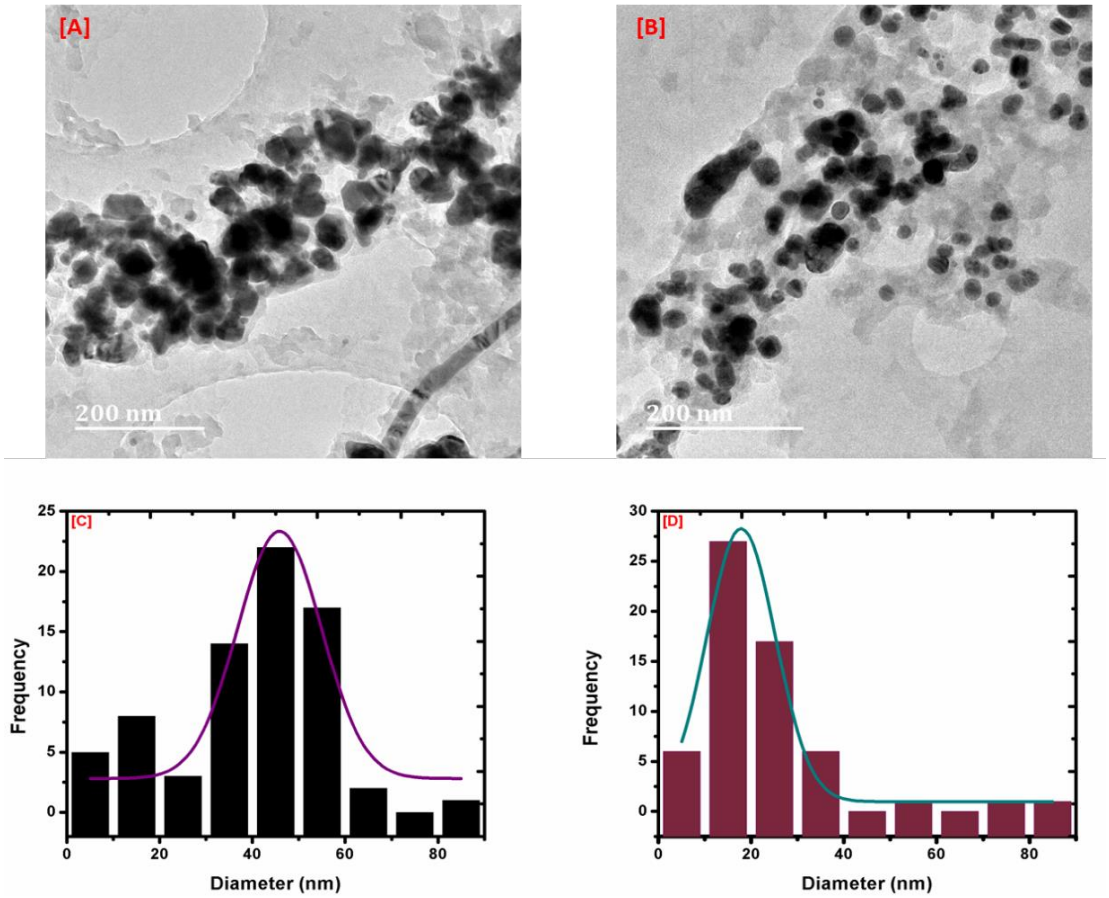

Figure 4.20: HR-TEM images of **(A)** TRPIDC-CH_3 AgNPs **(B)** AgNPs and Size distribution histogram prepared by image j software of **(C)** TRPIDC-CH_3 AgNPs **(D)** AgNPs.

4.2.2.3 FTIR studies

The FTIR (Figure 4.21) measurements were performed to identify the responsible functional groups: in the synthesis of TRPIDC-CH_3 AgNPs (yellow line), in comparison with uncapped AgNPs (grey line) the peak at 1209.52 cm^{-1} was assigned to the C-N stretching of aromatic amine but was absent if the AgNPs are capped with TRPIDC-CH_3 ligand. The absorption peaks centered at 3294.74 and 1630.71 cm^{-1} are present in TRPIDC-CH AgNPs but shifted. The widest peak at 3294.74 shifted to 3291.24 cm^{-1}, which is attributed to the stretching vibrations of the O-H group responsible for reducing the Ag^+ ions to atoms. Furthermore, the suppressed bands at 1630.71 shifted to 1636.30 cm^{-1} stretching vibrations of C=C (alkane groups), are responsible for stabilizing the TRPIDC-CH_3 AgNPs. The functional groups mentioned above are mainly derived from heterocyclic compounds and these are the water-soluble components of *pelargonium graveolens* leaf extract mentioned in section 4.2.1. TRPIDC-CH_3 AgNPs FTIR spectrum resembles the FTIR of the uncapped AgNPs.

Pandian *et al* also reported similar results when synthesizing uncapped AgNPs using *pelargonium graveolens* leaf extract (Pandian *et al.* 2013). Baraka *et al* reported similar results when synthesizing uncapped AgNPs using alfalfa leaf extract (Baraka *et al.* 2017).

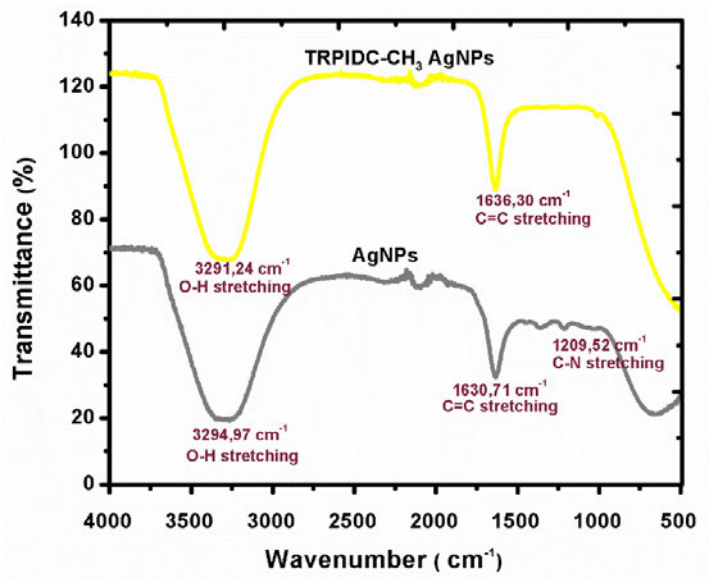

Figure 4.21: FTIR spectrum of TRPIDC-CH_3 AgNPs (**yellow**) and uncapped AgNPs (**grey**).

4.2.3 Cytotoxicity activity

The cytotoxicity effects of TRPIDC-CH_3 AgNPs and uncapped AgNPs against MCF-7, A549, and HEK923 cells were determined by the MTT assay. Investigating the cytotoxicity of these nanoparticles to a cancer cell line was necessary to examine how they have affected the viability and proliferation of the cells. The percentage cytotoxicity of the nanoparticle was investigated at concentrations of 100 µg/ml and 50 µg/ml. All experiments were conducted in triplicate and the average absorbance readings were calculated according to the negative solvent control (at 1 % DMSO) and results are shown in appendix K.

There was an overall low cytotoxic effect of the synthesized nanoparticles against the cells, the highest percentage activity of 38.0±0.04 % was observed with uncapped AgNPs (Appendix K: Table 17.2) against A549, and cell growth inhibition of 29.5±0.064 % was seen with TRPIDC-CH_3 against MCF-7. A dose-dependent increase in cytotoxic activity was observed for each of the nanoparticles, as the concentration increased from 50 µg/ml to 100 µg/ml. Low cytotoxic activity was

observed with all the screened nanoparticles against HEK293. No Morphological examination was performed for the AgNPs since its cytotoxicity effects percentage was low compared to the other two nanomaterials.

Comparable results have been reported by Yusefi *et al*. who synthesized the iron oxide nanoparticles using *Punica Granatum* fruit peel extract and assessed their anticancer activity against MCF-7, HepG2, and normal cell lines NHEM. The results showed that the synthesized samples were less toxic to normal cells (Yusefi et al. 2020). Chellapandian *et al*. synthesized gold nanoparticles using red seaweed *Gracilaria verrucosa* and evaluated the anticancer activity using MTT assay. Various concentrations of AuNPs (0, 8, 16, 32, 64, and 128 µg/ml) against HEK293T and A549 cells. The results demonstrated that they were no significant difference ($P<0.05$) in cell viability up to 64 µg/ml compared to the negative control. As concentrations increases (128 µg/ml), slight toxicity was observed. Comparable cell viability was observed for HEK293 cells after treatment with Au NPs (0- 100 µg/ml) (Chellapandian *et al.* 2019).

4.2.4 Protein interaction

We discuss the spectroscopic interaction study of the TRPIDC-CH_3 AgNPs with HSA protein in comparison with the uncapped AgNPs. Hence, we discuss UV-Vis, Fluorescence, FTIR studies and we look at the modes of binding involved in the complex formation.

4.2.4.1 UV-vis absorption studies

The interactions between HSA and AgNPs have been studied in order to improve the conformation evolution of HSA as well as the binding on the surface of AgNPs. Figure 4.22a shows the spectral shifts in HSA with the rising concentration of TRPIDC-CH_3 AgNPs. The absorbance spectra of HSA at 280 nm gradually increase with no shift of maxima. According to the previously reported work (Beg *et al.* 2017), the valuation of these spectra also showed an increase in absorbance spectra of HSA without any shift in band position, which suggested the occurrence of HSA adsorption on the surface of TRPIDC-CH_3 AgNPs similar results are reported for uncapped AgNPs (Figure 4.22b). Figure 4.22c shows the linear fits at 280 nm and can be seen that was an increase in the absorbance in comparison with uncapped AgNPs.

According to previous literature reports, variations in the absorption spectra HSA frequently result from ground-state complex formation and static quenching mechanism (Bardajee *et al.* 2016). The binding constant (K_b) was determined using equation (5). K_b was determined from the slope of the plot of $1/(A - A_0)$ versus $1/[Q]$. K_b for HSA-TRPIDC-CH_3 AgNPs complex was 1.11×10^7 M^{-1} and 7.430×10^6 M^{-1} for HSA-AgNPs complex. TRPIDC-CH_3 ligand does not alter the absorption interaction studies when used as a capping agent for AgNPs. The equilibrium established between HSA and TRPIDC-CH_3 AgNPs during the complex formation is distinct by the following chemical equation.

$$\text{HSA} + \text{TRPIDC-CH}_3\text{ AgNPs} \xleftrightarrow{K_b} \text{HSA}\ldots\ldots\text{TRPIDC-CH}_3\text{AgNPs} \qquad (12)$$

$$K_b = \frac{[\text{HSA}.....\text{TRPIDC}-\text{CH3 AgNPs}]}{[\text{HSA}]\ \text{x}\ [\text{TRPIDC}-\text{CH3 AgNPs}]} \qquad (13)$$

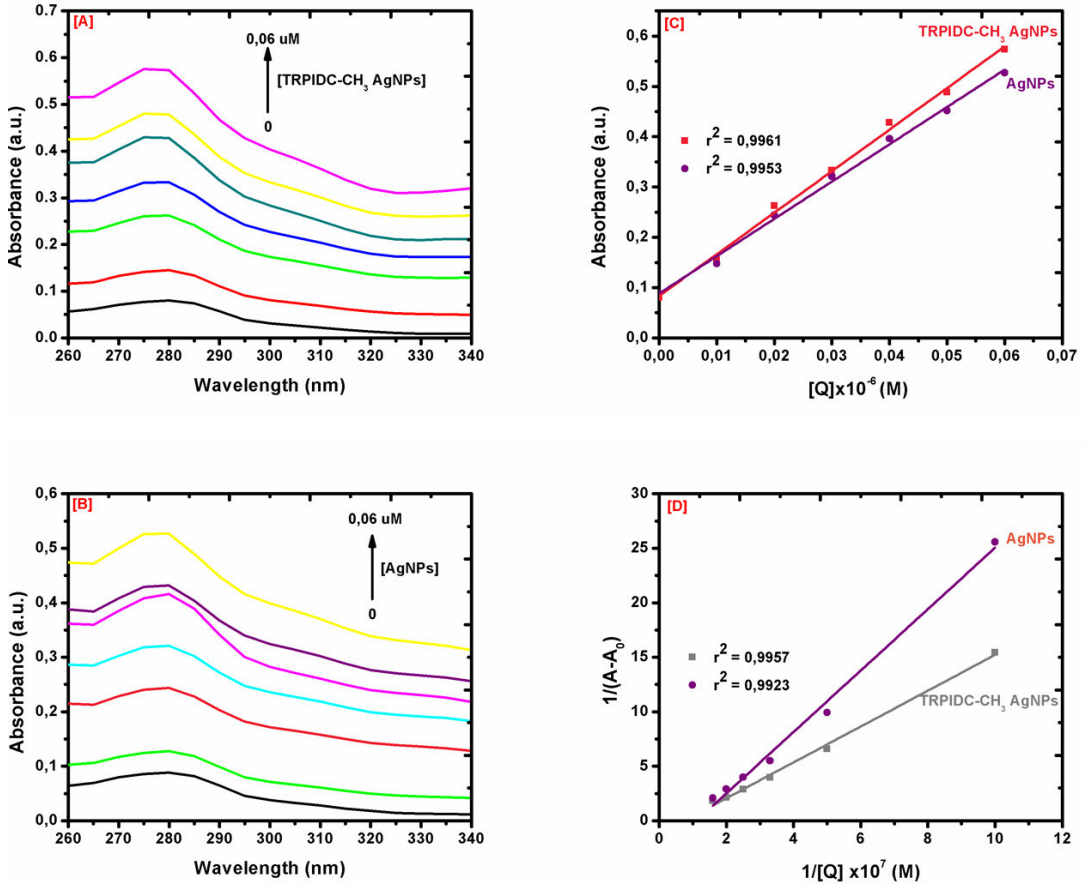

Figure 4.22: Absorbance spectra of HSA upon the addition of **(A)** TRPIDC-CH_3 AgNPs and **(B)** AgNPs **(C)** Linear fit for both the systems **(D)** Plot of $1/(A - A_0)$ versus $1/[Q]$ for both systems.

4.2.4.2 Fluorescence quenching study

The fluorescence spectrum of HSA is generally due to the single tryptophan residue that is positioned in a subdomain IIA ligand-binding site (Beg *et al.* 2017). The difference in the fluorescence intensity of HSA shows the adsorption of the tryptophan residue to the surfaces of the nanoparticles. Figure 4.23a reflects the fluorescence response of HSA with the addition of increasing concentrations of TRPIDC-CH_3 AgNPs (0 - 0,06 uM) by excitation at 280 nm at 310 K. Fluorescence intensity was quenched due to the inclusion of TRPIDC-CH_3 AgNPs without significant shifts in the emission wavelength for all three temperatures. The non-existence change in emission wavelength with a decline in intensity has demonstrated that the adsorption of proteins on the surfaces of nanoparticles. Resulted in a fluorescence quenching effect due to the development of HSA-TRPIDC-CH_3 AgNP complex after contact.

This quenching of protein fluorescence properties was studied by applying the Stern-Volmer (SV) equation (6). Figure 4.23c shows the Stern-Volmer plots of F_0/F vs [Q] at three different temperatures (298, 304, and 310K), and values of K_{SV} and K_q were estimated by slope with $\tau_0 \sim 10^{-8}$ s, the results are assembled in Table 4.6.The positive correlation of Stern–Volmer quenching constant and temperature showed that the likely quenching mechanism is dynamic quenching rather than static quenching. For the uncapped AgNPs and previously published work shows that the potential quenching mechanism is static quenching (Beg *et al.* 2017). The change in the quenching mechanism is due to the addition of the capping agent (TRPIDC-CH_3 ligand).

The binding constant (K_b) and the number of binding sites (*n*) for HSA complex interactions, were determined using the double-logarithm equation (7). K_a and *n* (Table 4.6) were calculated from intercept and slope of log $(F_0\text{-}F)/F$ versus log[Q] plot shown in Figure 4.23d. The binding constant and temperature showed a direct correlation indicating that the HSA-TRPIDC-CH_3 AgNPs complex is stable with the rise in temperature and the reverse effect was observed for the uncapped AgNPs. The values of *n* approximately equal to 1 indicated that TRPIDC-CH_3 AgNPs (and uncapped) binds to one class of site on HSA.

Table 4.6: The K_{SV}, K_q, K_b, and n of the HSA-TRPIDC-CH_3 AgNPs (and uncapped).

SeNPs	T (K)	K_{sv} (10^7 M^{-1})	K_q (10^{15} M^{-1} S^{-1})	r^2	K_b (M^{-1})	n	r^2
TRPIDC-CH_3	298	6,16	6,16	0,988	2,04x10^8	1,05	0,992
	304	7,82	7,82	0,99	2,49 x10^8	1,09	0,996
	310	10	10	0,992	15 x10^8	1,17	0,998
Uncapped	298	7,12	7,12	0,996	3,09 x10^8	1,09	0,988
	304	6,64	6,64	0,999	3,99 x10^7	0,97	0,991
	310	5,15	5,15	0,999	8 ,61 x10^5	0,75	0,998

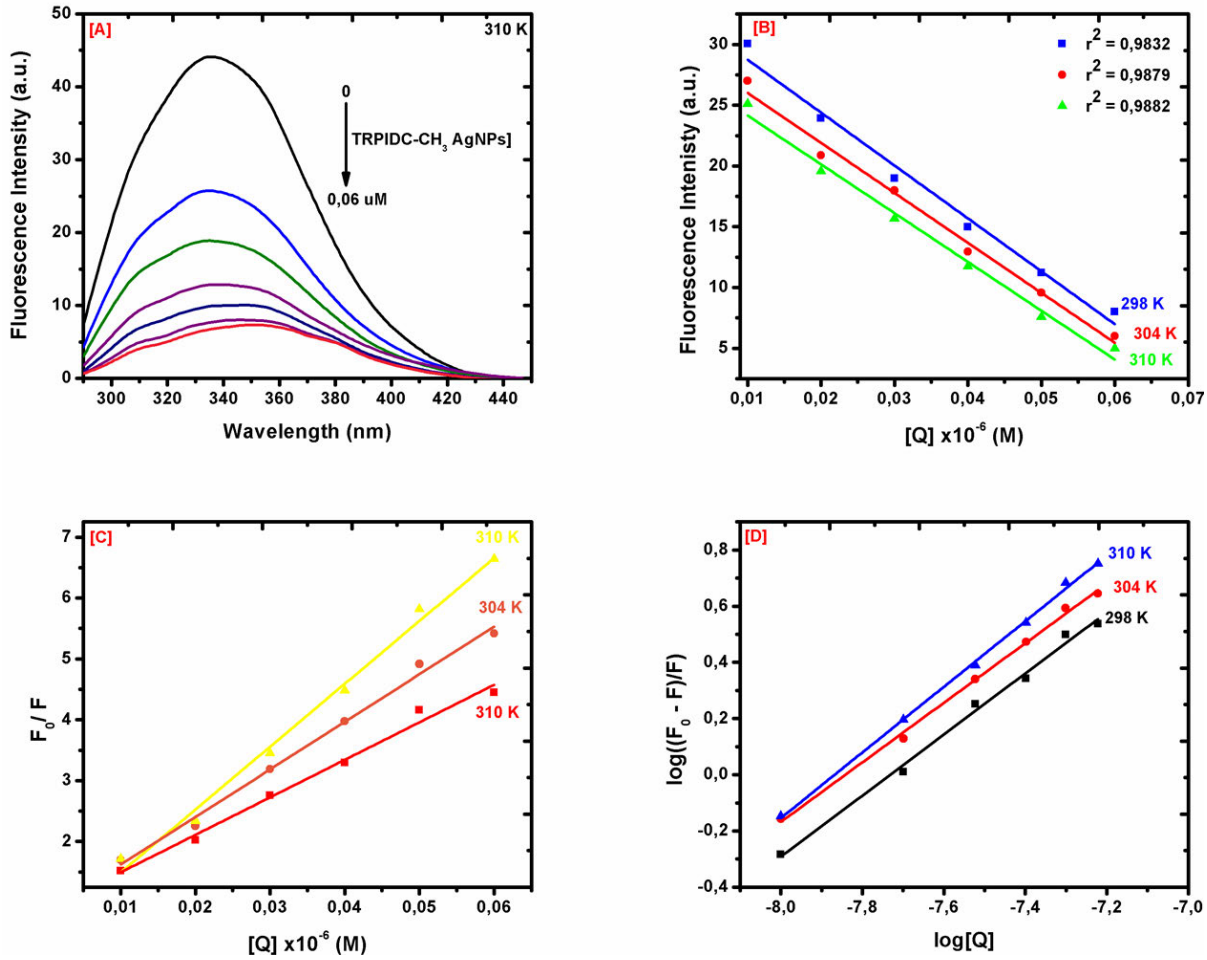

Figure 4.23: **(A)** Fluorescence spectrum of HSA in the presence of different concentrations of TRPIDC-CH_3 AgNPs. **(B)** a linear fit of the absorbances complex and increasing concentration of TRPIDC-CH_3 AgNPs at 345 nm at different temperatures. **(C)** Stern–Volmer curves for the binding of HSA with TRPIDC-CH_3 AgNPs at different temperatures. **(D)** log[(F_0 / F)/F] versus log[Q] plots for HSA versus TRPIDC-CH_3 AgNPs at different temperatures.

4.2.4.3 Mode of binding

The interaction forces between TRPIDC-CH_3 AgNPs and HSA are determined by thermodynamic parameters (ΔH, ΔS, and ΔG). These parameters were calculated form the Van't Hoff plot (Figure 4.24) by equation (8) and (9), they are illustrated in Table 4.7. The positive sign of ΔH and negative sign of ΔG indicates that the binding process is endothermic and spontaneous. The positive signs of ΔH and ΔS indicate the involvement of hydrophobic interactions HSA-TRPIDC-CH_3 AgNPs complex formation. For the uncapped AgNPs the binding process is exothermic and spontaneous and the interaction forces involve were either van der Waals or hydrogen bonding, similar results have been reported (Beg *et al.* 2017). The addition of the TRPIDC-CH_3 ligand changes the interaction forces involve in complex binding.

Table 4.7: Thermodynamics parameters of HSA and nanoparticles interaction.

Parameters	TRPIDC-CH_3 AgNPs	Uncapped AgNPs
$\Delta \boldsymbol{H}$ (kJ mol^{-1} K^{-1})	135,21	-382,79
$\Delta \boldsymbol{S}$ (kJ mol^{-1} K^{-1})	0,611	-1,12
$\Delta \boldsymbol{G}$(kJ mol^{-1} K^{-1})	-317,43	-48,24
Forces	hydrophobic interactions	hydrogen or van der Waals

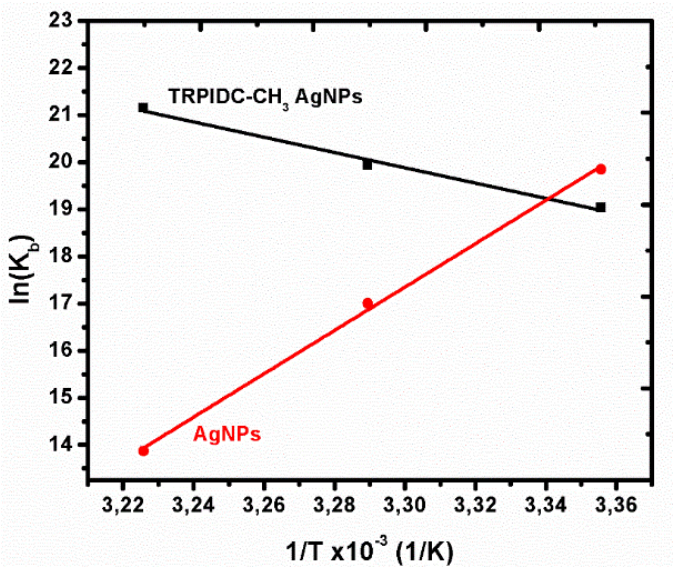

Figure 4.24: Van't Hoff plot of (**Black**) HSA-TRPIDC-CH_3 SeNPs and (**Red**) HSA-SeNPs.

4.2.4.4 FTIR studies

FTIR has emerged as an effective device for characterizing the relationship between protein-nanoparticles. The FTIR protein spectrum has many amide bands that reflect various vibrations of the peptide moiety and most of the studies have focused on the amide I band because it is responsive to changes in the protein secondary structure. (Rezanejade Bardajee *et al.* 2017). The amide I component bands are allocated according to the well-established assignment situation. The amide I peak occurs in the 1600-1700 cm^{-1} range (mainly the C=O stretch) is commonly used for the investigation of secondary protein structures. Figure 4.25 displays the effects of the study of the secondary protein structure of HSA before and after interaction with TRPIDC-CH_3 AgNPs. The peak at 1641.31 cm^{-1} shifted to 1636.30 cm^{-1} after addition TRPIDC-CH_3 AgNPs. This confirms the complex formation between HSA and TRPIDC-CH_3 AgNPs through hydrophobic interactions.

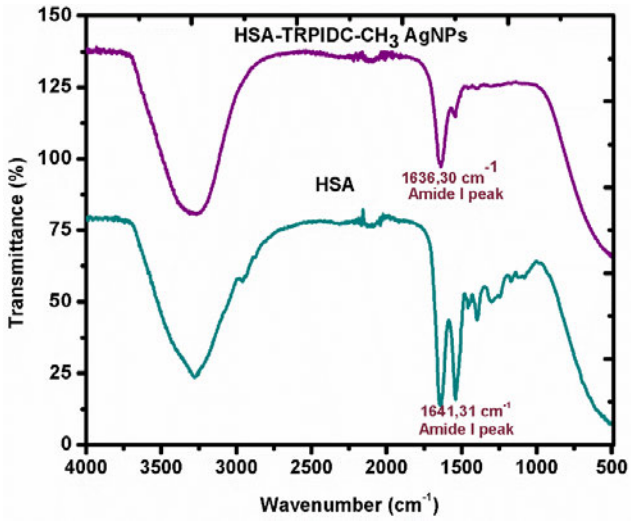

Figure 4.25: FTIR spectra of HSA before and after interactions with TRPIDC-CH_3 AgNPs.

4.2.5 Electrochemistry

4.2.5.1 Electrochemical characterization

We studied the electrochemical signals achieved from the different modified stages of the GCE. The Cyclic voltammograms of the GCE in different modified stages in 10 mL PBS (0.1 M, pH 7) containing 1 mM of $K_3[Fe(CN)_6]/K_4[Fe(CN)_6]$, recorded at a scan rate of 100 mV/s are illustrated in Figure 4.26a. The anodic peak current obtained from Bare GCE (curve i) was the lowest with I_a of 3.98 μA. There was a shift in peak

potential from 0.40 V to 0.23 V and GO:Hex/AgNPs/MWCNTs/GCE was the highest with I_a of 51.08 μA. There was an increase in anodic peak current with no shift in peak position (curve ii-vi) in comparison to bare GCE (curve i). After the nanoparticles were capped with TRPIDC-CH_3 ligand the peak current decreased slightly 29 % and 30 % for curve iv and vi when compared to uncapped AgNPs (curve iii and v), respectively. The ligand interfered with the surface area and electrical conductivity of the nanoparticles. Indicating that electrode modification with TRPIDC-CH_3 AgNPs ineffectively decreased the conductive activity of the electrode.

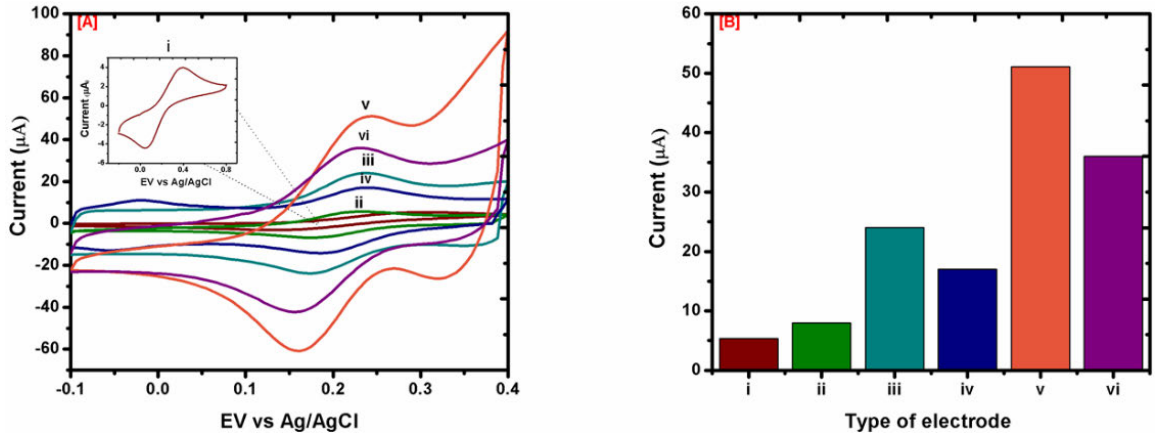

Figure 4.26: **(A)** Cyclic voltammograms of 0.02 mM ATP at (i) bare GCE, (ii) MWCNTs/GCE, (iii) SeNPS/MWCNTs/GCE, (iv) TRPIDC-CH_3 AgNPs/MWCNTs/GCE, (v) GO:Hex/AgNPs/MWCNTs/GCE. and (vi) GO:Hex/TRPIDC-CH_3 AgNPs/MWCNTs/GCE. **(B)** histogram displaying the current responses at corresponding electrodes.

4.2.5.2 Effect of pH

As the pH values of 0.1 M PBS containing 1 mM $K_4[Fe(CN)_6]/K_3[Fe(CN)_6]$ were increased from pH 5 to 9, the oxidized species of ATP becomes more stable as indicated by the increasing ratio of Ip_c/Ip_a shown in Figure 4.27 and Table 16.2 (Appendix J). When the Ep_a was plotted against pH values (Figure 4.27b and c), the Ep_a remain constant at 0.23 V for the GO:Hex/TRPIDC-CH_3 AgNPs/MWCNTs/GC electrode and for the GO:Hex/AgNPs/MWCNTs/GC electrode it increased from 0.23 to 0.24 V after pH 6 and it was constant throughout. Figure 4.27a and c showed the cyclic voltammograms of the GO:Hex/TRPIDC-CH_3AgNPs/MWCNTs/GC and GO:Hex/AgNPs/MWCNTs/GC electrodes, respectively. As the pH increased the anodic current decreased which was attributed to the deprotonation.

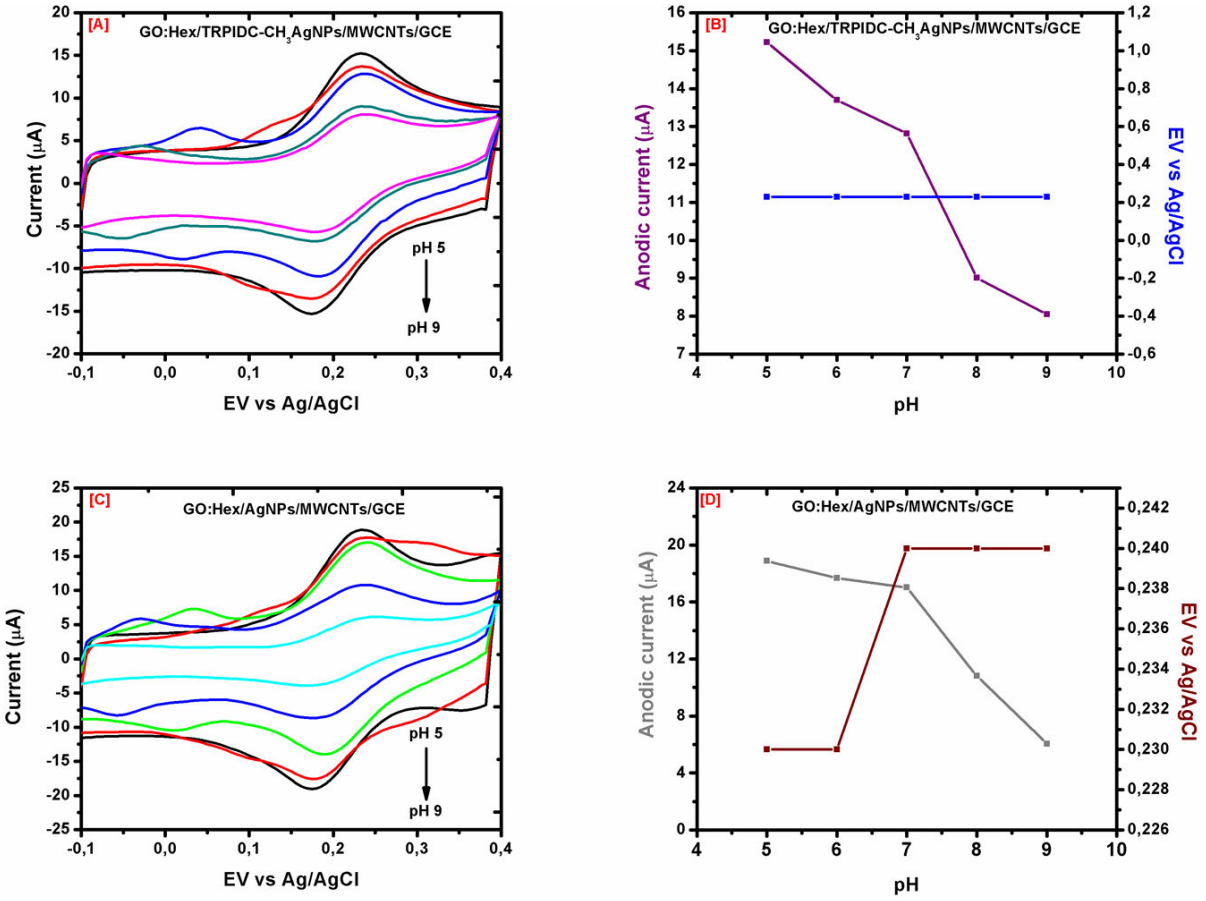

Figure 4.27: Effects of pH in 0.1 M PBS using **(A)** GO:Hex/TRPIDC-CH_3AgNPs/MWCNTs/GCE **(B)** corresponding plot of current vs pH, **(C)** GO:Hex /AgNPs/MWCNTs/GCE using 0.02 mM ATP and **(D)** corresponding plot of current vs pH Effect of Scan Rate.

4.2.5.3 Effect of Scan Rate

Figure 4.28a and c show the cyclic voltammograms of 0.02 mM ATP in the PBS of pH 7 containing 1 mM $K_4[Fe(CN)_6]/K_3[Fe(CN)_6]$ at different scan rates with a distinct anodic and cathodic waves produced at the electrodes surfaces. The anodic and cathodic peak currents were increased with increasing scan rate. The plot of anodic peak current vs scan rate (Figure4.28b and d) gives a linear plot. Pointing to a diffusion-controlled response and its electrochemical behavior is quasi-reversible in the PBS of pH 7. The relationship between the redox peak currents and the scan rates were correlated at 0.9906 and 0.9903 for and anodic and cathodic peaks, respectively for GO:Hex/TRPIDC-CH_3AgNPs/MWCNTs/GCE. For GO:Hex/AgNPs/MWCNTs/GCE was for anodic peak 0.9970 and 0.9975 for cathodic peak.

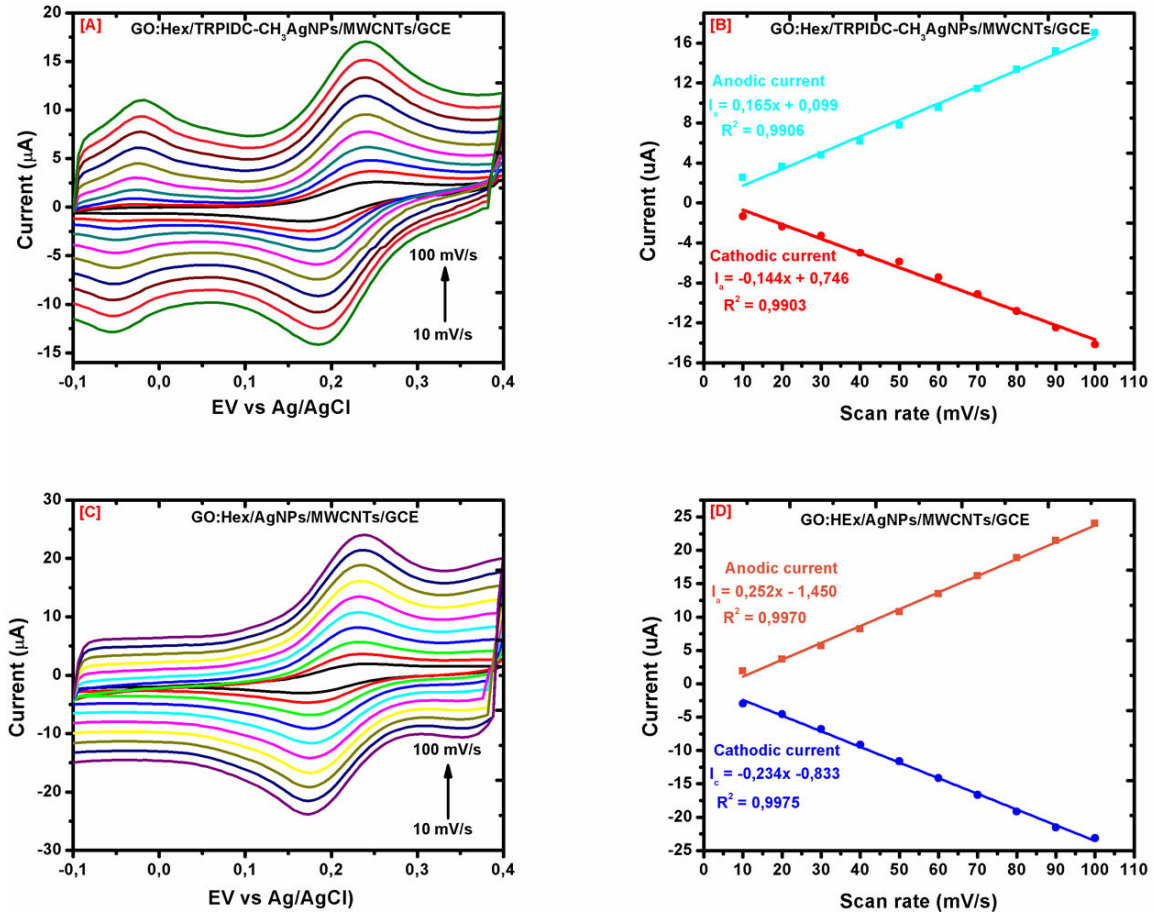

Figure 4.28: Effects of scan rate from 10 to 100 mV/s **(A)** GO:Hex/TRPIDC-CH_3AgNPs/MWCNTs/GCE **(B)** corresponding plot of current vs scan rate, **(C)** GO;Hex/AgNPs/MWCNTs/GCE using 0.02 mM ATP and **(D)** corresponding plot of current vs scan rate.

4.2.5.4 Effect of Deposition Time

Figure 4.29 showed the effects of deposition times for the GO:Hex/TRPIDC-CH_3AgNPs/MWCNTs/GC and GO:Hex/AgNPs/MWCNTs/GC electrodes, which was investigated on an anodic peak current of 5 mM ATP in 0.1 M PBS containing 1 mM $K_4[Fe(CN)_6]/K_3[Fe(CN)_6]$ at pH 7. Under the time interval of 30 to 150 s. There was no change in the on anodic current as we increase deposition time.

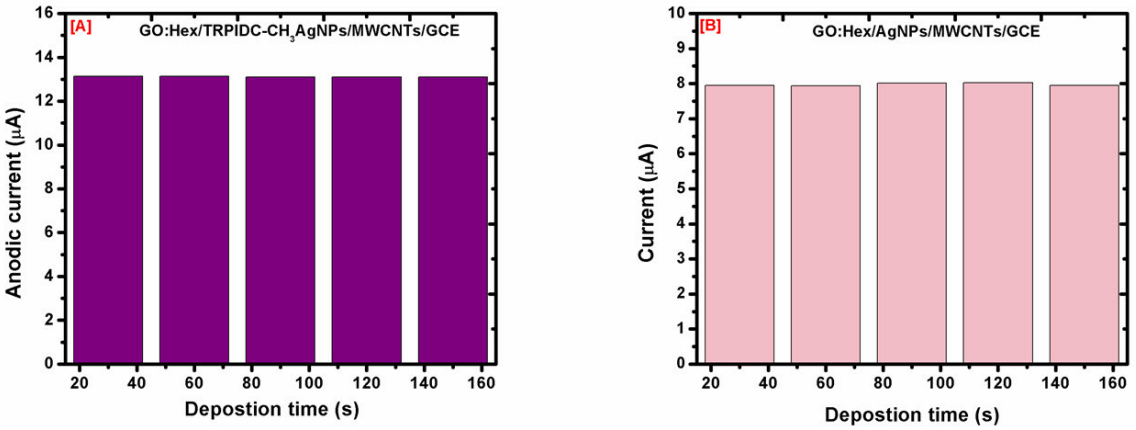

Figure 4.29: Effects of deposition time on the oxidation current from 30 to 150 s in 5 mM ATP **(A)** GO:Hex/TRPIDC-CH_3AgNPs/MWCNTs/GCE **(B)** GO:Hex/AgNPs/MWCNTs/GCE.

4.2.5.5 Indirect SWV technique for quantitative detection of ATP

Electrochemical detection of ATP via dual-enzyme biosensors requires indirect detection, raising the complexity of the detection system (Kueng *et al.* 2004). Based on the co-immobilization of the enzymes GOD and Hex on the electrode surface. The concentration of ATP in solution can be determined due to the competitive enzymatic reaction of the glucose substrate. Indirect electrochemical determination of ATP using the $[Fe(CN)_6]^{3-/4}$ peak as a reference peak, to observe the behavior of ATP with TRPIDC-CH_3 AgNPs (Capped) and the uncapped AgNPs. Figures 4.30a and 4.30c show the square wave voltammograms of $[Fe(CN)_6]^{3-/4-}$, in 10 mL PBS (0.1 M, pH 7) containing 1 mM of $K_3[Fe(CN)_6]/K_4[Fe(CN)_6]$ recorded at a scan rate of 100 mV/s, respectively using GO:Hex/TRPIDC-CH_3 AgNPs/MWCNTs/GCE and GO:Hex/TRPIDC-CH_3 AgNPs/MWCNTs/GCE. Where its peak current was monitored upon the addition of ATP (0.02. - 0.12 mM).

An increase in the peak current of $[Fe(CN)_6]^{3-/4-}$ as the concentration of ATP is increased from 0.02 – 0.12 mM was notedIf ATP is present in the solution, Hex converts ATP and glucose to reduce the local glucose concentration. The decreased glucose concentration is detected by GO and results in a current signal that is proportional to the ATP concentration, based on this observation the electrodes do detect the response of ATP. Figures 4.30b and 4.30d display the linear plot between the concentrations of ATP and the peak currents of $[Fe(CN)_6]^{3-/4-}$, with correlation coefficients of 0.9905 and a LOD of 0,03 mM and a LOQ of 0,08 mM for the GO:Hex/TRPIDC-CH_3AgNPs/MWCNTs/GC electrode. GO:Hex/AgNPs/MWCNTs/GC

electrode had a correlation coefficients of R^2 = 0.9944 and a LOD of 0,02 mM and a LOQ of 0,06 Mm, respectively.

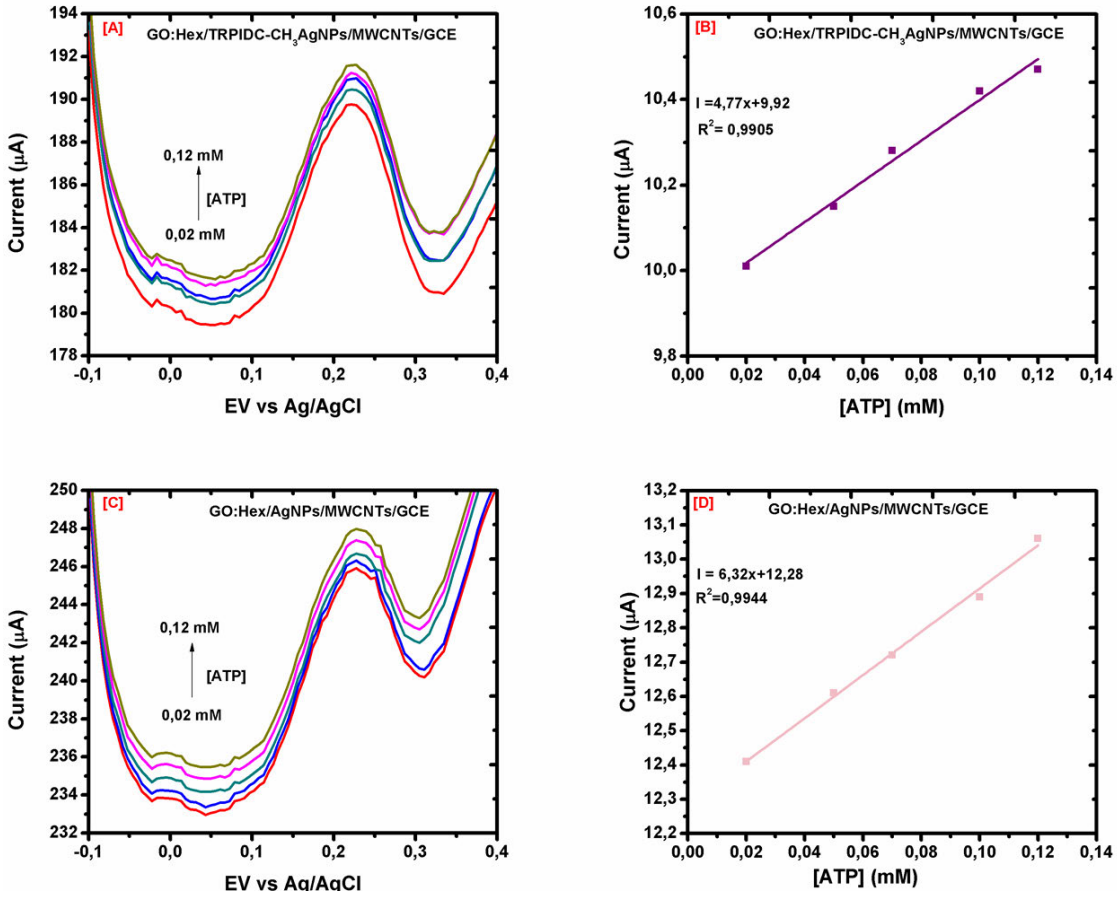

Figure 4.30: **(A)** SWV voltammogram GO:Hex/TRPIDC-CH_3 AgNPs/MWCNTs/GCE at different concentrations (0.02-0.12 mM), **(B)** Corresponding calibration curve showing linear dependence of the peak currents versus concentration of ATP, **(C)** SWV voltammogram GO:Hex/AgNPs/MWCNTs/GCE and **(D)** Corresponding calibration curve.

4.2.5.6 Reproducibility and Stability

The stability of the developed biosensors was tested using SWV (Figures 4.31a and 4.31c) and was observed by assessing the response of $[Fe(CN)_6]^{3-/4-}$ peak when ATP (0.02-0.26 mM) was introduced for 10 replicate measurements (n=10) over one day using the same coating. The $[Fe(CN)_6]^{3-/4}$ peak current was directly proportional to the ATP concentration and to some degree, began to decrease, signaling the saturation of the sensors. Figures 4.31a and 4.31b display the graphic representation for the GO:Hex/TRPIDC-CH_3 AgNPs/MWCNTs/GCE and GO:Hex/AgNPs/MWCNTs/GCE respectively. For both sensors, it is certain that they reach saturation at the same cycle

(6th) shown in insert a and insert b , TRPDIC-CH_3 ligand did not have an effect on the electrochemical stability of the AgNPs.

The reproducibility of the biosensors was confirmed by further testing of the $[Fe(CN)_6]^{3-/4}$ peak current by the addition of ATP (0.02-0.24 mM) using three prepared electrodes with the same coating. Figure 4.31c and d display the current influence on each concentration as seen in Figure 4.31d the line graphs are closer together relative to Figure 4.31c. RSD values of 1.87 for GO:Hex/AgNPs/MWCNTs/GCE sensor and 3.37 for GO:Hex/TRPIDC-CH_3 AgNPs/MWCNTs/GCE sensor and obtained for three replicate measurements for each sensor. The GO:Hex/AgNPs/MWCNTs/GCE sensor is more reliable because of the smaller the RSD.

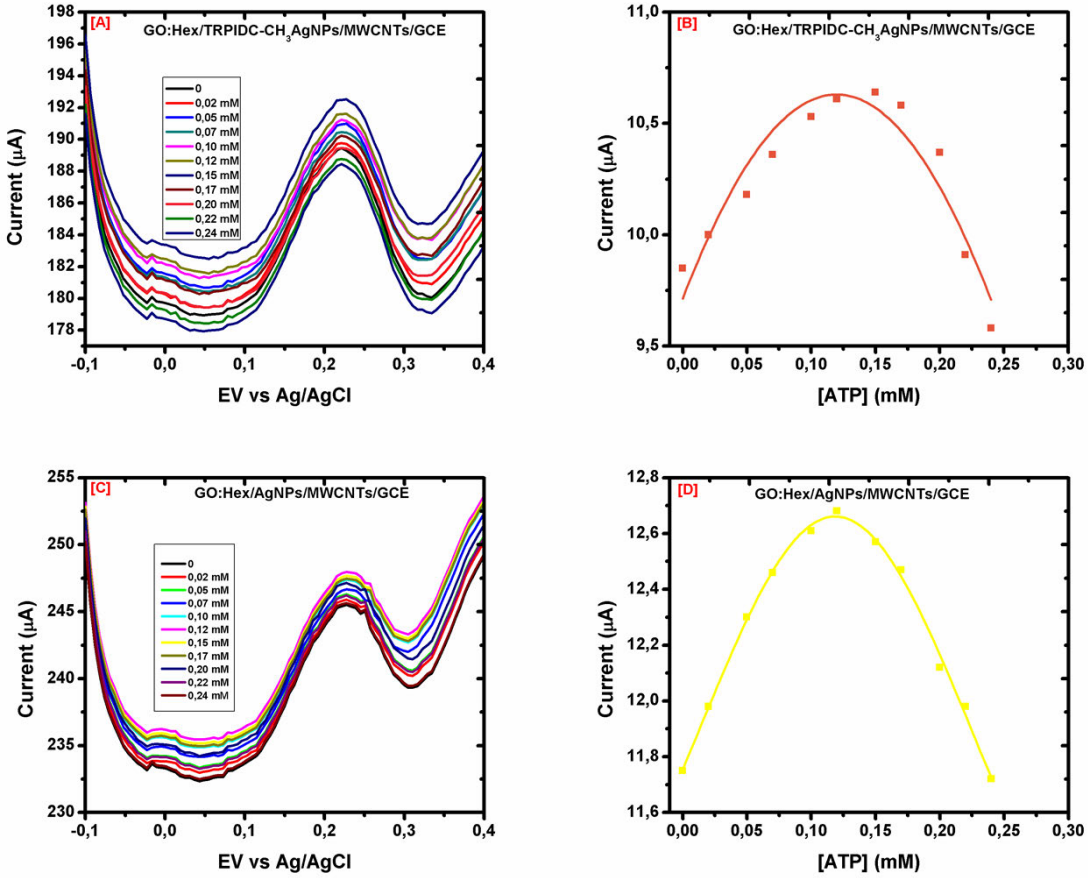

Figure 4.31: **(A)** Square wave voltammogram GO: Hex/ TRPIDC-CH_3AgNPs/MWCNTs/GCE at different concentrations of ATP (0 – 0.24 mM) and **(B)** Corresponding line graph of concentration vs current, showing the effect of current, **(C)** Square wave voltammogram GO:Hex/AgNPs/MWCNTs/GCE at different concentrations of ATP (0 – 0.24 mM) and **(D)** Corresponding line graph of concentration vs current, showing the effect of current.

4.2.5.7 Real Sample analysis

The efficiency of the developed biosensors was tested for ATP analysis in two commercially available samples, Swanson peak ATP and Vita-thion tablets. The samples were spiked with three different amounts (0.05, 0.07 and 0.10 mM) of ATP. The quantitative findings in Table 4.8 correspond to the mean voltammogram for the ATP triplicate analysis in tablets. GO:Hex/TRPIDC-CH3AgNPs/MWCNTs/GCE had a lower recovery rate relative to GO:Hex/AgNPs/MWCNTs/GCE.

Table 4.8: Results for the detection of ATP in spiked real samples analysed using the electrodes.

	GO:Hex/TRPIDC-CH_3AgNPs/MWCNTs/GCE				**GO:Hex/AgNPs/MWCNTs/GCE**			
Samples[a]	**[ATP] (mM)**	**Recovery (%)**	**RSD (%)**	**Relative Error[b]**	**[ATP] (mM)**	**Recovery (%)**	**RSD (%)**	**Relative Error[b]**
Swanson								
Spiked 1	0,07	82	4,01	-18,39	0,07	84	4,09	-15,57
Spiked 2	0,05	80	3,3	-20,49	0,05	86	0,77	-13,08
Spiked3	0,1	80	4,65	-19,96	0,1	88	5,16	-11,95
Vita-thion								
Spiked 1	0,07	80	3,05	-19,56	0,07	82	2,89	-18,19
Spiked 2	0,05	79	2,56	-20,89	0,05	83	2,89	-17,08
Spiked 3	0,1	81	0,58	-18,59	0,1	85	4,57	14,72

[a] Average of three measurements, [b] relative error = (absolute error/true value)*100

4.3 CASE STUDY 3: Cadmium Sulfide quantum dots

In this subsection, we discuss the camparision between the TRPIDC-CH_3 CdSQDs and the uncapped CdSQDs. We show its cytotoxicity assay using MCF–7, A549, and HEK293 cells, as well as its spectroscopic interaction with HSA protein. Lasty electrochemical behavior of ATP using a glassy carbon electrode (GCE) modified with TRPDC-CH_3 CdSQDs and uncoated CdSQDs separately, in conjunction with glucose oxidase (GOD) and hexokinase (Hex) enzymes.

4.3.1 Characterization of extract

4.3.1.1 Phytochemical screening

Nanoparticles are mainly affected by the natural phytochemicals existing in an extract (Ocsoy *et al.* 2018). A phytochemical screening test for the *Moringa oleifera* leaf extract, that was used to synthesise QDs, was performed to see which phytochemicals were present. *Moringa oleifera* leaves particularly reported to contain tannins, terpenoids, flavonoids, saponins, and alkaloids (Ilanko *et al.* 2019; Pratiwi *et al.* 2019) which may influence the reduction process and the stability of the synthesized QDs. The leaf extract tested positive for flavonoids, alkaloids, and terpenoids in agreement with the FTIR results (Figure 4.32), as well as with literature (Table 4.9).

Table 4.9: Characteristics of phytochemicals found in *Moringa oleifera* extract

Compound class	Phytochemical test	Literature	References
Flavonoids	+ +	+	(Preeti *et al.* 2018; Ilanko *et al.* 2019; Das *et al.* 2020; Suresh *et al.* 2020)
Alkaloids	+ +	+	(Preeti *et al.* 2018; Ilanko *et al.* 2019; Das *et al.* 2020; Suresh *et al.* 2020)
Terpenoids	+ +	+	(Preeti *et al.* 2018; Ilanko *et al.* 2019; Das *et al.* 2020)

++ positive current study; + literature

4.3.1.2 FTIR studies

The FTIR spectrum of *moringa oleifera* (Figure4.32) exhibits multiple absorption peaks indicating the various functional groups present in the *moringa oleifera* leaf extract, in the region of 400 to 4000 cm^{-1}. The peak around 3531.65 cm^{-1} is assigned to O-H stretching whilst 3069.64 cm^{-1} is attributed to the C-H stretching of alkenes.

The peak at 1884.31 cm^{-1} is assigned to the C-H bending of aromatic compounds. The peak at 1602.76 cm^{-1} C=C is attributed to the stretching of alkenes. The peak observed at 1185.29 cm^{-1} is due to C-N stretching. Based on the FTIR results the biomolecules of *moringa oleifera* leaf extract involved in the bioreduction of CdSQDs mainly contain the O-H, C=C, and C-H functional groups, which are in agreements with phytochemical screening. Das *et al* reported similar functional groups (C-H, C=C, C-N, and O-H) (Das et al. 2020). Jegadeensan *et a*l reported O-H and C=C functional groups (Jegadeesan *et al.* 2019).

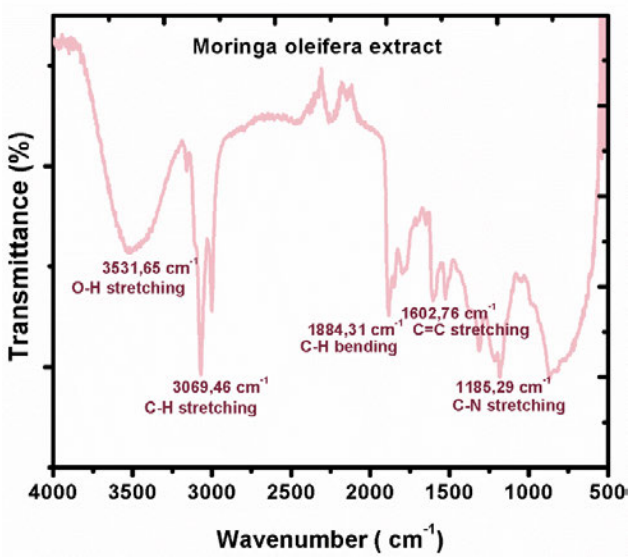

Figure 4.32: FTIR spectrum of *moringa oleifera* leaf extract.

4.3.2 Characterization of CdSQDs

The green approach was used to synthesize TRPIDC-CH_3CdSQDs from $CdSO_4$ using methanolic moringa oleifera leaf extract as an efficient reducing agent and TRPIDC-CH_3 ligand as a stabilizing agent. The dark green solution was incubated in the dark for 7 days and the solution changed to yellow suggesting the development of TRPIDC-CH_3 CdSQDs (Figure 4.33). In the synthesis of uncapped CdSQDs a similar method was used and the solution also switched from dark green to yellow colour. Shivaji *et al* reported a pale yellow solution using tea leaf extract (Shivaji *et al.* 2018). Kandasamy *et al* also produced yellow CdSQDs using fruit sap of *opuntia ficus-indica* (Kandasamy et al. 2019). Orange CdSQDs has also been reported using fungus (Borovaya *et al.* 2015)

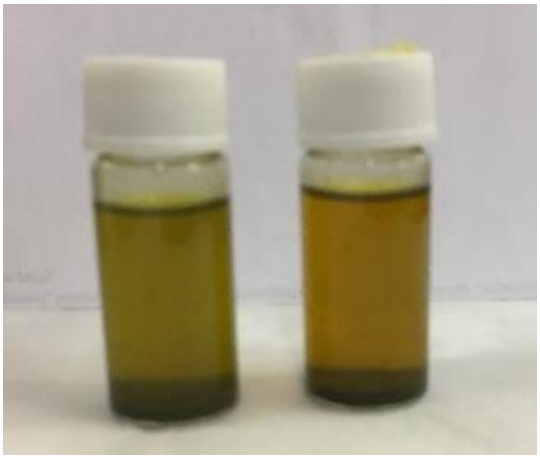

Figure 4.33: Green synthesized TRPIDC-CH_3 CdSQDs.

4.3.2.1 UV-Visible spectroscopy

UV-visible adsorption analysis was performed as semiconductor quantum dots are known to have a characteristic energy absorption edge shifted to the QD absorption band at a short wavelength. This 'blue' shift is induced by quantum size effects and symbolizes the nature of QD semiconductor and is created to demonstrate the presence of low-dimensional semiconductor properties (Kandasamy *et al.* 2019). Figure 4.34 displays the absorption spectra of the QDs. The absorption band is at 420 nm, which corresponds to a bandgap energy of 2.95 eV (calculated using the quantum mechanics energy equation) and the measured TRPIDC-CH_3 CdSQDs are within the well-known quantum-confined size range for CdSQDs reported by Shivaji *et a*l and Kandasamy *et a*l (Shivaji *et al.* 2018; Kandasamy *et al.* 2019).

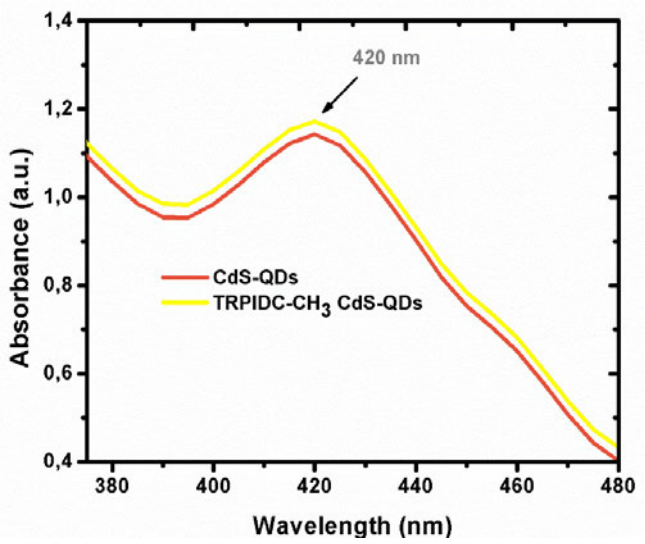

Figure 4.34: UV-Vis spectrum of TRPIDC-CH_3 CdSQDs (uncapped CdSQDs) synthesized.

4.3.2.2 Morphology and particle size analysis

HR-TEM image of TRPIDC-CH_3 CdSQDs shown in Figure 4.35a confirms the structure and size of the QDs. The TEM image shows the spherical shaped QDs and their average diameter is 4.5 nm, with a distribution of size of particles with a diameter between 3 and 9 nm (Figure 4.35b). Therefore, the outcome supports the formation of a quantum dot (<10 nm) (Kandasamy *et al.* 2019). Figure 4.35b shows the HR-TEM image of the uncapped CdSQDs, with an average diameter of 4 nm and a size distribution range of 3.5 to 5.5 nm (Figure 4.35d). The TRPIDC-CH_3 CdSQDs had a larger diameter by 5% and wider size distribution in comparison with uncapped CdSQDs. The addition of TRPIDC-CH_3 ligand increased the size of CdSQDs. The findings obtained are consistent with previous studies on the use of plant extracts to synthesize CdSQDs. Borovaya *et al* obtained CdSQDs that were spherical in shape and predominantly from 4 to 5 nm in size (Borovaya *et al.* 2015). Shivaji and co-works synthesized CdSQs using tea leaves and obtained a range between 2−5 nm in particle size (Shivaji *et al.* 2018)

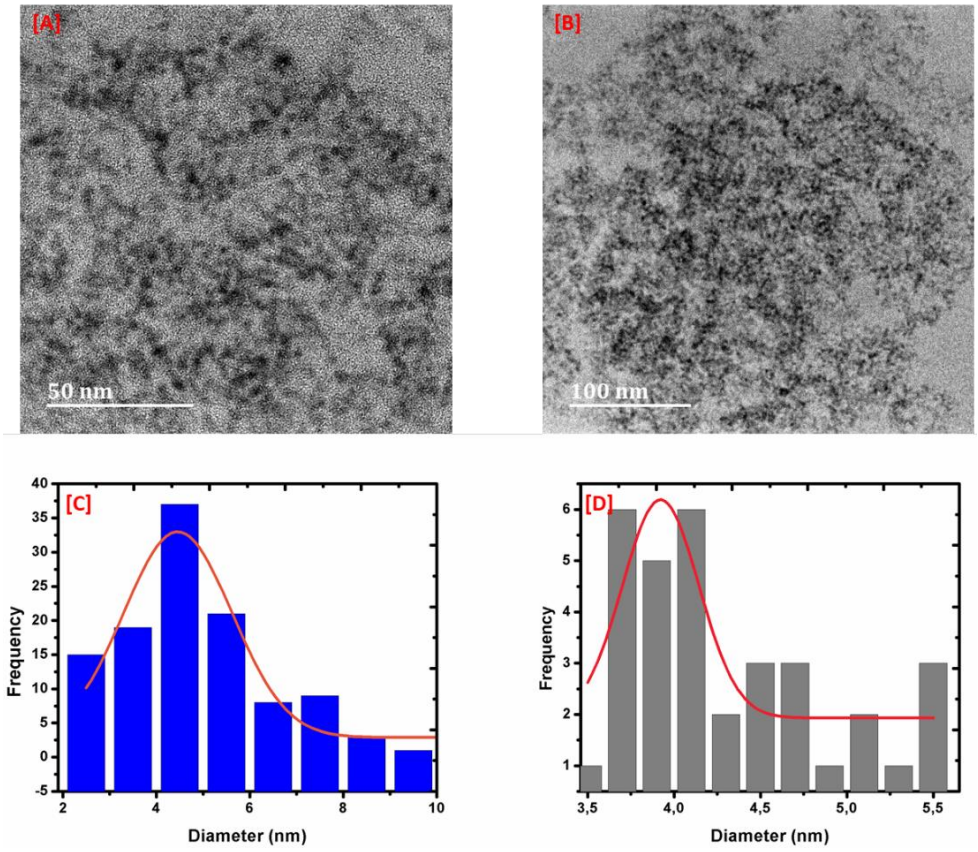

Figure 4.35: HR-TEM images of **(A)** TRPIDC-CH_3 CdSQDs **(B)** CdSQDs and Size distribution histogram prepared by image j software of **(C)** TRPIDC-CH_3 CdSQDs **(D)** CdSQDs.

4.3.2.3 FTIR studies

The FTIR spectrum (Figure 4.36) of TRPIDC-CH_3 CdSQDs (purple line) showed identical peaks with a minor shift and a disappearance in the absorption peak at 1787.26 cm^{-1} when the QDs were capped with the TRPIDC-CH_3 ligand in comparison to the uncapped CdSQDs FTIR spectrum with the TRPIDC-CH3 ligand (pink line). The weak peaks at 3065.74 and 3002.37 cm^{-1} shifted to 2931and 2860.73 cm^{-1} respectively, shows C-H group stretching. The peak at 1606.48 cm^{-1} shifted to 1636.30 cm^{-1} corresponds to the C=C stretching of the alkene group and a sharp peak at 1162.92 cm^{-1} shifted to 1010.11 cm^{-1} shows the C-O group stretching. Kandasamy et al and Shivaji *et al* reported similar results using fruit sap and tea leaves. (Shivaji *et al.* 2018; Kandasamy *et al.* 2019)

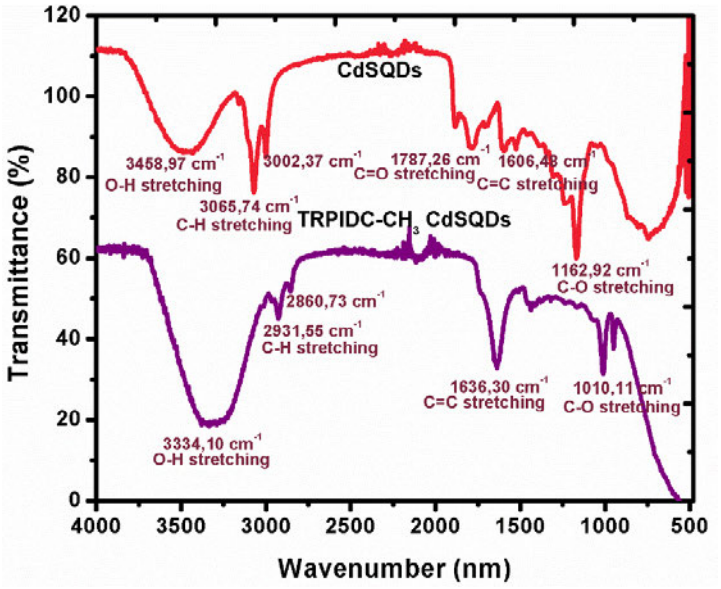

Figure 4.36: FTIR spectrum of TRPIDC-CH_3 CdSQDs (**purple**) and uncapped CdSQDs (**pink**).

4.3.3 Cytotoxicity activity

The cytotoxicity effects of TRPIDC-CH_3 CdSQDs and uncapped CdSQDs against MCF-7, A549, and HEK923 cells were determined by the MTT assay. Investigating the cytotoxicity of QDs to a cancer cell line was necessary to examine how they affected the viability and proliferation of the cells. 100 µg/ml and 50 µg/ml (concentrations) were used to investigate the percentage cytotoxicity of the QDs, as indicated in Appendix K (Tables 17.1, 17.2, and 17.3). All experiments were conducted in triplicate and the average absorbance readings were calculated

according to the negative solvent control (at 1 % DMSO). The results are displayed in Tables in appendix K.

There was an overall low cytotoxic effect of the synthesized nanoparticles against MCF-7, A549, and HEK293 cells, the highest percentage activity of 63.8±0.005 % was observed with uncapped CdSQDs at a 100 µg/ml Appendix K (Table 17.1) against MCF-7. Furthermore, cell growth inhibition of 43.7±0.15 % was seen with uncapped CdSQDs against A549. Although overall cytotoxicity was low, a dose-dependent increase in cytotoxic activity was observed for each of the nanoparticles, as the concentration increased from 50 µg/ml to 100 µg/ml. Low cytotoxic activity was observed with all the screened QDs against HEK293.

The microscopic analysis showed the morphological characteristics of untreated or treated cells. The control cells appeared in normal form and were bound to the surface. Nevertheless, the MCF-7 cells that were exposed to CdSQDs (Figure 4.37a) and lost their normal shape and cell adhesion ability, shrinking and decreasing in cell density. Similar changes have also been recognized in CdS-modified chitosan quantum dots in MCF-7 breast cancer cell line (Abdelhamid *et al.* 2019), indicating that the cytotoxic effect of synthesized AgNPs could be due to the antineoplastic properties and their ability to cause cell death by multiple molecular mechanisms (Farah *et a*l. 2016).

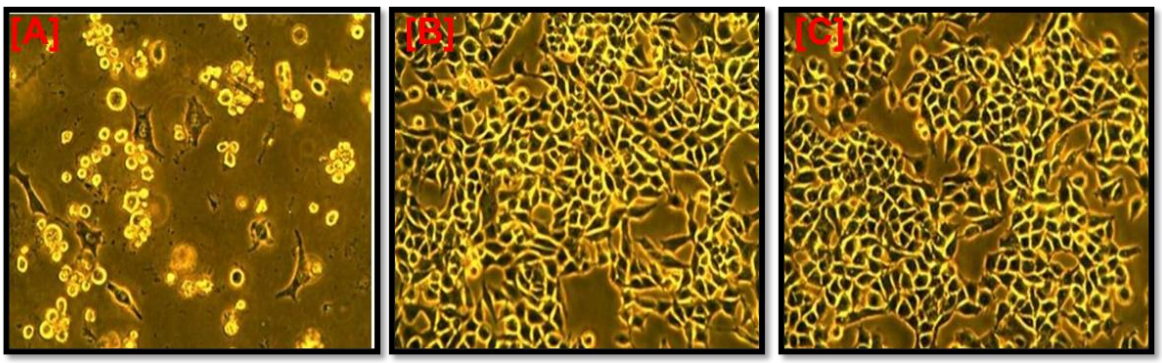

Figure 4.37: morphology of MCF-7 cell (100x magnification), treated with **(A)** Uncapped CdSQDs, **(B)** DMSO (1%), **(C)** untreated.

4.3.4 Protein interaction

We discuss the spectroscopic relationship of the TRPIDC-CH_3 CdSQDs with HSA protein by exploring UV-vis, fluorescence, FTIR studies and looking at the binding modes involved in complex forming.

4.3.4.1 UV-Vis absorption studies

UV-Vis absorption is a simple and relevant measurement to study the structural changes and to prove the complex formation. As shown in Figure 4.38a and b, there is a strong absorption band at around 278 nm which was primarily due to π→π * transition (Pansare *et al.* 2018). The absorbance of this peak is mainly due to the absorption of tryptophan (Ishtikhar et al. 2015; Mahanthappa et al. 2018), and it increases gradually, without any shift in the peak position, upon increasing the concentration of QDs. These observations indicate that there is a structural change (microenvironment) in HSA and the formation of a ground-state complex between HSA and QDs (Prasanth *et al.* 2017; Pansare *et al.* 2018).

Figure 4.38c shows the linear fits of increasing concentration of TRPIDC-CH_3CdQDs and uncapped CdSQDs at 278 nm which confirms the positive correlation between the concentration of QDs. Equations (14) and (15) were used to measure the degree of complex forming between HSA and TRPIDC-CH_3 CdSQDs (CdSQDs). According to the Benesi-Hildebrand relationship equation, the binding constant of complex formation was calculated from the shift in intensity of the absorption peak at 278 nm equation (5). From the plot slope of 1/(A - A0) versus 1/[Q] (Figure 4.38d), K_b was measured and the value was for the HSA-TRPIDC-CH_3 CdSQDs complex was $1.76x10^2$ M^{-1} and $1.20x10^3$ for HSA-CdSQDs Complex..

$$\text{HSA} + \text{TRPIDC-CH}_3\ \text{CdSQDs} \xleftrightarrow{K_b} \text{HSA……TRPIDC-CH}_3\ \text{CdSQ} \qquad (14)$$

$$K_b = \frac{[\text{HSA}.....\text{TRPIDC}-\text{CH3 CdSQDs}]}{[\text{HSA}]\ \text{x}\ [\text{TRPIDC}-\text{CH3 CdSQQs}]} \qquad (15)$$

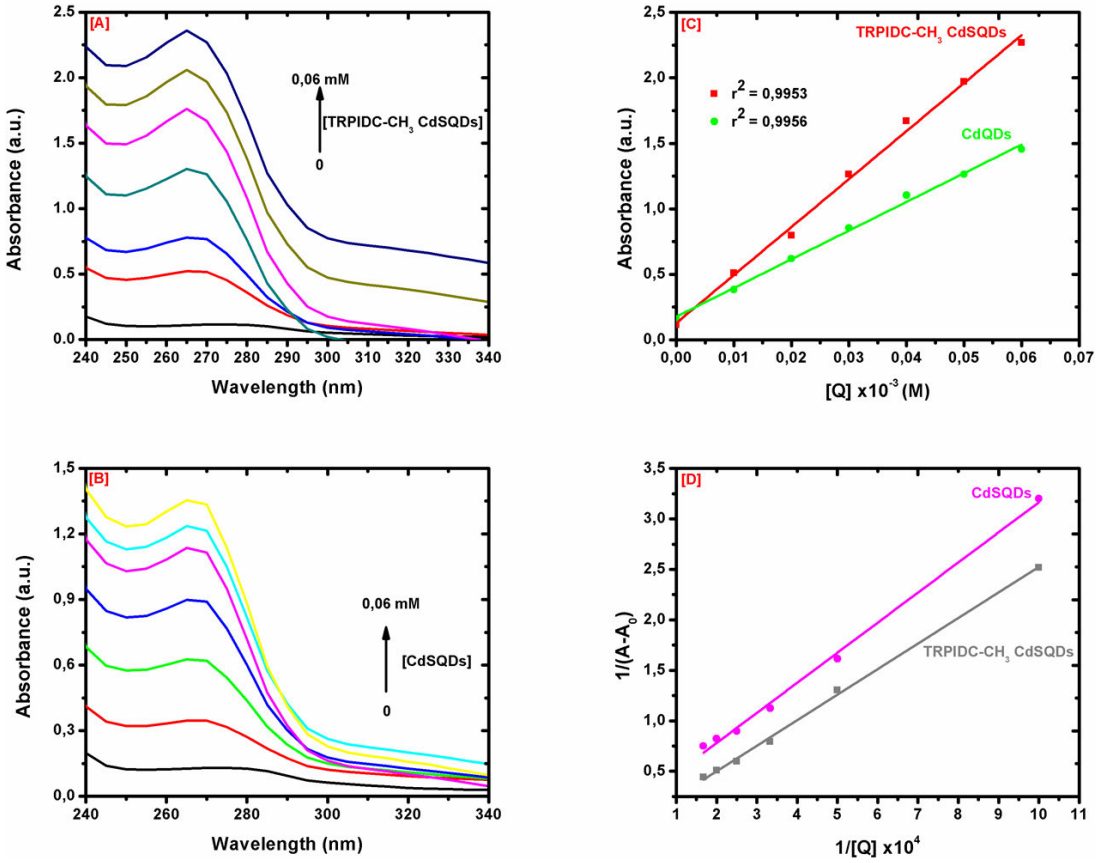

Figure 4.38: Absorbance spectra of HSA upon the addition of **(A)** TRPIDC-CH_3 CdSQDs and **(B)** CdQDs **(C)** Linear fit for both the systems **(D)** Plot of 1/(A - A_0) versus 1/[Q] for both systems.

4.3.4.2 Fluorescence quenching study

The HSA fluorescence emission spectra at the TRPIDC-CH_3 CdSQDs sequence of concentrations by setting the excitation wavelength at 280 nm are presented in Figure 4.39a. The fluorescence intensities of HSA decreased markedly with an increase in the concentration of TRPIDC-CH_3 CdSQDs and there were no peak changes or no new peaks (Figure 4.39b). These findings indicated that the TRPIDC-CH_3 CdSQDs and HSA complex could be responsible for the quenching process. A variety of molecular interactions, such as excited-state reactions, molecular rearrangements, energy transfer, ground-state complex formation, and collision quenching, can reduce the fluorescence intensity of a compound called fluorescence quenching (Rezanejade Bardajee *et al.* 2017).

Dynamic quenching refers to the process in which fluorophore and quencher come into contact during the life of the excited state, whereas static quenching refers to fluorophore-quencher complex formation. The fluorescence quenching process can

be quantitatively evaluated at various temperatures (298, 304, and 310 K) using the Stern–Volmer equation (6).Figure 4.39c displays the Stern-Volmer plots of F_0/F vs [Q] at three different temperatures (298, 304, and 310K) and the K_{SV} and K_q values were determined by slope with $\tau_0 \sim 10^{-8}$ s and shown in Table 4.10.

The fluorescence quenching mechanisms are usually classified as either dynamic quenching or static quenching and can be differentiated by their different dependence on temperature. The quenching constants decrease with the increase in temperature for static quenching, and the reverse effect is observed for dynamic quenching (Prasanth *et al.* 2017). The quenching constants values increase with the rise of temperature, which indicates that the quenching type of HSA-TRPIDC-CH_3 CdSQDs system. for HSA-CdSQDs system The quenching constants decrease with the temperature rise suggesting the static quenching as seen in Table 4.10.

Devi et al reported static quenching for the HSA-CdSQDs system (Devi et al. 2019). Rezanejade et *al* also reported static quenching for the HSA-CdSQDs and BSA systems (Rezanejade Bardajee *et al.* 2017). These observations suggest that capping the CdSQDs with TRPIDC-CH_3 ligand changes the quenching mechanism. The binding constant (K_b) and the number of binding sites between TRPIDC-CH_3 CdSQDs and HSA can be calculated according to the double logarithm equation. After measuring the fluorescence quenching intensities on HSA, the double logarithm algorithm was assessed by equation (7). Figure 4.39d showed the double-logarithm curve and Table 4.10 gives the corresponding calculated results. The number of binding sites (n) is approximately 1 for all temperatures. The n equal to 1 indicating that there is one class of binding site for TRPIDC-CH_3 CdSQDs and uncapped CdSQDs to HSA

Table 4.10: The K_{SV}, K_q, K_b, and n of the HSA-TRPIDC-CH_3 CdSQDs (& uncapped CdSQDs).

SeNPs	T (K)	K_{sv} (10^3 M^{-1})	K_q (10^{11} M^{-1} S^{-1})	r^2	K_b (M^{-1})	n	r^2
TRPIDC-CH_3	298	1,36	1,36	0,995	7,03x10^2	0,68	0,992
	304	1,76	7,82	0,992	2,83 x10^3	1,00	0,996
	310	3,05	3,05	0,998	5,02x10^3	1,12	0,995
Uncapped	298	4,22	4,22	0,995	4,91x10^3	1,00	0,994
	304	3,33	3,33	0,996	1,09 x10^3	0,89	0,999
	310	3,01	3,05	0,993	3.45 x10^2	0,75	0,996

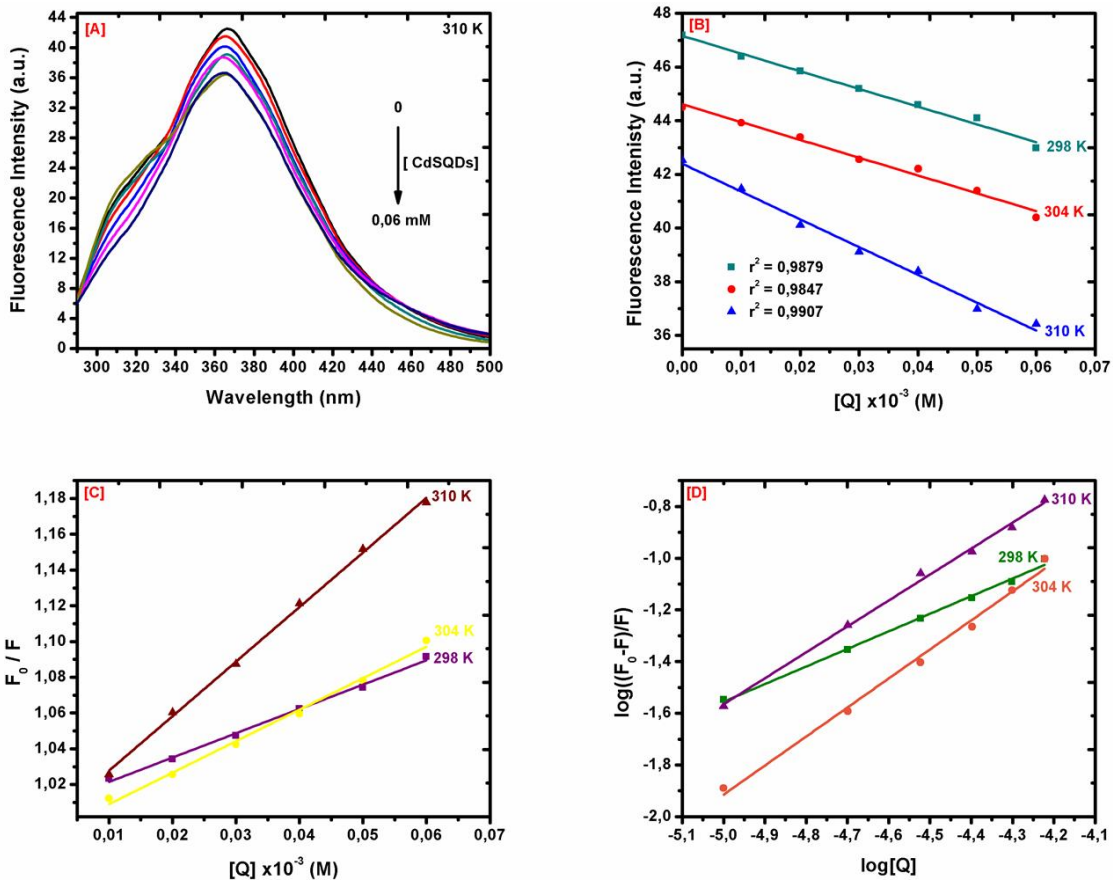

Figure 4.39: **(A)** Fluorescence spectrum of HSA in the presence of different concentrations of TRPIDC-CH_3 CdSQDs. **(B)** a linear fit of the absorbances complex and increasing concentration of TRPIDC-CH_3 CdSQDs at 345 nm at different temperatures. **(C)** Stern–Volmer curves for the binding of HSA with TRPIDC-CH_3 CdSQDs at different temperatures. **(D)** log[(F_0 / F)/F] versus log[Q] plots for HSA versus TRPIDC-CH_3 CdSQDs at different temperatures.

4.3.4.3 Mode of binding

The van't Hoff equation (8) was used to determine the driving force between TRPIDC-CH_3 CdSQDs and HSArom the van't Hoffplot: we calculated enthalpy and entropy changes between $\ln K_b$ and 1/T (Figure 4.40). The free energy change (ΔG) of the reaction was calculated using ΔH and ΔS in the equation (9). The binding parameters are listed in Table 4.11. The positive sign of ΔH and negative sign of ΔG indicates that the binding process is endothermic and spontaneous. The positive signs of ΔH and ΔS indicate the involvement of hydrophobic interactions HSA-TRPIDC-CH_3 CdSQDs complex formation. For the uncapped CdSQDs, the binding process is exothermic and spontaneous. The interaction forces involve were either van der Waals or hydrogen bonding. Chinnathambi *et al* reported similar results using uncapped CdSQDs (Chinnathambi *et al.* 2017).

Table 4.11: Thermodynamics parameters of HSA and quantum dots interaction.

Parameters	TRPIDC-CH_3 CdSQDs	Uncapped CdSQDs
$\Delta \boldsymbol{H}$ (kJ mol^{-1} K^{-1})	256,10	-170,89
$\Delta \boldsymbol{S}$ (kJ mol^{-1} K^{-1})	0,901	-0,501
$\Delta \boldsymbol{G}$(kJ mol^{-1} K^{-1})	-12,40	-20,79
Forces	hydrophobic interactions	hydrogen or van der Waals

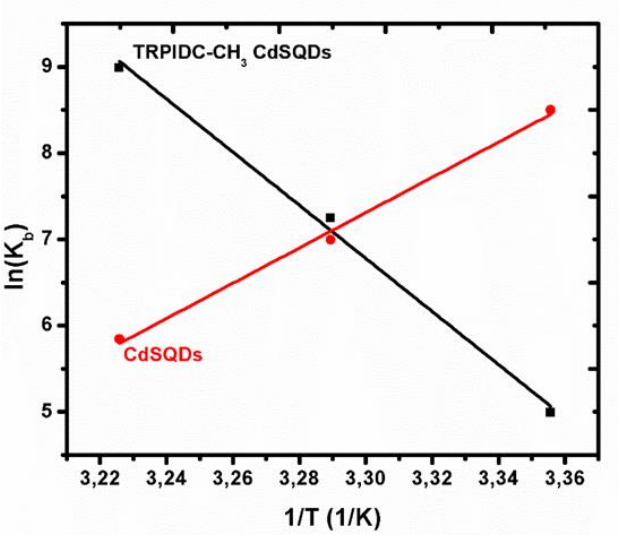

Figure 4.40: Van't Hoff plot of (**Black**) HSA-TRPIDC-CH_3 CdSQDs and (**Red**) HSA-CdSQDs.

4.3.4.4 FTIR studies

FTIR has appeared as an efficient technique for the characterization of protein-nanoparticles interaction. The FTIR spectrum of a protein exhibits several amide bands that represent different vibrations of the peptide moiety and most investigations have focused on the amide I band because it is sensitive to the change in the protein secondary structure (Rezanejade Bardajee *et al.* 2017). The component bands of amide I are distributed according to the well-established assignment condition. The amide I peak occurs in the 1600-1700 cm^{-1} region (mainly the C=O stretch) and is widely used for investigating the secondary structures of proteins. Figure 4.41 shows the results of the analyses on the secondary protein structure of HSA before and after interaction with TRPIDC-CH_3 CdSQDs. The peak at 1643.76 cm^{-1} shifted to 1636.30 cm^{-1} after addition TRPIDC-CH_3 CdSQDs. This confirms the complex formation between HSA and TRPIDC-CH_3 CdSQDs.

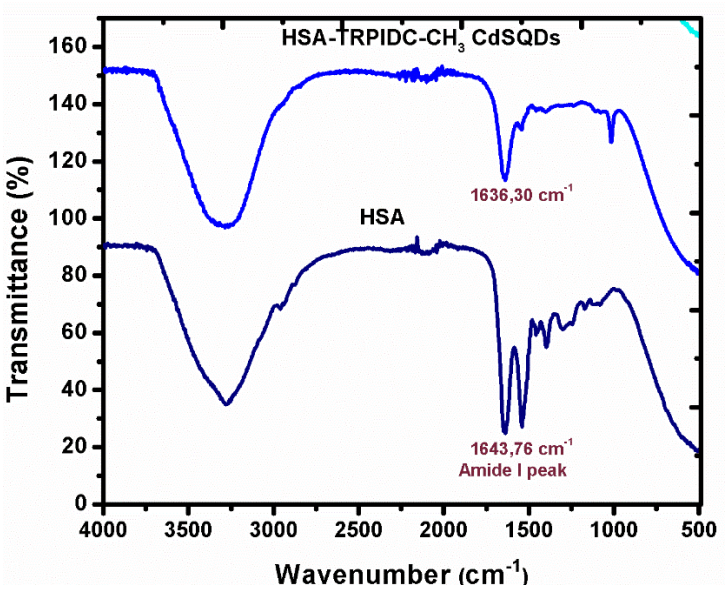

Figure 4.41: FTIR spectra of HSA before and after interactions with TRPIDC-CH_3 CdSQDs.

4.3.5 Electrochemistry

4.3.5.1 Electrochemical characterization

Figure 4.42a displays cyclic voltammograms of GCE at varying modified stages in a 10 mL PBS (0.1 M, pH 7) containing 1 mM of $K_3[Fe(CN)_6]/K_4[Fe(CN)_6]$, recorded at a scan rate of 100 mV/s. All the stages showed a well-defined reversible peak of $[Fe(CN)_6]^{3-/4-}$ with a bare GCE having the lowest (curve i) and curve vi (GO:Hex/TRPIDC-CH_3 CdSQDs/MWCNTs/GCE) the highest anodic peak current. At each stage, there was a change in peak potential from 0.40 V to 0.23 V. GO:Hex enzyme composite in curve vi and curve i improved [Fe(CN)6]3-/4− peak current (anodic) relative to the other stages where the enzyme composite was absent. When looking at curve iii and curve iv a rise in current was found with the QDs capped with TRPIDC-CH_3 (curve iv). Similar alterations were found with curve v and vi, suggesting that the TRPIDC-CH_3 ligand influenced the surface area and the conductive behavior of the sensor.

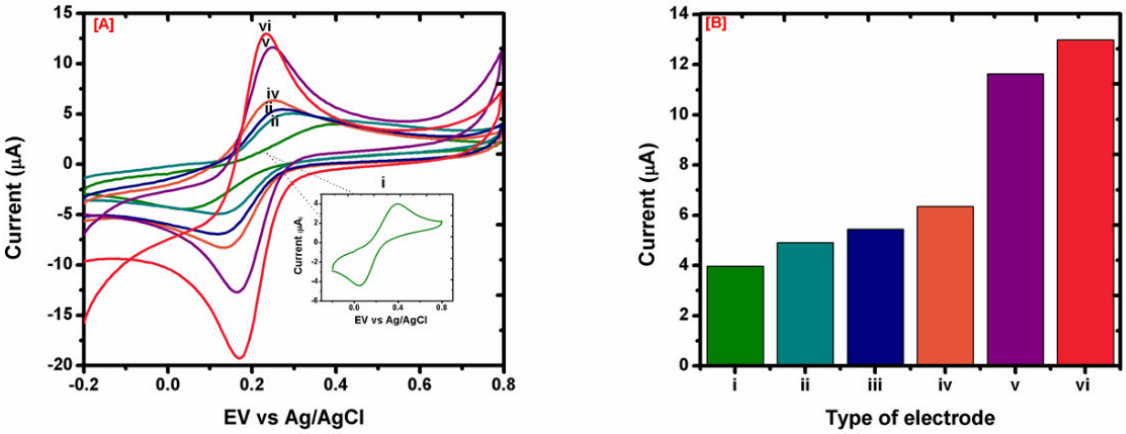

Figure 4.42: **(A)** Cyclic voltammograms of 1 mM $[Fe(CN)_6]^{3-/4-}$ in 10 mL PBS (0.1 M, pH 7) (i) bare GCE, (ii) MWCNTs/GCE, (iii) CdSQDs/MWCNTs/GCE, (iv) TRPIDC-CH_3 CdSQDs/MWCNTs/GCE, (v) GO:Hex/CdSQDs/MWCNTs/GCE,and (vi) GO:Hex/TRPIDC-CH_3 CdSQDs/MWCNTs/GCE. **(B)** histogram displaying the current responses at corresponding electrodes.

4.3.5.2 Effect of pH

The electrochemical behavior of electrodes were evaluated in different pHs' ranging from 5 to 9. CV measurement were conducted with ATP (0.02 mM) in 0.1 M PBS containing 1 mM $K_4[Fe(CN)_6]/K_3[Fe(CN)_6]$ under the scan rate of 100 mV/s. As the pH of supporting electrolytes increased, the oxidized species of ATP became more stable as indicated by the increasing ratio of Ip_c/Ip_a accumulated in Appendix J (Table16.3). For the GO:Hex/TRPIDC-CH_3 CdSQDs/MWCNTs/GCE as the pH increase, the anodic current decreased and the peak potential shifted towards the less positive values (Figure 4.43a and b). Figure 4.43c shows the pH voltammogram of GO:Hex/CdSQDs/MWCNTs/GC electrode there is a decrease in the anodic currents and shift in peak position to the more positive values in this pH range and after pH 7 the current becomes constant (Figure 4.43d).

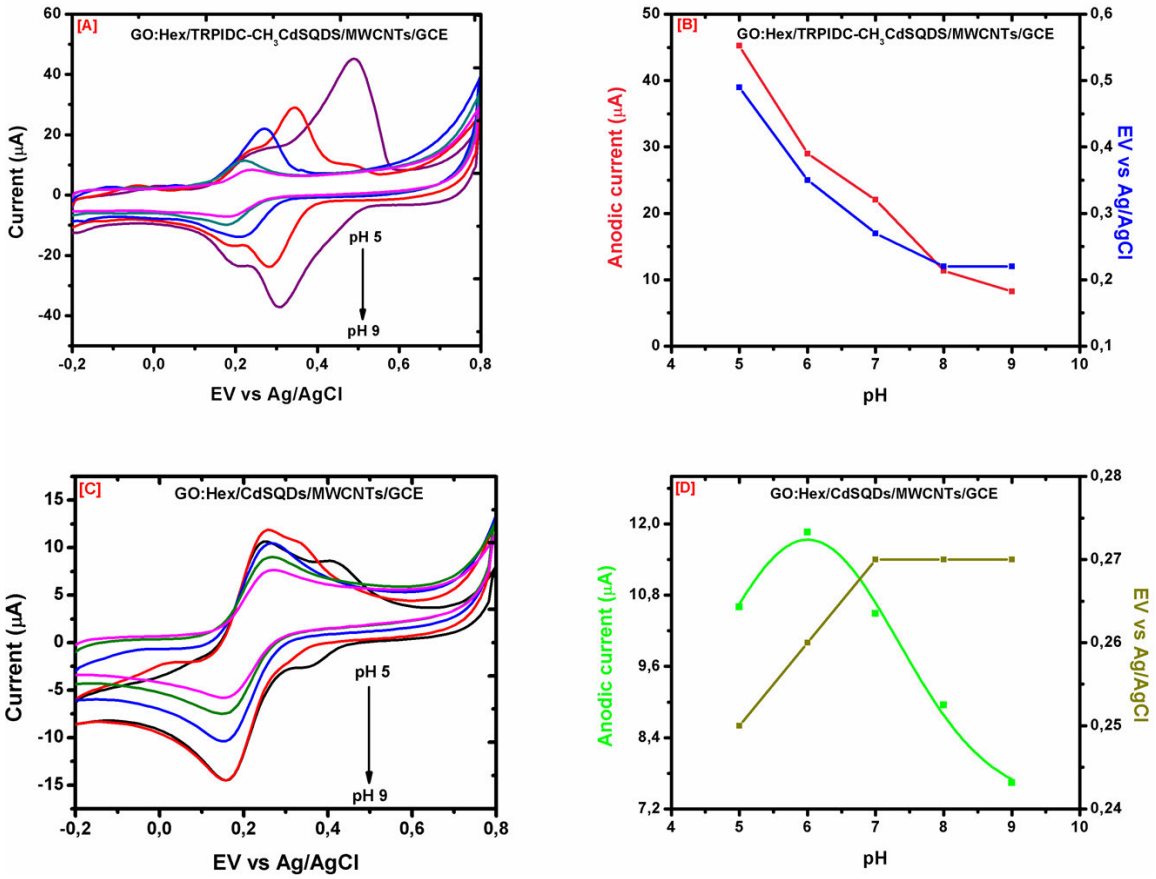

Figure 4.43: Effects of pH in 0.1 M PBS using **(A)** GO:Hex/TRPIDC-CH_3 CdSQDs/MWCNTs/GCE **(B)** corresponding plot of current vs pH, **(C)** GO:Hex /CdSQDs/MWCNTs/GCE using 0.02 mM ATP and **(D)** corresponding plot of current vs pH.

4.3.5.3 Effect of Scan Rate

The effect of scan rate on anodic and cathodic peak current of GO:Hex/TRPIDC-CH_3 CdSQDs/MWCNTs/GC and GO:Hex/CdSQDs/MWCNTs/GC electrodes upon addition of 0.02 mM ATP in 0.1 M PBS containing 1 mM $K_4[Fe(CN)_6]/K_3[Fe(CN)_6]$ at pH 7 was studied under the scan rate of 10–100 mV/s. In comparing the effect of scan rates on the cyclic voltammograms (Figure 4.44a and c), it is clear that both anodic and cathodic peaks were dominant throughout the scanning rate. The anodic and cathodic peak currents were increased with increasing scan rate. Good linearity was observed while plotting current against the scan rate (Figure 4.44b and d). The relationship between the redox peak currents and the scan rates were correlated at the anodic peak 0.9993 and cathodic peak 0.9982 for GO:Hex/TRPIDC-CH_3 CdSQDs/MWCNTs/GC electrode. For GO:Hex/CdSQDs/MWCNTs/GC electrode was for anodic peak 0.9867 and 0.9764 for cathodic peak.

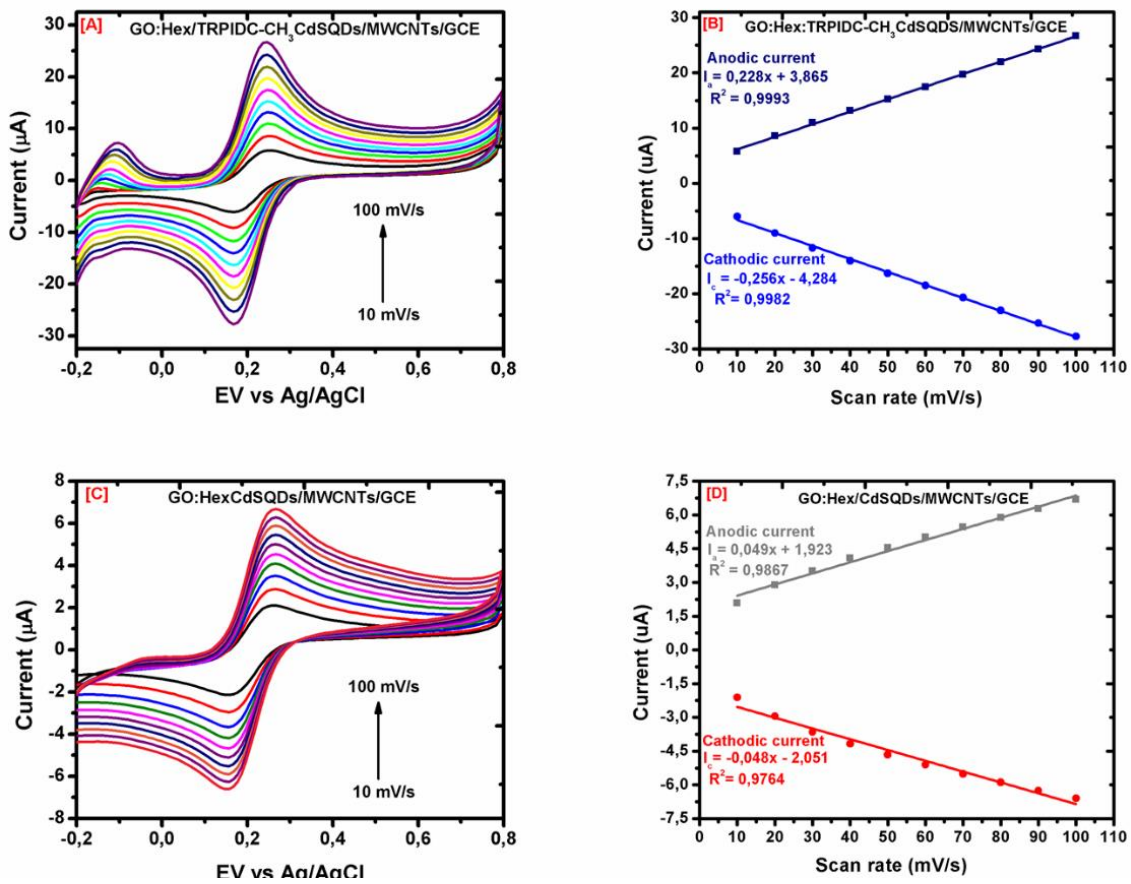

Figure 4.44: Effects of scan rate from 10 -100 mV/s **(A)** GO:Hex/TRPIDC-CH_3CdSQDs/MWCNTs/GCE **(B)** corresponding plot of current vs scan rate, **(C)** GO;Hex/CdSQDs/MWCNTs/GCE using 0.02 mM ATP and **(D)** corresponding plot of current vs scan rate.

4.3.5.4 Effect of Deposition Time

The effects of deposition times for the GO:Hex/TRPIDC-CH_3CdSQDs/MWCNTs/GCE and GO:Hex/CdSQDs/MWCNTs/GCE were investigated on an anodic peak current of 0.02 mM ATP in 0.1 M PBS containing 1 mM $K_4[Fe(CN)_6]/K_3[Fe(CN)_6]$ at pH 7, in the time interval of 30 - 150 s. The GO:Hex/TRPIDC-CH_3 CdSQDs/MWCNTs/GC electrode (Figure 4.45a) the current increased with the deposition time up to 60 s, beyond 60 s the anodic peak current decreases due to the saturation of the electrode surface with ATP. For the GO:Hex/CdSQDs/MWCNTs/GC electrode there was no uniformity of the current from 30 to 90 s, and after 90s saturation of electrode surface with ATP was observed as the current decreased. The addition of TRPIDC-CH_3 ligand caused an early saturation of the electrode surface.

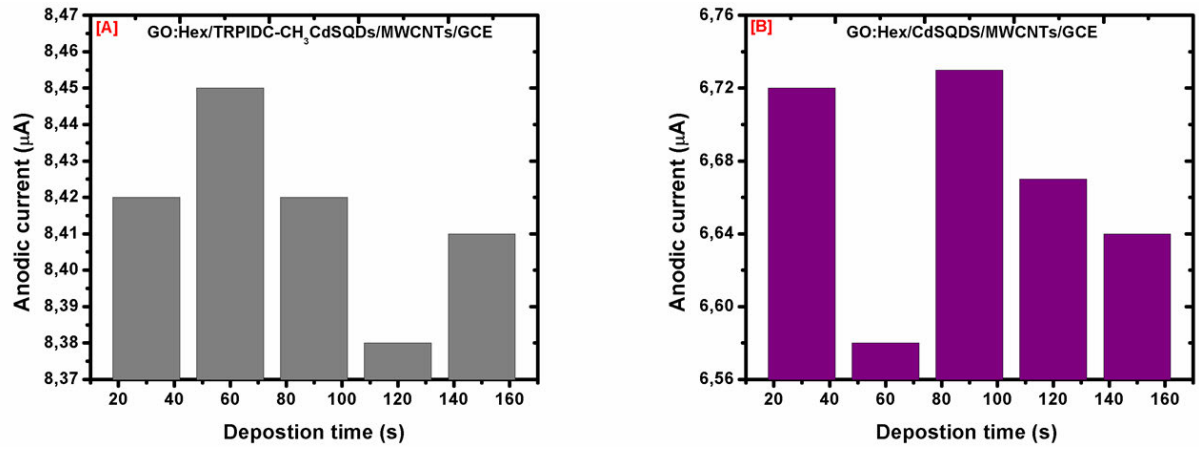

Figure 4.45: Effects of deposition time on the oxidation current from 30 to 150 s in 5 mM ATP **(A)** GO:Hex/TRPIDC-CH_3 CdSQDs/MWCNTs/GCE **(B)** GO:Hex/CdSQDs/MWCNTs/GCE.

4.3.5.5 Indirect SWV Technique Quantitative Detection of ATP

Indirect electrochemical determination of ATP using of redox probe ($[Fe(CN)_6]^{3-/4}$) as a reference peak, to observe the behavior of ATP with TRPIDC-CH_3 CdSQDs (Capped) and the uncapped CdSQDs was performed using a SWV in 10 mL PBS (0.1 M, pH 7) containing 1 mM of $K_3[Fe(CN)_6]/K_4[Fe(CN)_6]$ recorded at a scan rate of 100 mV/s respectively where its peak current was monitored upon the addition of ATP (0.2-0.15 mM). The SWV of the response of ATP on the GO:Hex/TRPIDC-CH_3 CdSQDs/MWCNTs/GC and GO:Hex/CdSQDs/MWCNTs/GC electrodes is displayed in Figure 4.46a and 4.46c respectively.

Upon the addition of ATP (0.02 – 0.15 mM), there was a decrease in the redox probe peak current, the electrochemical signal is produced by the oxidation of H_2O_2 at the electrode surface in the presence of ATP, the enzymatic reaction catalyzed by Hex is consuming glucose and the signal decreases (Kueng *et al.* 2004). Figures 4.46b and 4.46d display the linear plot between the concentrations of ATP and the peak currents of $[Fe(CN)_6]^{3-/4-}$, with correlation coefficients of 0.9789 and a LOD of 0,06 mM and a LOQ of 0,017 mM for the GO:Hex/TRPIDC-CH_3 CdSQDs/MWCNTs/GC electrode and GO:Hex/CdSQDs/MWCNTs/GC electrode had a correlation coefficient of 0.9808 and a LOD of 0,05 mM and a LOQ of 0,05 mM respectively.

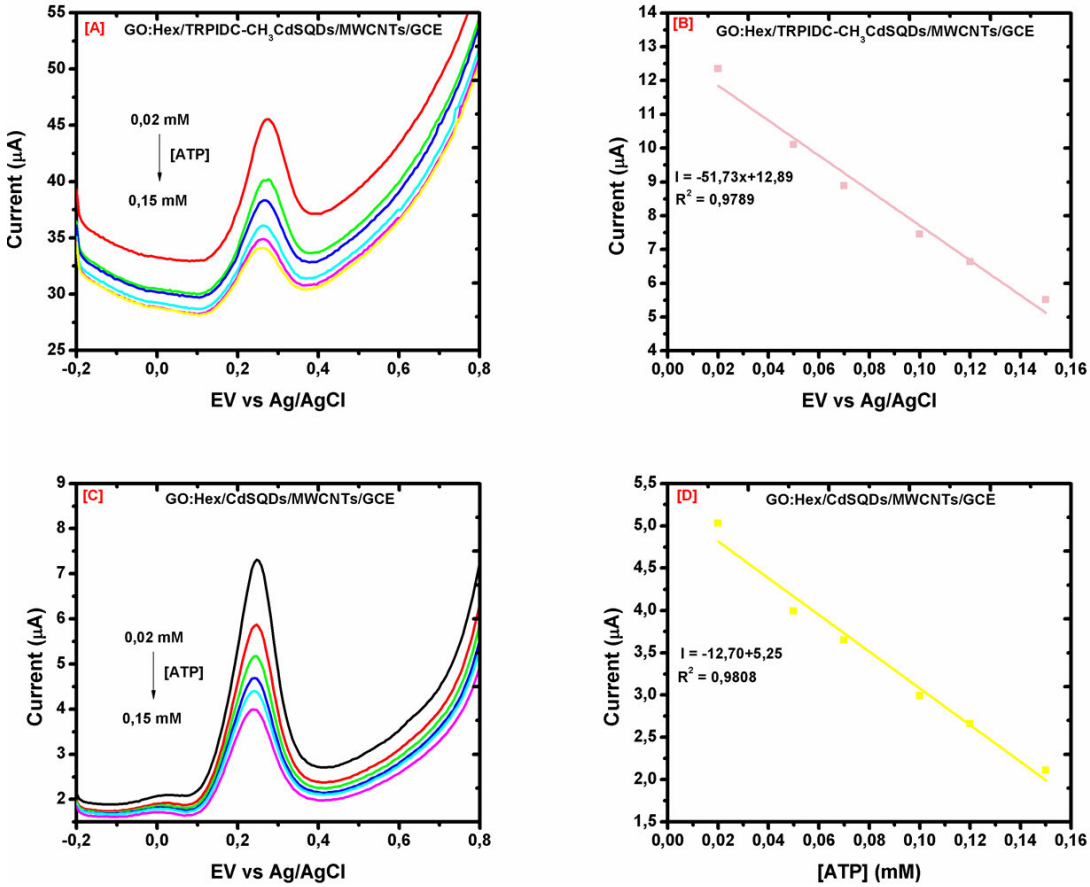

Figure 4.46: **(A)** SWV voltammogram GO:Hex/TRPIDC-CH_3 CdSQDs/MWCNTs/GCE at different concentrations (0.02–0.15 mM), **(B)** Corresponding calibration curve showing linear dependence of the peak currents versus concentration of ATP, **(C)** SWV voltammogram GO:Hex/CdSQDs/MWCNTs/GCE and **(D)** Corresponding calibration curve.

4.3.5.6 Reproducibility and Stability

The stability of the formed biosensors was tested using SWV (Figures 4.47a and 4.47b) and measured ATP response for 10 replication measurements (n=10) over one day using the same coating. The $[Fe(CN)_6]^{3-/4-}$ peak current was indirectly proportional to the ATP concentration. The redox probe current peak decreased to some degree and reached a saturation point where the sensors were unable to detect the addition of ATP, the peak current remained stable (Figure 4.47). The sensor with the uncapped QDs (insert b) achieved saturation faster than the sensor with the capped QDs (insert a).The TRPDIC-CH_3 ligand had an impact. The reproducibility of the biosensors was confirmed by further testing of the $[Fe(CN)_6]^{3-/4}$ peak current by the addition of ATP (0.02-0.24 mM) using three prepared electrodes with the same coating. Figure 4.47c and d display the current influence on each concentration. The %RSD for 6 successive

detections is about 2.63%, for the sensor with TRPIDC-CH_3 CdSQDs and 2.90% with the uncapped CdSQDs. indicating acceptable fabrication reproducibility.

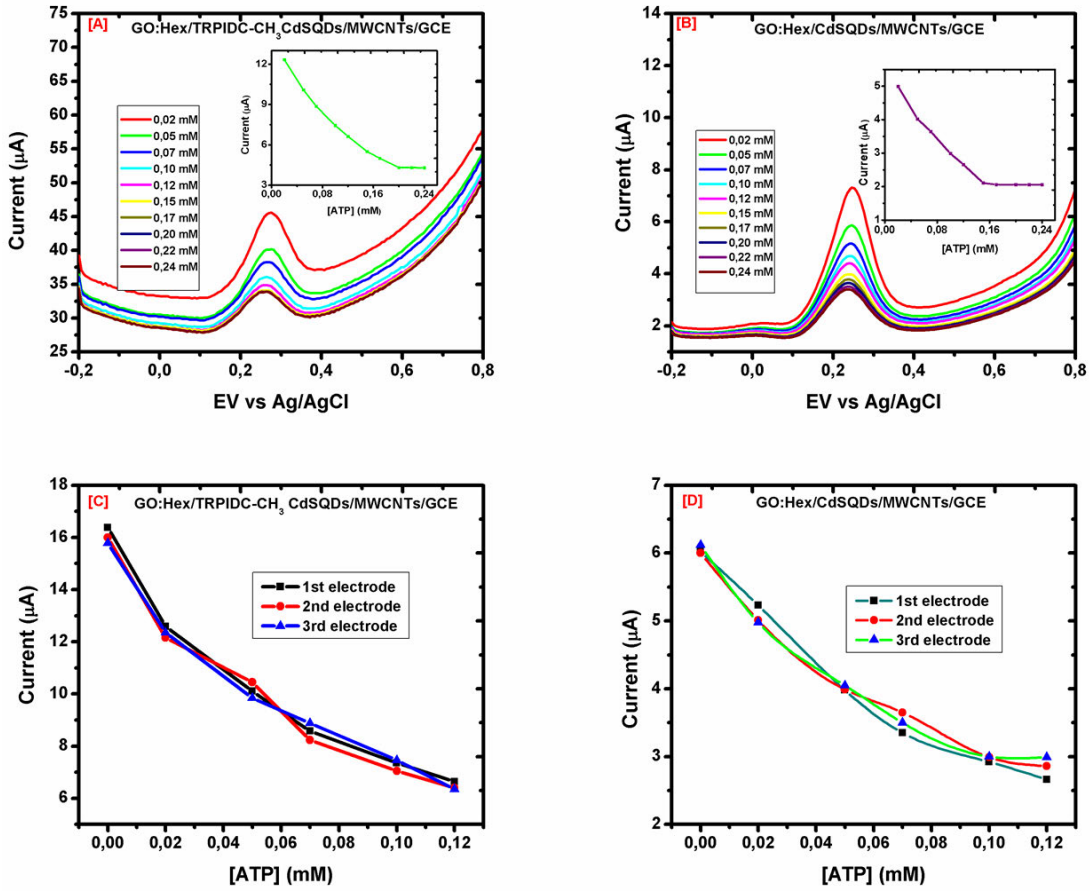

Figure 4.47: **(A)** Square wave voltammogram GO: Hex/ TRPIDC-CH_3CdSQDs/MWCNTs/GCE at different concentrations of ATP (0 – 0.24 mM) and **(B)** Corresponding line graph of concentration vs current, showing the effect of current, **(C)** Square wave voltammogram GO:Hex/CdSQDs/MWCNTs/GCE at different concentrations of ATP (0 – 0.24 mM) and **(D)** Corresponding line graph of concentration vs current, showing the effect of current.

4.3.5.7 Real Samples analysis

The optimized sensitive SWV procedure was successfully applied for the determination ATP in two commercially available tablet samples, Swanson peak ATP, and Vita-thion tablets. The samples were spiked with three different concentrations (0.05, 0.07, and 0.10 mM) of the standard solution of ATP. The results are shown in Table 4.12 for a response of ATP on the GO:Hex/TRPIDC-CH_3CdSQDs/MWCNTs/GC and GO:Hex/CdSQDs/MWCNTs/GC electrodes. Base on the obtained results CdSQDs had a time detecting ATP in these this may be due to interferences in the

sample. The GO:Hex/CdSQDs/MWCNTs/GC electrode had a lower percentage recovery compared to the GO:Hex/TRPIDC-CH_3CdSQDs/MWCNTs/GCE.

Table 4.12: Results for the detection of ATP in spiked real samples analysed.

Samples[a]	GO:Hex/TRPIDC-CH3CdSQDs/MWCNTs/GCE [ATP] (mM)	Recovery (%)	RSD (%)	Relative Error[b]	GO:Hex/CdSQDs/MWCNTs/GCE (ATP) (mM)	Recovery (%)	RSD (%)	Relative Error[b]
Swanson								
Spiked 1	0,07	80	2,33	-20,41	0,07	72	0,77	-28,3
Spiked2	0,05	76	2,49	-23,78	0,05	78	3,38	-21,79
Spiked3	0,1	81	1,56	-19,33	0,1	83	258	-16,87
Vita-thion								
Spiked 1	0,07	78	3,34	-21,9	0,07	70	2,89	-29,66
Spiked2	0,05	71	0,41	-28,67	0,05	69	1,26	-30,54
Spiked3	0,1	86	1,85	-13,96	0,1	75	0,75	-25,08

CHAPTER 5: CONCLUSION

In this study, a comparison study of pyrazole capped and uncapped nanomaterials were investigated. The nanomaterials (SeNPs, AgNPs, and CdSQDs) were successfully synthesized via a green method using plant extracts of *allium sativum* cloves, *pelargonium,* and *moringa* leaves. Based on the characterization techniques used, the UV-Visible spectra in the range of 200 – 800 nm showed no shift in wavelength position but an increase in the absorbance in the capped nanomaterials. The HR-TEM analysis confirmed the formation of the nanomaterials, there were no changes in the morphology but there was an increase in the average diameter due to the introduction of the ligand. The FTIR measurements showed no new functional groups but only a shift in the wavenumbers.

There was an overall low cytotoxic effect of the synthesized nanomaterials against MCF-7, A549, and HEK293 cells, the highest percentage activity of 56.9±0.016 and 63.8±0.005 was observed with TRPIDC-CH3 SeNPs and the uncapped CdSDQs, respectively at 100 µg/ml against MCF-7. Although overall cytotoxicity was low, a dose-dependent increase in cytotoxic activity was observed for each of the nanomaterials, as the concentration increased from 50 µg/ml to 100 µg/ml. Low cytotoxic activity was observed with all the screened nanomaterials against HEK293. A morphological examination of MCF-7 Cells was performed on the nanomaterials with the highest percentage of activity (TRPIDC-CH3 SeNPs and uncapped CdSDQs). The controlled cells appeared in normal form and were bound to the surface and MCF-7 cells that were exposed to these nanomaterials lost their normal shape and cell adhesion ability, shrinking and decreasing in cell density.

Furthermore, the interaction between TRPIDC-CH_3 capped and uncapped nanomaterials with HSA by employing spectroscopic techniques under physiological conditions were investigated. The increasing values of K_q with an increase in temperature indicated the presence of a dynamic quenching mechanism. The addition of the ligand changed the quenching mechanism when compared to the uncapped nanomaterials (static quenching mechanism). The values of *n* revealed the presence of a single class of binding sites on HSA with both capped and uncapped. Thermodynamic parameters indicated that the hydrophobic interactions plays a major

role in the interactions of capped nanomaterials with HSA and for the uncapped indicated that van der Waals forces or hydrogens bond. The hydrophobic interactions are relatively stronger than van der Waals forces or hydrogens bond (Atkins *et al.* 2011), therefore it likely that the capped nanomaterials formed stronger complex interactions with HSA. These results make a better understanding of the nanomaterials -proteins interactions, which is important for the further applications of TRPIDC-CH_3 capped nanomaterials in the biological area.

Indirect electrochemical detection of ATP via dual-enzymatic biosensors, using an electroactive species like $[Fe(CN)_6]^{3-/4}$(redox probe) as a reference peak, to observe the behavior of ATP upon its addition. The modified GC electrodes were prepared by simple coating with colloidal solutions of TRPIDC-CH_3 capped or uncapped nanomaterials, MWCNTs and the enzymes GO and Hex at electrode surfaces. Both the sensors with TRPIDC-CH_3 capped or uncapped nanoparticles (SeNPs and AgNPs) exhibits a major improvement in sensitivity, reproducibility (standard deviation <4%), and ease of fabrication of ATP biosensing systems. However, for CdSQDs the addition of the TRPIDC-CH_3 ligand affected the surface area and conductive activity of the sensor leading to a decrease in sensitivity and weakening the electrochemical stability of the QDs.

REFERENCES

Abbas, H. M. K., Kong, X., Wu, J., Ali, M. and Dong, W. 2019. Antimicrobial Potential of Genes from Garlic (Allium sativum L.). In: *Medicinal Plants: Use in Prevention and Treatment of Diseases*. IntechOpen, 25-35.

Abdelhamid, H. N., El-Bery, H. M., Metwally, A. A., Elshazly, M. and Hathout, R. M. 2019. Synthesis of CdS-modified chitosan quantum dots for the drug delivery of Sesamol. *Carbohydrate Polymers*, 214: 90-99.

Aisida, S. O., Madubuonu, N., Alnasir, M. H., Ahmad, I., Botha, S., Maaza, M. and Ezema, F. I. 2020. Biogenic synthesis of iron oxide nanorods using Moringa oleifera leaf extract for antibacterial applications. *Applied Nanoscience*, 10 (1): 305-315.

Al-Shalabi, Z. and Doran, P. M. 2016. Biosynthesis of fluorescent CdS nanocrystals with semiconductor properties: comparison of microbial and plant production systems. *Journal of Biotechnology*, 223: 13-23.

Alagesan, V. and Venugopal, S. 2019. Green synthesis of selenium nanoparticle using leaves extract of withania somnifera and its biological applications and photocatalytic activities. *Bionanoscience*, 9 (1): 105-116.

Alam, M., Alam, M., Hakim, M., Huq, A. O. and Moktadir, S. G. 2014. Development of fiber enriched herbal biscuits: a preliminary study on sensory evaluation and chemical composition. *International Journal of Nutrition and Food Sciences*, 3: 246-250.

Ali, Z. A., Yahya, R., Sekaran, S. D. and Puteh, R. 2016. Green synthesis of silver nanoparticles using apple extract and its antibacterial properties. *Advances in Materials Science and Engineering*, 2016: 1-6.

Amatya, S. P. and Joshi, L. P. 2020. Bio-synthesis of copper nanoparticles (CuNPs) using garlic extract to investigate antibacterial activity. *Bibechana*, 17: 13-19.

Ambika, S. and Sundrarajan, M. 2015. Green biosynthesis of ZnO nanoparticles using Vitex negundo L. extract: spectroscopic investigation of interaction between ZnO nanoparticles and human serum albumin. *Journal of Photochemistry and Photobiology B: Biology*, 149: 143-148.

Anastas, P. T. and Warner, J. C. 1998. Green chemistry. *Frontiers*, 640

Anu, K., Singaravelu, G., Murugan, K. and Benelli, G. 2017. Green-Synthesis of Selenium Nanoparticles Using Garlic Cloves (Allium sativum): Biophysical Characterization and Cytotoxicity on Vero Cells. *Journal of Cluster Science*, 28 (1): 551-563.

Atkins, P. and De Paula, J. 2011. The Gibbs energy of assembly of proteins and biological membranes. In: *Physical Chemistry for the Life Sciences,* Oxford University Press, USA, 95-96.

Babayeju, A., Gbadebo, C., Obalowu, M., Otunola, G., Nmom, I., Kayode, R., Toye, A. and Ojo, F. 2014. Comparison of Organoleptic properties of egusi and efo riro soup blends produced with moringa and spinach leaves. *Food Science and Quality Management*, 28: 15-18.

Baraka, A., Dickson, S., Gobara, M., El-Sayyad, G. S., Zorainy, M., Awaad, M. I., Hatem, H., Kotb, M. M. and Tawfic, A. 2017. Synthesis of silver nanoparticles using natural pigments extracted from Alfalfa leaves and its use for antimicrobial activity. *Chemical Papers*, 71 (11): 2271-2281.

Bardajee, G. R. and Hooshyar, Z. 2016. Interaction of a novel starch-capped CdS quantum dots with human serum albumin and bovine serum albumin. *Starch-Stärke*, 68 (3-4): 329-338.

Beg, M., Maji, A., Mandal, A. K., Das, S., Aktara, M. N., Jha, P. K. and Hossain, M. 2017. Green synthesis of silver nanoparticles using Pongamia pinnata seed: characterization, antibacterial property, and spectroscopic investigation of interaction with human serum albumin. *Journal of Molecular Recognition*, 30 (1): e2565.

Bergman, M. E., Chávez, Á., Ferrer, A. and Phillips, M. A. 2019. Distinct metabolic pathways drive monoterpenoid biosynthesis in a natural population of Pelargonium graveolens. *Journal of Experimental Botany*, 71 (1): 258–271.

Blerot, B., Martinelli, L., Prunier, C., Saint-Marcoux, D., Legrand, S., Bony, A., Sarrabère, L., Gros, F., Boyer, N. and Caissard, J.-C. 2018. Functional analysis of four

terpene synthases in rose-scented pelargonium cultivars (Pelargonium x hybridum) and evolution of scent in the Pelargonium genus. *Frontiers in Plant Science*, 9: 1435.

Borovaya, M., Pirko, Y., Krupodorova, T., Naumenko, A., Blume, Y. and Yemets, A. 2015. Biosynthesis of cadmium sulphide quantum dots by using Pleurotus ostreatus (Jacq.) P. Kumm. *Biotechnology & Biotechnological Equipment*, 29 (6): 1156-1163.

Chakraborti, S., Sarwar, S. and Chakrabarti, P. 2013. The effect of the binding of ZnO nanoparticle on the structure and stability of α-lactalbumin: a comparative study. *The Journal of Physical Chemistry B*, 117 (43): 13397-13408.

Chan, W.-J. J., McLachlan, A. J., Luca, E. J. and Harnett, J. E. 2019. Garlic (Allium sativum L.) in the Management of Hypertension and Dyslipidemia–A Systematic Review. *Journal of Herbal Medicine*: 100292.

Chandramohan, S., Sundar, K. and Muthukumaran, A. 2018. Hollow selenium nanoparticles from potato extract and investigation of its biological properties and developmental toxicity in zebrafish embryos. *IET Nanobiotechnology*, 13 (3): 275 -281.

Chatterjee, T., Pal, A., Dey, S., Chatterjee, B. K. and Chakrabarti, P. 2012. Interaction of virstatin with human serum albumin: spectroscopic analysis and molecular modeling. *PLoS One*, 7 (5): e37468.

Chellapandian, C., Ramkumar, B., Puja, P., Shanmuganathan, R., Pugazhendhi, A. and Kumar, P. 2019. Gold nanoparticles using red seaweed Gracilaria verrucosa: Green synthesis, characterization and biocompatibility studies. *Process Biochemistry*, 80: 58-63.

Chen, C., Liu, C.-H., Cai, J., Zhang, W., Qi, W.-L., Wang, Z., Liu, Z.-B. and Yang, Y. 2018. Broad-spectrum antimicrobial activity, chemical composition and mechanism of action of garlic (Allium sativum) extracts. *Food Control*, 86: 117-125.

Chen, Y., Zhao, J., Du, J., Xu, G., Tang, C. and Geng, B. 2012. Hydrogen sulfide regulates cardiac sarcoplasmic reticulum Ca2+ uptake via KATP channel and PI3K/Akt pathway. *Life Sciences*, 91 (7-8): 271-278.

Chinma, C., Abu, J. and Akoma, S. 2014. Effect of germinated tigernut and moringa flour blends on the quality of wheat-based bread. *Journal of Food Processing and Preservation*, 38 (2): 721-727.

Chinnathambi, S., Abu, N. and Hanagata, N. 2017. Biocompatible CdSe/ZnS quantum dot micelles for long-term cell imaging without alteration to the native structure of the blood plasma protein human serum albumin. *Royal Society of Chemistry: Advances*, 7 (5): 2392-2402.

Chugh, H., Kumar, P., Tomar, V., Kaur, N., Sood, D. and Chandra, R. 2019. Interaction of noscapine with human serum albumin (HSA): A spectroscopic and molecular modelling approach. *Journal of Photochemistry and Photobiology A: Chemistry*, 372: 168-176.

Chung, S., Zhou, R. and Webster, T. J. 2020. Green Synthesized BSA-Coated Selenium Nanoparticles Inhibit Bacterial Growth While Promoting Mammalian Cell Growth. *International Journal of Nanomedicine*, 15: 115.

Dadiboyena, S. and Nefzi, A. 2011. Synthesis of functionalized tetrasubstituted pyrazolyl heterocycles–A review. *European Journal of Medicinal Chemistry*, 46 (11): 5258-5275.

Dar, R. A., Naikoo, G. A., Hassan, I. U. and Shaikh, A. M. 2016. Electrochemical behavior of kaempferol and its determination in presence of quercetin employing multi-walled carbon nanotube modified carbon paste electrode. *Analytical Chemistry Research*, 7: 1-8.

Das, P. E., Abu-Yousef, I. A., Majdalawieh, A. F., Narasimhan, S. and Poltronieri, P. 2020. Green Synthesis of Encapsulated Copper Nanoparticles Using a Hydroalcoholic Extract of Moringa oleifera Leaves and Assessment of Their Antioxidant and Antimicrobial Activities. *Molecules*, 25 (3): 555.

de Marco, B. A., Rechelo, B. S., Tótoli, E. G., Kogawa, A. C. and Salgado, H. R. N. 2019. Evolution of green chemistry and its multidimensional impacts: A review. *Saudi Pharmaceutical Journal*, 27 (1): 1-8.

Devi, S. and Tyagi, S. 2019. Fluorescent determination of trinitrotoluene with bovine serum albumin mediated enhancement of thioglycolic acid capped cadmium selenium quantum dots. *Instrumentation Science & Technology*, 47 (3): 292-311.

El-bakry, K., Toson, E., Serag, M. and Aboser, M. 2016. Hepatoprotective effect of Moringa oleifera leaves extract against carbon tetrachloride-induced liver damage in rats. *World Journal of Pharmacy and Pharmaceutical Sciences,* 5 (5): 76-89.

El-Sayed, E.-S. R., Abdelhakim, H. K. and Ahmed, A. S. 2020. Solid-state fermentation for enhanced production of selenium nanoparticles by gamma-irradiated Monascus purpureus and their biological evaluation and photocatalytic activities. *Bioprocess and Biosystems Engineering*, 43: 797-809.

Elnoby, R. M., Mourad, M. H., Elnaby, S. L. H. and Kana, M. T. A. 2018. Monocrystalline solar cells performance coated by silver nanoparticles: Effect of NPs sizes from point of view Mie theory. *Optics & Laser Technology*, 101: 208-215.

Ennaifer, M., Bouzaiene, T., Messaoud, C. and Hamdi, M. 2018. Phytochemicals, antioxidant, anti-acetyl-cholinesterase, and antimicrobial activities of decoction and infusion of Pelargonium graveolens. *Natural Product Research*, 34 (18): 2634-2638.

Ezhilarasi, A. A., Vijaya, J. J., Kaviyarasu, K., Maaza, M., Ayeshamariam, A. and Kennedy, L. J. 2016. Green synthesis of NiO nanoparticles using Moringa oleifera extract and their biomedical applications: Cytotoxicity effect of nanoparticles against HT-29 cancer cells. *Journal of Photochemistry and Photobiology B: Biology*, 164: 352-360.

Ezhuthupurakkal, P. B., Polaki, L. R., Suyavaran, A., Subastri, A., Sujatha, V. and Thirunavukkarasu, C. 2017. Selenium nanoparticles synthesized in aqueous extract of Allium sativum perturbs the structural integrity of Calf thymus DNA through intercalation and groove binding. *Materials Science and Engineering: C*, 74: 597-608.

Farah, M. A., Ali, M. A., Chen, S.-M., Li, Y., Al-Hemaid, F. M., Abou-Tarboush, F. M., Al-Anazi, K. M. and Lee, J. 2016. Silver nanoparticles synthesized from Adenium obesum leaf extract induced DNA damage, apoptosis and autophagy via generation of reactive oxygen species. *Colloids and Surfaces B: Biointerfaces*, 141: 158-169.

Fardsadegh, B. and Jafarizadeh-Malmiri, H. 2019a. Aloe vera leaf extract mediated green synthesis of selenium nanoparticles and assessment of their in vitro antimicrobial activity against spoilage fungi and pathogenic bacteria strains. *Green Processing and Synthesis*, 8 (1): 399-407.

Fardsadegh, B., Vaghari, H., Mohammad-Jafari, R., Najian, Y. and Jafarizadeh-Malmiri, H. 2019b. Biosynthesis, characterization and antimicrobial activities assessment of fabricated selenium nanoparticles using Pelargonium zonale leaf extract. *Green Processing and Synthesis*, 8 (1): 191-198.

Feng, J.-H., Wei, K.-Z., Gao, J.-P. and Xu, X. 2020. Determination of adenosine phosphates in mouse myocardium tissue by HPLC with UV detection and using porous graphite carbon column. *Journal of Chromatography B*, 1145: 122110.

Freitas, M. C., Cholewa, J. M., Gerosa-Neto, J., Gonçalves, D. C., Caperuto, E. C., Lira, F. S. and Rossi, F. E. 2017. A Single Dose Of Oral Atp Supplementation Improves Performance And Physiological Response During Lower Body Resistance Exercise In Recreational Resistance Trained Males. *Journal of Strength and Conditioning Research*, 33 (12): 3345-3352.

Garmanchuk, L., Borovaya, M., Nehelia, A., Inomistova, M., Khranovska, N., Tolstanova, G., Blume, Y. B. and Yemets, A. 2019. CdS Quantum Dots Obtained by “Green” Synthesis: Comparative Analysis of Toxicity and Effects on the Proliferative and Adhesive Activity of Human Cells. *Cytology and Genetics*, 53 (2): 132-142.

Gholami, Z., Dadmehr, M., Jelodar, N. B., Hosseini, M. and Parizi, A. P. 2020. One-pot biosynthesis of CdS quantum dots through in vitro regeneration of hairy roots of Rhaphanus sativus L. And their apoptosis effect on MCF-7 and AGS cancerous human cell lines. *Materials Research Express*, 7 (1): 015056.

Gunti, L., Kanak, K. R., Mahata, P. K. and Dass, R. S. 2019. Green Synthesis of Selenium Nano-metalloid from the extract of Cabbage (Brassica oleracea var. capitata) leaf and its Antimicrobial Activities. *Journal of Nanoscience Nanoengineering and Applications*, 9 (1): 12-20.

Hamidpour, R., Hamidpour, S., Hamidpour, M., Marshall, V. and Hamidpour, R. 2017. Pelargonium graveolens (Rose Geranium)-A novel therapeutic agent for antibacterial, antioxidant, antifungal and diabetics. *Archives in Cancer Research*, 5: 134.

Hekmat, S., Morgan, K., Soltani, M. and Gough, R. 2015. Sensory evaluation of locally-grown fruit purees and inulin fibre on probiotic yogurt in mwanza, Tanzania and the microbial analysis of probiotic yogurt fortified with Moringa oleifera. *Journal of Health, Population, and Nutrition*, 33 (1): 60.

Hsu, P.-C., Shih, Z.-Y., Lee, C.-H. and Chang, H.-T. 2012. Synthesis and analytical applications of photoluminescent carbon nanodots. *Green Chemistry*, 14 (4): 917-920.

Ilanko, P., McDonnell, P. A., van Vuuren, S. and Cock, I. E. 2019. Interactive antibacterial profile of Moringa oleifera Lam. extracts and conventional antibiotics against bacterial triggers of some autoimmune inflammatory diseases. *South African Journal of Botany*, 124: 420-435.

Ishtikhar, M., Rabbani, G., Khan, S. and Khan, R. H. 2015. Biophysical investigation of thymoquinone binding to ‘N’and ‘B’isoforms of human serum albumin: exploring the interaction mechanism and radical scavenging activity. *Royal Society of Chemistry: Advances*, 5 (24): 18218-18232.

Jacob, J. M., Sharma, S. and Balakrishnan, R. M. 2017. Exploring the fungal protein cadre in the biosynthesis of PbSe quantum dots. *Journal of Hazardous Materials*, 324: 54-61.

Jafarizad, A., Safaee, K., Gharibian, S., Omidi, Y. and Ekinci, D. 2015. Biosynthesis and in-vitro study of gold nanoparticles using mentha and pelargonium extracts. *Procedia Materials Science*, 11: 224-230.

Jegadeesan, G. B., Srimathi, K., Srinivas, N. S., Manishkanna, S. and Vignesh, D. 2019. Green synthesis of iron oxide nanoparticles using Terminalia bellirica and Moringa oleifera fruit and leaf extracts: Antioxidant, antibacterial and thermoacoustic properties. *Biocatalysis and Agricultural Biotechnology*, 21: 101354.

Jiang, Y., Ma, W., Ji, W., Wei, H. and Mao, L. 2019. Aptamer superstructure-based electrochemical biosensor for sensitive detection of ATP in rat brain with in vivo microdialysis. *Analyst*, 144 (5): 1711-1717.

Kalugendo, E. and Kousalya, P. 2019. Synthesis Of Silver Nanoparticles Using Moringa Oleifera Seeds, Glycyrrhiza Glabra Stems, And Its Anti-Methicillin-Resistant Staphylococcus Aureus Activity. *Asian Journal of Pharmaceutical and Clinical Research*, 12 (2): 368-370.

Kandasamy, K., Venkatesh, M., Khadar, Y. S. and Rajasingh, P. 2019. One-pot green synthesis of CdS quantum dots using Opuntia ficus-indica fruit sap. *Materials Today: Proceedings*, 26 (4): 3503-3506.

Kapur, M., Soni, K. and Kohli, K. 2017. Green synthesis of selenium nanoparticles from broccoli, characterization, application and toxicity. *Advanced Techniques in Biology & Medicine*, 5 (1): 2379-1764.

Karim, O., Kayode, R., Oyeyinka, S. and Oyeyinka, A. 2015. Physicochemical properties of stiff dough 'amala'prepared from plantain (Musa Paradisca) flour and Moringa (Moringa oleifera) leaf powder. *Hrana u Zdravlju i Bolesti: Znanstveno-Stručni Časopis za Nutricionizam i Dijetetiku*, 4 (1): 48-58.

Karunanithy, M., Banu, A. A., Ragamathunnisa, M., Saravanakkumar, D. and Ayeshamariam, A. 2019. Bio Synthesis of Zn Doped AgTe with the Help of Allium sativum Peel Powder for Bacterial Results. *European Journal of Medicinal Plants*, 30 (4): 1-8.

Khan, I., Saeed, K. and Khan, I. 2019. Nanoparticles: Properties, applications and toxicities. *Arabian Journal of Chemistry*, 12 (7): 908-931.

Khulu, S. 2015. Interaction studies of chiral non-steroidal anti-inflammatory drugs with HSA protein using capillary electrophoresis frontal analysis and electrokinetic chromatography. Durban University of Technology. Available: http://196.21.61.18/handle/10321/1270 (Accessed 2019-02-09).

Kueng, A., Kranz, C. and Mizaikoff, B. 2004. Amperometric ATP biosensor based on polymer entrapped enzymes. *Biosensors and Bioelectronics*, 19 (10): 1301-1307.

Kumar, B., Smita, K., Cumbal, L. and Debut, A. 2017. Green synthesis of silver nanoparticles using Andean blackberry fruit extract. *Saudi Journal of Biological Sciences*, 24 (1): 45-50.

Kurzawa, C., Hengstenberg, A. and Schuhmann, W. 2002. Immobilization method for the preparation of biosensors based on pH shift-induced deposition of biomolecule-containing polymer films. *Analytical chemistry*, 74 (2): 355-361.

Li, Z., Yin, J., Gao, C., Sheng, L. and Meng, A. 2019. A glassy carbon electrode modified with graphene oxide, poly(3,4-ethylenedioxythiophene), an antifouling peptide and an aptamer for ultrasensitive detection of adenosine triphosphate. *Microchimica Acta*, 186 (2): 1-9.

Liu, X., Atwater, M., Wang, J. and Huo, Q. 2007. Extinction coefficient of gold nanoparticles with different sizes and different capping ligands. *Colloids and surfaces B: Biointerfaces*, 58 (1): 3-7.

Liu, Y., Cui, K., Kong, Q. K., Zhang, L. N., Ge, S. G. and Yu, J. H. 2020. A self-powered origami paper analytical device with a pop-up structure for dual-mode electrochemical sensing of ATP assisted by glucose oxidase-triggered reaction. *Biosensors & Bioelectronics*, 148: 111839.

Liu, Z., Zhong, Y., Hu, Y., Yuan, L., Luo, R., Chen, D., Wu, M., Huang, H. and Li, Y. 2019. Fluorescence strategy for sensitive detection of adenosine triphosphate in terms of evaluating meat freshness. *Food chemistry*, 270: 573-578.

Lu, L., Si, J. C., Gao, Z. F., Zhang, Y., Lei, J. L., Luo, H. Q. and Li, N. B. 2015. Highly selective and sensitive electrochemical biosensor for ATP based on the dual strategy integrating the cofactor-dependent enzymatic ligation reaction with self-cleaving DNAzyme-amplified electrochemical detection. *Biosensors and Bioelectronics*, 63: 14-20.

Maccelli, A., Cesa, S., Cairone, F., Secci, D., Menghini, L., Chiavarino, B., Fornarini, S., Crestoni, M. E. and Locatelli, M. 2020. Metabolic profiling of different wild and

cultivated Allium species based on high-resolution mass spectrometry, high-performance liquid chromatography-photodiode array detector, and color analysis. *Journal of Mass Spectrometry*, 55 (11): e4525.

Machalova, Z., Sajfrtova, M., Pavela, R. and Topiar, M. 2015. Extraction of botanical pesticides from Pelargonium graveolens using supercritical carbon dioxide. *Industrial Crops and Products*, 67: 310-317.

Maduraiveeran, G., Sasidharan, M. and Ganesan, V. 2018. Electrochemical sensor and biosensor platforms based on advanced nanomaterials for biological and biomedical applications. *Biosensors and Bioelectronics*, 103: 113-129.

Mahanthappa, M., Savanur, M. A., Puthusseri, B. and Yellappa, S. 2018. Spectroscopic and electrochemical studies on the molecular interaction between copper sulphide nanoparticles and bovine serum albumin. *Journal of Materials Science*, 53 (1): 202-214.

Maiyo, F. and Singh, M. 2017. Selenium nanoparticles: Potential in cancer gene and drug delivery. *Nanomedicine*, 12 (9): 1075-1089.

Majeed, S., bin Abdullah, M. S., Nanda, A. and Ansari, M. T. 2016. In vitro study of the antibacterial and anticancer activities of silver nanoparticles synthesized from Penicillium brevicompactum (MTCC-1999). *Journal of Taibah University for Science*, 10 (4): 614-620.

Makarov, V., Love, A., Sinitsyna, O., Makarova, S., Yaminsky, I., Taliansky, M. and Kalinina, N. 2014. “Green” nanotechnologies: synthesis of metal nanoparticles using plants. *Acta Naturae*, 6 (1 (20)): 35-44.

Makhanya, T. R. 2019. Synthesis, characterisation and biological activity of selected pyrazoles and naphthyrides. Durban University of Technology. Available: http://hdl.handle.net/10321/3211 (Accessed 2019-10-18).

Manjubaashini, N., Sephra, P. J., Nehru, K., Sivakumar, M. and Thangadurai, T. D. 2019. Electrochemical determination of ATP at rhodamine6G capped gold nanoparticles modified carbon felt electrode at pH 7.2. *Sensors and Actuators B: Chemical*, 281: 1054-1062.

Matinise, N., Fuku, X., Kaviyarasu, K., Mayedwa, N. and Maaza, M. 2017. ZnO nanoparticles via Moringa oleifera green synthesis: Physical properties & mechanism of formation. *Applied Surface Science*, 406: 339-347.

Medda, S., Hajra, A., Dey, U., Bose, P. and Mondal, N. K. 2015. Biosynthesis of silver nanoparticles from Aloe vera leaf extract and antifungal activity against Rhizopus sp. and Aspergillus sp. *Applied Nanoscience*, 5 (7): 875-880.

Mellinas, C., Jiménez, A. and Garrigós, M. d. C. 2019. Microwave-Assisted Green Synthesis and Antioxidant Activity of Selenium Nanoparticles Using Theobroma cacao L. Bean Shell Extract. *Molecules*, 24 (22): 4048.

Modi, S. and Fulekar, M. 2019. Green Synthesis of Zinc Oxide Nanoparticles using Garlic skin extract and Its Characterization. *Journal of Nanostructures*, 10 (1): 20-27.

Mohammadlou, M., Jafarizadeh-Malmiri, H. and Maghsoudi, H. 2017. Hydrothermal green synthesis of silver nanoparticles using Pelargonium/Geranium leaf extract and evaluation of their antifungal activity. *Green Processing and Synthesis*, 6 (1): 31-42.

Mpanza, T., Sabela, M. I., Mathenjwa, S. S., Kanchi, S. and Bisetty, K. 2014. Electrochemical determination of capsaicin and silymarin using a glassy carbon electrode modified by gold nanoparticle decorated multiwalled carbon nanotubes. *Analytical Letters*, 47 (17): 2813-2828.

Nabikhan, A., Kandasamy, K., Raj, A. and Alikunhi, N. M. 2010. Synthesis of antimicrobial silver nanoparticles by callus and leaf extracts from saltmarsh plant, Sesuvium portulacastrum L. *Colloids and surfaces B: Biointerfaces*, 79 (2): 488-493.

Ocsoy, I., Tasdemir, D., Mazicioglu, S. and Tan, W. 2018. Nanotechnology in plants. In: *Plant Genetics and Molecular Biology*. Springer, 263-275.

Owen, P. D. 2010. Limitations of the relative standard deviation of win percentages for measuring competitive balance in sports leagues. *Economics Letters*, 109 (1): 38-41.

Oyeyinka, A. T. and Oyeyinka, S. A. 2018. Moringa oleifera as a food fortificant: Recent trends and prospects. *Journal of the Saudi Society of Agricultural Sciences*, 17 (2): 127-136.

Pandian, M., Marimuthu, R., Natesan, G., Rajagopal, R. E., Justin, J. and Mohideen, A. 2013. Development of biogenic silver nano particle from Pelargonium graveolens leaf extract and their antibacterial activity. *American Journal of Nanoscience and Nanotechnology*, 1 (2): 57-64.

Pansare, A. V., Shedge, A. A. and Patil, V. R. 2018. Discrete SeNPs-Macromolecule Binding Manipulated by Hydrophilic Interaction. *International Journal of Biological Macromolecules*, 107: 1982-1987.

Pawlowska, A. and Sadowski, Z. 2017. Biosynthesis of copper nanoparticles using aqueous extracts of aloe vera and geranium and bioleaching solutions. In: Proceedings of *Solid State Phenomena*. Trans Tech Publications, 193-196.

Peteu, S. F., Russell, S. A., Galligan, J. J. and Swain, G. M. 2020. An Electrochemical ATP Biosensor with Enzymes Entrapped within a PEDOT Film. *Electroanalysis*: 12.

Phan, A. D. T., Netzel, G., Chhim, P., Netzel, M. E. and Sultanbawa, Y. 2019. Phytochemical Characteristics and Antimicrobial Activity of Australian Grown Garlic (Allium Sativum L.) Cultivars. *Foods*, 8 (9): 358.

Prasanth, S. and Sudarsanakumar, C. 2017. Elucidating the interaction of L-cysteine-capped selenium nanoparticles and human serum albumin: spectroscopic and thermodynamic analysis. *New Journal of Chemistry*, 41 (17): 9521-9530.

Pratiwi, D. E., Side, S. and Nisa, N. A. T. 2019. Synthesis of Silver Nanoparticles Using Moringa oleifera L. Leaf Extract as Bioreductor. In: Proceedings of *Materials Science Forum*. Trans Tech Publications, 145-149.

Preeti, S. and Gaurava, S. 2018. Pharmacological and phytochemical screening of Desmodium gangeticum and Moringa oleifera. *Research Journal of Chemistry and Environment*, 22 (5): 6-10.

Qin, Z., Yue, Q., Liang, Y., Zhang, J., Zhou, L., Hidalgo, O. B. and Liu, X. 2018. Extracellular biosynthesis of biocompatible cadmium sulfide quantum dots using trametes versicolor. *Journal of Biotechnology*, 284: 52-56.

Rajkumar, K., Sandhya, M., Koganti, S. and Burgula, S. 2020. Selenium Nanoparticles Synthesized Using Pseudomonas stutzeri (MH191156) Show Antiproliferative and Anti-angiogenic Activity Against Cervical Cancer Cells. *International Journal of Nanomedicine*, 15: 4523-4540.

Rauwel, P., Küünal, S., Ferdov, S. and Rauwel, E. 2015. A review on the green synthesis of silver nanoparticles and their morphologies studied via TEM. *Advances in Materials Science and Engineering*, 2015: 1-9.

Reddy, G. D., Noorjahan, M., Mangatayaru, K. G. and Krishnakanth, M. 2018. Microwave assisted phytosynthesis and characterization of magnetic iron oxide quantum dots using Moringa oleifera. *Material Science Research India*, 15 (2): 145-150.

Rezanejade Bardajee, G., Hooshyar, Z., Rezaei, M., Khalili Khaneghah, M. and Fallahnejad, F. 2017. Spectroscopic studies on the interactions of capped CdS quantum dots with human serum albumin (HSA) and bovine serum albumin (BSA). *Inorganic and Nano-Metal Chemistry*, 47 (5): 688-696.

Rose, P., Moore, P. K. and Zhu, Y.-Z. 2018. Garlic and gaseous mediators. *Trends in Pharmacological Sciences*, 39 (7): 624-634.

Ryavanaki, L., Tsai, H. and Fuh, C. B. 2020. Microwave Synthesis of Gold Nanoclusters with Garlic Extract Modifications for the Simple and Sensitive Detection of Lead Ions. *Nanomaterials*, 10 (1): 94.

Sabela, M. I., Makhanya, T., Kanchi, S., Shahbaaz, M., Idress, D. and Bisetty, K. 2018. One-pot biosynthesis of silver nanoparticles using Iboza Riparia and Ilex Mitis for cytotoxicity on human embryonic kidney cells. *Journal of Photochemistry and Photobiology B: Biology*, 178: 560-567.

Saha, M. and Bandyopadhyay, P. K. 2019. Green Biosynthesis of Silver Nanoparticle Using Garlic, Allium sativum with Reference to Its Antimicrobial Activity Against the Pathogenic Strain of Bacillus sp. and Pseudomonas sp. Infecting Goldfish, Carassius auratus. In: Proceedings of *Proceedings of the Zoological Society*. Springer, 180-186.

Saini, R. K., Shetty, N. P. and Giridhar, P. 2014. Carotenoid content in vegetative and reproductive parts of commercially grown Moringa oleifera Lam. cultivars from India by LC–APCI–MS. *European Food Research and Technology*, 238 (6): 971-978.

Sang, F., Zhang, X., Liu, J., Yin, S. and Zhang, Z. 2019. A label-free hairpin aptamer probe for colorimetric detection of adenosine triphosphate based on the anti-aggregation of gold nanoparticles. *Spectrochimica Acta Part A: Molecular and Biomolecular Spectroscopy*, 217: 122-127.

Sarpong, K. A., Zhang, K., Luan, Y., Cao, Y. and Xu, W. 2020. Development and application of a novel electrochemical sensor based on AuNPS and difunctional monomer-MIPs for the selective determination of Tetrabromobisphenol-S in water samples. *Microchemical Journal*, 154: 104526.

Satgurunathan, T., Bhavan, P. S. and Komathi, S. 2017. Green synthesis of selenium nanoparticles from sodium selenite using garlic extract and its enrichment on Artemia nauplii to feed the freshwater prawn Macrobrachium rosenbergii post-larvae. *Research Journal of Chemistry and Environment*, 21 (10): 1-12.

Seetha, J., Mallavarapu, U. m., Akepogu, P., Mesa, A., Gollapudi, V. R., Natarajan, H. and Anumakonda, V. R. 2020. Biosynthesis and study of bimetallic copper and silver nanoparticles on cellulose cotton fabrics using Moringa oliefiera leaf extraction as reductant. *Inorganic and Nano-Metal Chemistry*, 50 (9): 828-835.

Shaheen, F., Aziz, M. H., Fatima, M., Khan, M. A., Ahmed, F., Ahmad, R., Ahmad, M. A., Alkhuraiji, T. S., Akram, M. W. and Raza, R. 2018. In Vitro cytotoxicity and morphological assessments of GO-ZnO against the MCF-7 Cells: Determination of singlet oxygen by chemical trapping. *Nanomaterials*, 8 (7): 539.

Shameli, K., Bin Ahmad, M., Jaffar Al-Mulla, E. A., Ibrahim, N. A., Shabanzadeh, P., Rustaiyan, A., Abdollahi, Y., Bagheri, S., Abdolmohammadi, S. and Usman, M. S. 2012. Green biosynthesis of silver nanoparticles using Callicarpa maingayi stem bark extraction. *Molecules*, 17 (7): 8506-8517.

Shao, S., Tang, Y.-j., Dai, S.-y., Zhou, Y.-t., Cheng, G.-f., HE, P.-g. and Fang, Y.-z. 2018. A Highly Sensitive Electrochemical Biosensor for Detection of Adenosine

Triphosphate Based on Space Block. *Chinese Journal of Analytical Chemistry*, 46 (2): 254-259.

Sharma, D., Sabela, M. I., Kanchi, S., Mdluli, P. S., Singh, G., Stenström, T. A. and Bisetty, K. 2016. Biosynthesis of ZnO nanoparticles using Jacaranda mimosifolia flowers extract: Synergistic antibacterial activity and molecular simulated facet specific adsorption studies. *Journal of Photochemistry and Photobiology B: Biology*, 162: 199-207.

Sheikhlou, K., Allahyari, S., Sabouri, S., Najian, Y. and Jafarizadeh-Malmiri, H. 2020. Walnut leaf extract-based green synthesis of selenium nanoparticles via microwave irradiation and their characteristics assessment. *Open Agriculture*, 5 (1): 227-235.

Shivaji, K., Mani, S., Ponmurugan, P., De Castro, C. S., Lloyd Davies, M., Balasubramanian, M. G. and Pitchaimuthu, S. 2018. Green-Synthesis-Derived CdS Quantum Dots Using Tea Leaf Extract: Antimicrobial, Bioimaging, and Therapeutic Applications in Lung Cancer Cells. *ACS Applied Nano Materials*, 1 (4): 1683-1693.

Shrestha, D., Sapkota, H., Baidya, P. and Basnet, S. 2016. Antioxidant and antibacterial activities of Allium sativum and Allium cepa. *Bulletin of Pharmaceutical Research*, 6 (2): 50-55.

Siddiqui, M. H., Al-Whaibi, M. H., Firoz, M. and Al-Khaishany, M. Y. 2015. Role of nanoparticles in plants. In: *Nanotechnology and Plant Sciences*. Springer, 19-35.

Suresh, S., Chhipa, A. S., Gupta, M., Lalotra, S., Sisodia, S. S., Baksi, R. and Nivsarkar, M. 2020. Phytochemical analysis and pharmacological evaluation of methanolic leaf extract of Moringa oleifera Lam. in ovalbumin induced allergic asthma. *South African Journal of Botany*, 130: 484-493.

Sut, S., Maggi, F., Bruno, S., Badalamenti, N., Quassinti, L., Bramucci, M., Beghelli, D., Lupidi, G. and Dall'Acqua, S. 2020. Hairy Garlic (Allium subhirsutum) from Sicily (Italy): LC-DAD-MSn Analysis of Secondary Metabolites and in Vitro Biological Properties. *Molecules*, 25 (12): 2837.

Tian, Y.-F., Zhou, W., Yin, B.-C. and Ye, B.-C. 2017. Highly sensitive surface-enhanced Raman scattering detection of adenosine triphosphate based on core–satellite assemblies. *Analytical Methods*, 9 (42): 6038-6043.

Tiloke, C., Phulukdaree, A., Gengan, R. M. and Chuturgoon, A. A. 2019. Moringa oleifera aqueous leaf extract induces cell-cycle arrest and apoptosis in human liver hepatocellular carcinoma cells. *Nutrition and cancer*, 71 (7): 1165-1174.

Tippayawat, P., Phromviyo, N., Boueroy, P. and Chompoosor, A. 2016. Green synthesis of silver nanoparticles in aloe vera plant extract prepared by a hydrothermal method and their synergistic antibacterial activity. *PeerJ*, 4: e2589.

Vahidi, A., Vaghari, H., Najian, Y., Najian, M. J. and Jafarizadeh-Malmiri, H. 2019. Evaluation of three different green fabrication methods for the synthesis of crystalline ZnO nanoparticles using Pelargonium zonale leaf extract. *Green Processing and Synthesis*, 8 (1): 302-308.

Vivek, R., Thangam, R., Muthuchelian, K., Gunasekaran, P., Kaveri, K. and Kannan, S. 2012. Green biosynthesis of silver nanoparticles from Annona squamosa leaf extract and its in vitro cytotoxic effect on MCF-7 cells. *Process Biochemistry*, 47 (12): 2405-2410.

Wang, P., Cheng, Z., Chen, Q., Qu, L., Miao, X. and Feng, Q. 2018. Construction of a paper-based electrochemical biosensing platform for rapid and accurate detection of adenosine triphosphate (ATP). *Sensors and Actuators B: Chemical*, 256: 931-937.

Weber, C. 2014. The challenge of ATP biosensing-application, investigation and further development of ATP microbiosensors. Ulm University Available: http://dx.doi.org/10.18725/OPARU-2649 (Accessed 2020-03-04).

Wu, X.-Q., Huang, C., Jia, Y.-M., Song, B.-A., Li, J. and Liu, X.-H. 2014. Novel coumarin-dihydropyrazole thio-ethanone derivatives: design, synthesis and anticancer activity. *European journal of medicinal chemistry*, 74: 717-725.

Xia, Y., Xiao, M., Zhao, M., Xu, T., Guo, M., Wang, C., Li, Y., Zhu, B. and Liu, H. 2020. Doxorubicin-loaded functionalized selenium nanoparticles for enhanced antitumor

efficacy in cervical carcinoma therapy. *Materials Science and Engineering: C*, 106: 110100.

Xiao, Q., Feng, J., Feng, M., Li, J., Liu, Y., Wang, D. and Huang, S. 2019. A ratiometric electrochemical aptasensor for ultrasensitive determination of adenosine triphosphate via a triple-helix molecular switch. *Microchimica Acta*, 186 (7): 478.

Yee, M. M. 2019. Investigation of Chemical Composition, Antimicrobial and Antioxidant Activities of Allium Wallichii Kunth (Garlic) Bulb. *American Scientific Research Journal for Engineering, Technology, and Sciences*, 54 (1): 30-41.

Yusefi, M., Shameli, K., Ali, R. R., Pang, S.-W. and Teow, S.-Y. 2020. Evaluating anticancer activity of plant-mediated synthesized iron oxide nanoparticles using Punica Granatum fruit peel extract. *Journal of Molecular Structure*, 1204: 127539.

Zhang, Y., Yang, D., Kong, Y., Wang, X., Pandoli, O. and Gao, G. 2010. Synergetic antibacterial effects of silver nanoparticles@ aloe vera prepared via a green method. *Nano Biomedicine and Engineering*, 2 (4): 252-257.

Zhao, B., Lan, T., Li, H., He, Y., Wu, D. and Chen, Z. 2019. Antioxidation activity of Moringa oleifera Lam. leaves extract on soybean oil during both storage and thermal treatment. *Journal of Food Processing and Preservation*: e13975.

Zhu, Q., Cai, Y., Fang, L., Liang, X., Ye, X. and Liang, B. 2018. A Lithops-Like Pt Nanorods Modified Microelectrode Array for Cellular ATP Release Detection. In: Proceedings of *2018 IEEE SENSORS*. IEEE, 1-3.

APPENDIX A: fluorescence quenching results of uncapped SeNPs

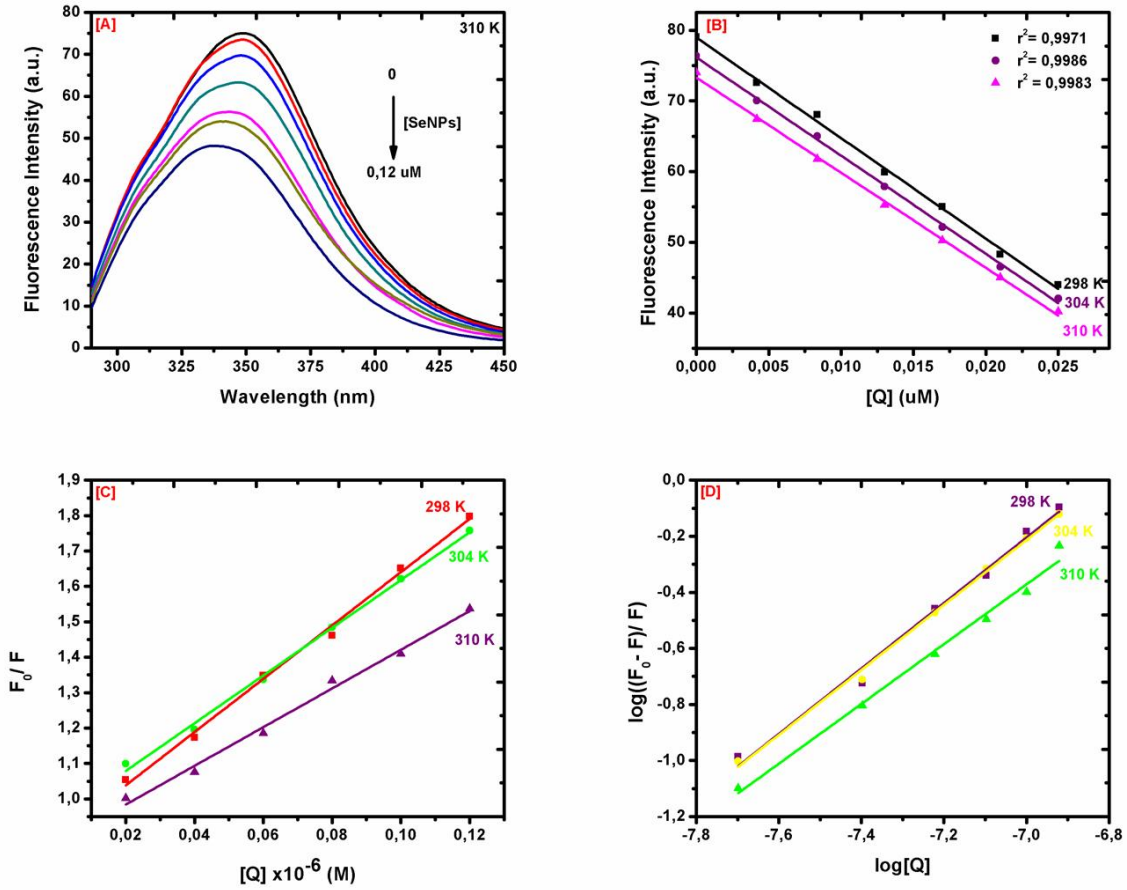

(A) Fluorescence quenching of HSA in the presence of different concentrations of SeNPs. **(B)** linear fit of the absorbances complex vs increasing concentration of SeNPs at 345 nm at different temperatures. **(C)** Stern–Volmer curves for the binding of HSA with SeNPs at different temperatures. **(D)** log[(F_0 / F)/F] versus log[Q] plots for HSA versus SeNPs at different temperatures.

APPENDIX B: fluorescence spectra of HSA-TRPIDC-CH_3 SeNPs at different temperatures

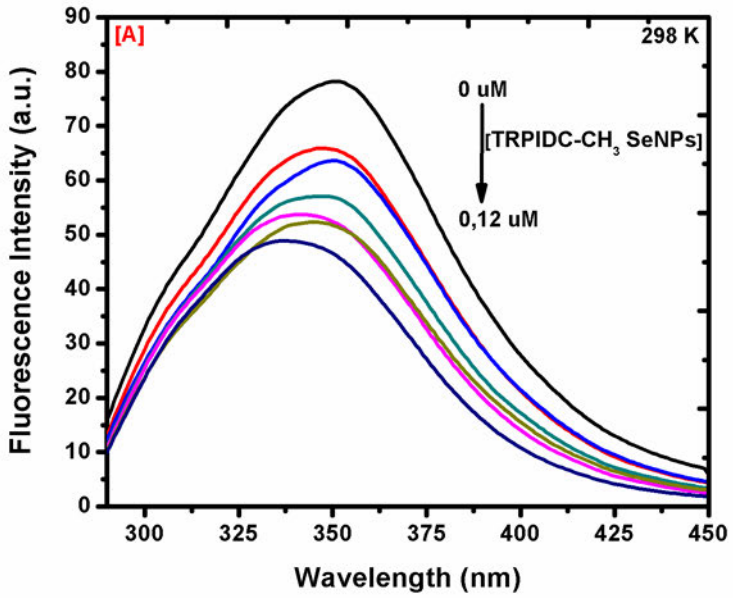

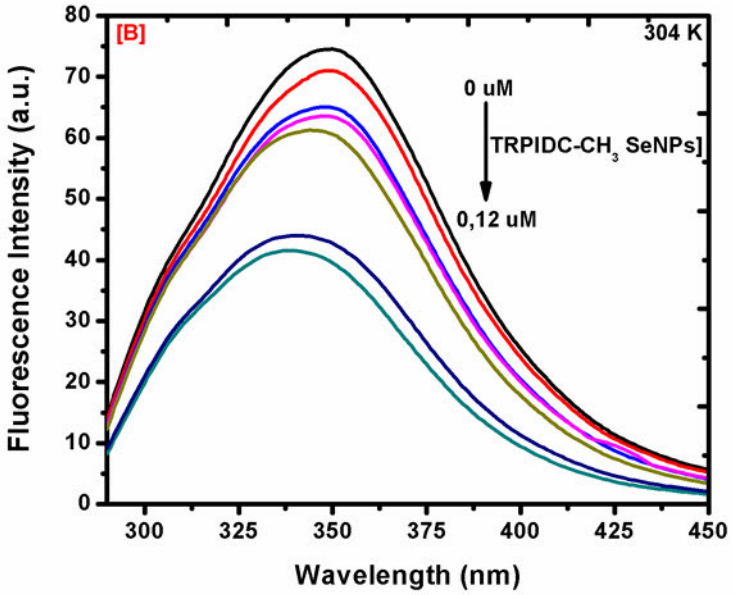

APPENDIX C: fluorescence spectra of HSA-SeNPs at different temperatures

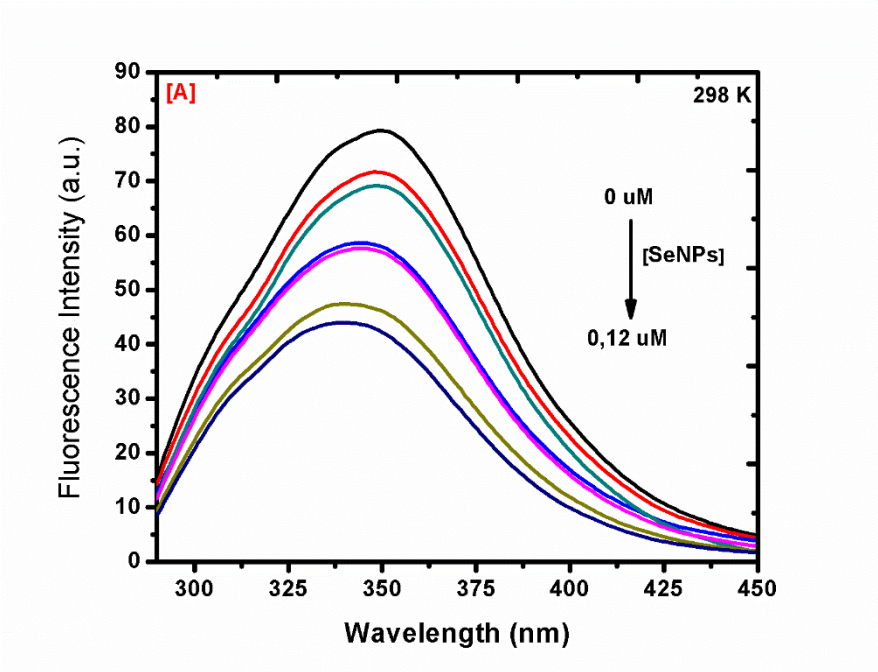

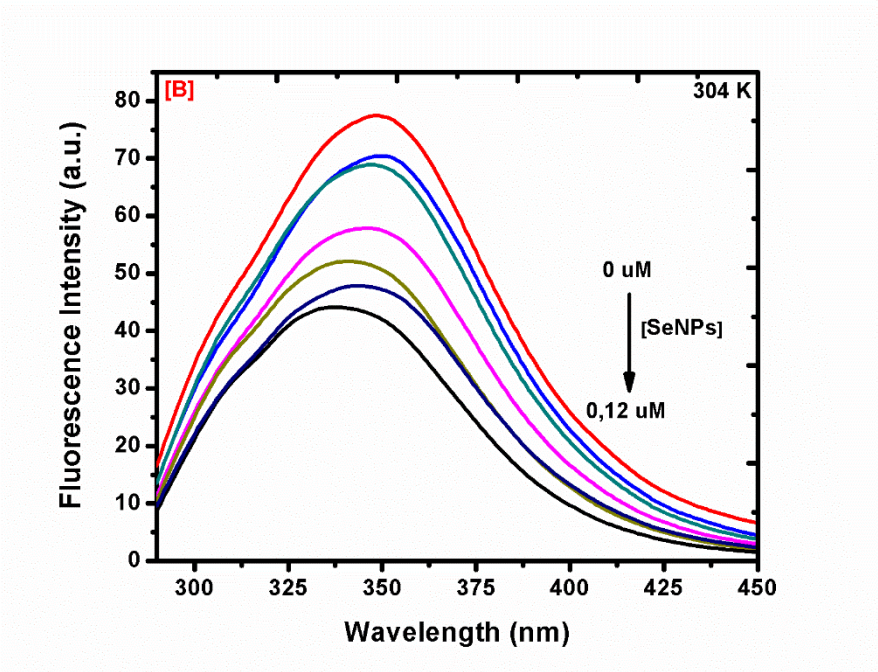

APPENDIX D: fluorescence quenching results of uncapped AgNPs

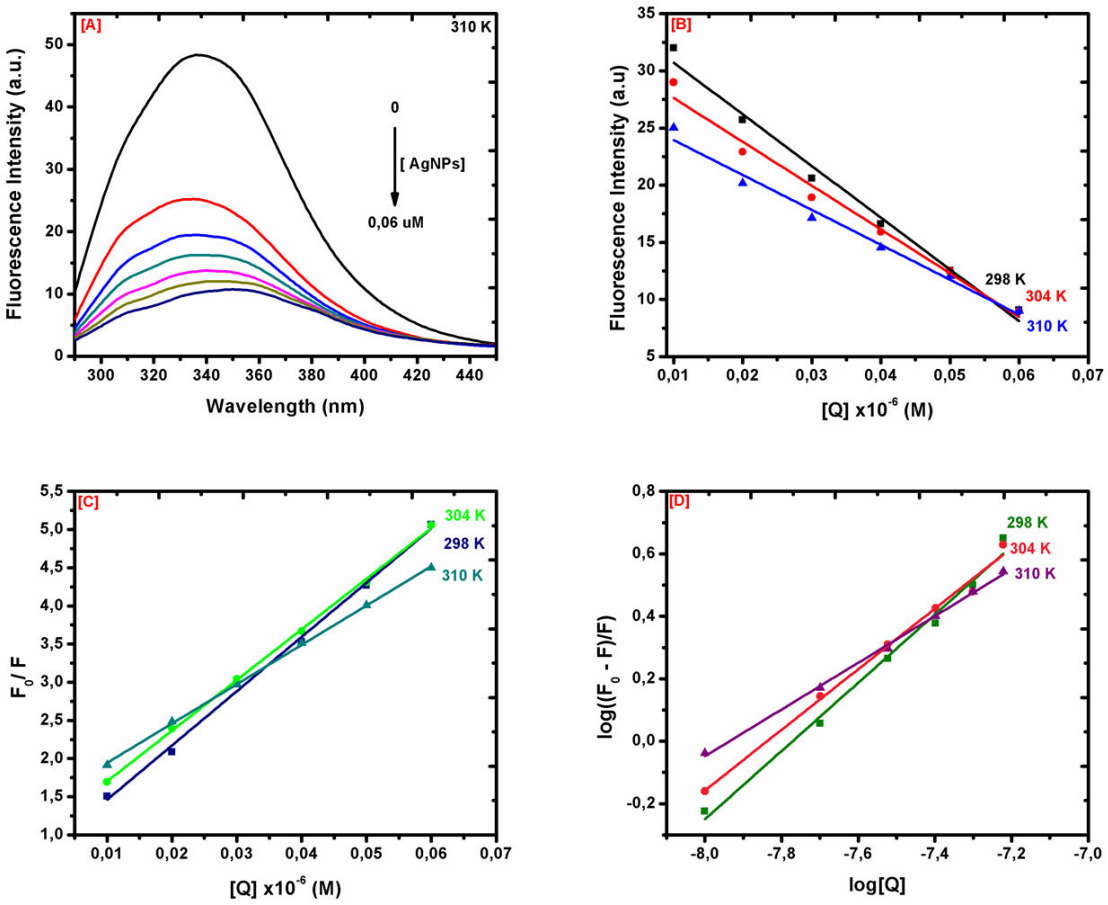

(A) Fluorescence quenching of HSA in the presence of different concentrations of AgNPs. **(B)** linear fit of the absorbances complex vs increasing concentration of AgNPs at 345 nm at different temperatures. **(C)** Stern–Volmer curves for the binding of HSA with AgNPs at different temperatures. **(D)** log[(F_0 / F)/F] versus log[Q] plots for HSA versus AgNPs at different temperatures.

APPENDIX E: fluorescence spectra of HSA-TRPIDC-CH_3 AgNPs at different temperatures

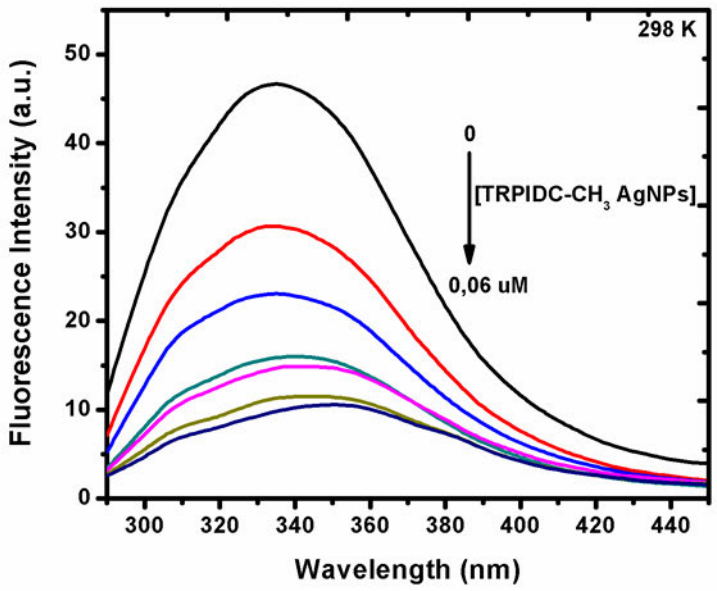

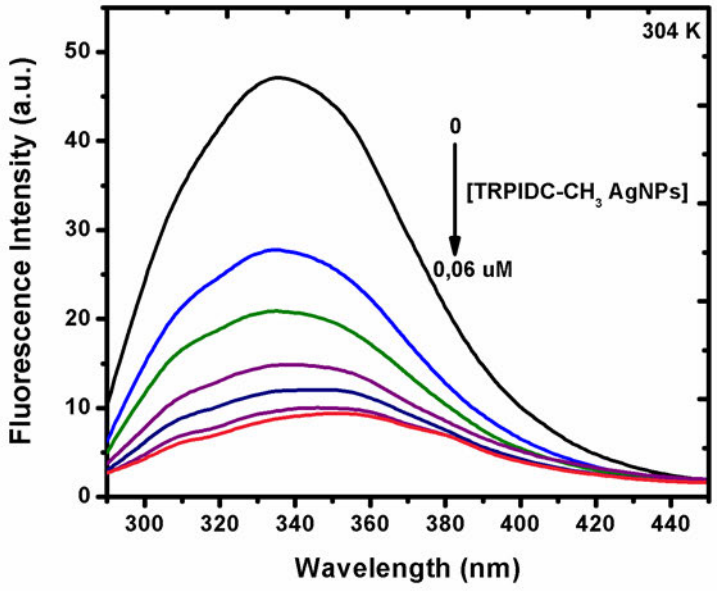

APPENDIX F: fluorescence spectra of HSA-SeNPs at different temperatures

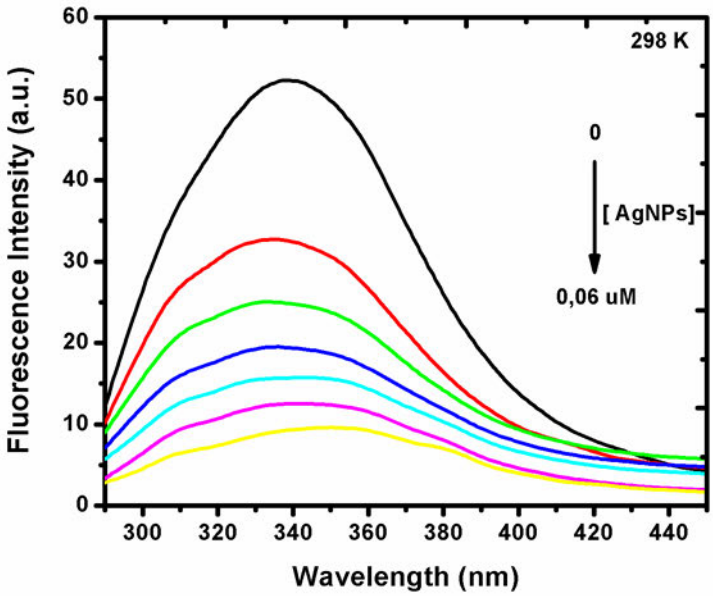

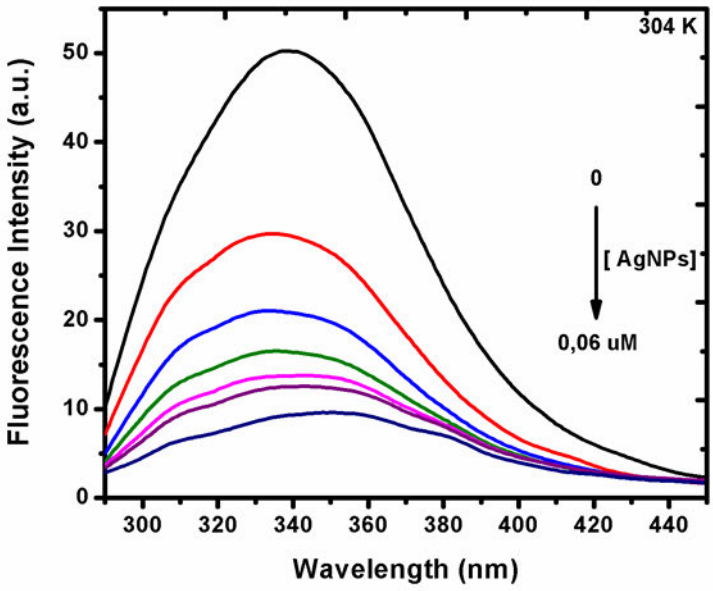

APPENDIX G: fluorescence quenching results of uncapped CdSQDs

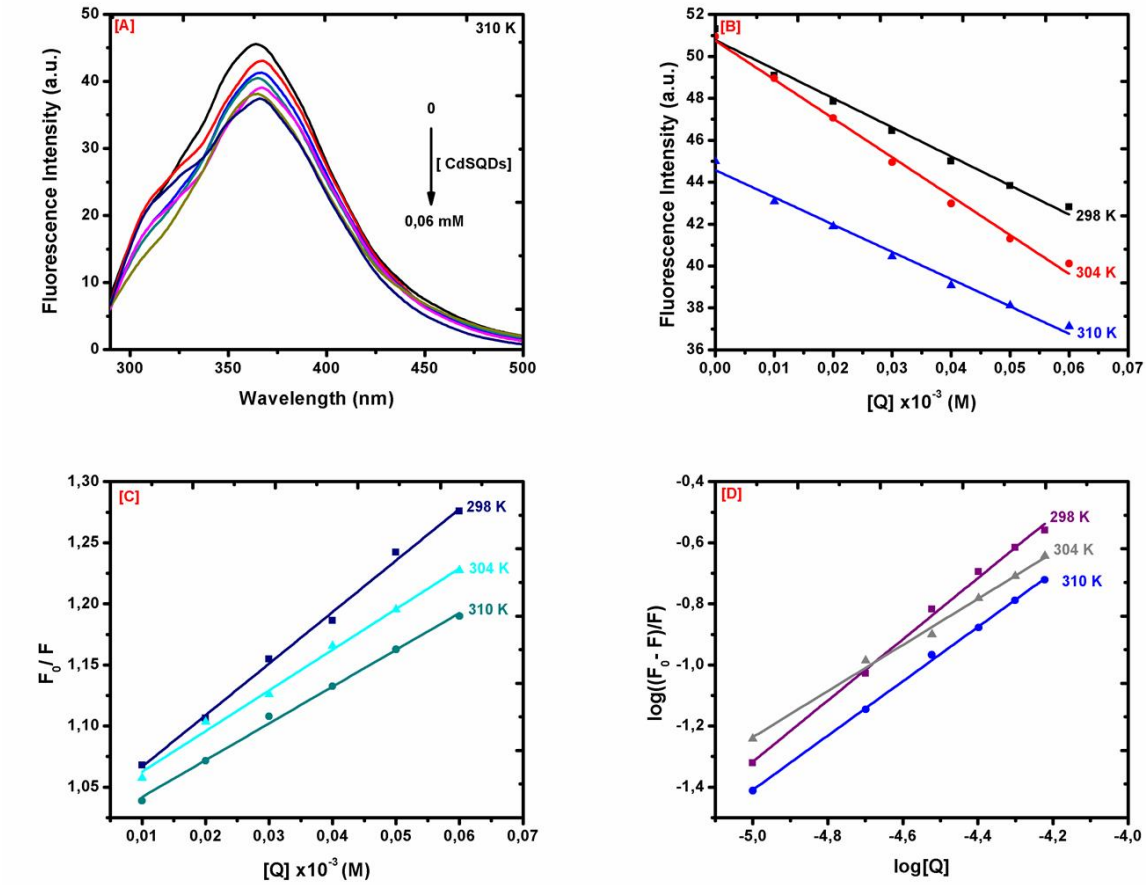

(A) Fluorescence spectrum of HSA in the presence of different concentrations of CdSQDs. **(B)** linear fit of the absorbances complex and increasing concentration of CdSQDs at 345 nm at different temperatures. **(C)** Stern–Volmer curves for the binding of HSA with CdSQDs at different temperatures. **(D)** log[(F_0 / F)/F] versus log[Q] plots for HSA versus CdSQDs at different temperatures.

APPENDIX H: fluorescence spectra of HSA-TRPIDC-CH_3 CdSQDs at different temperatures

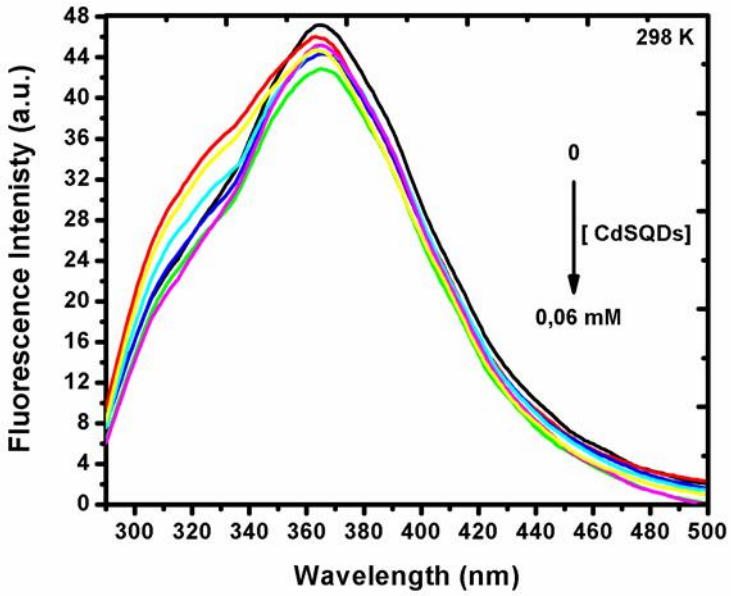

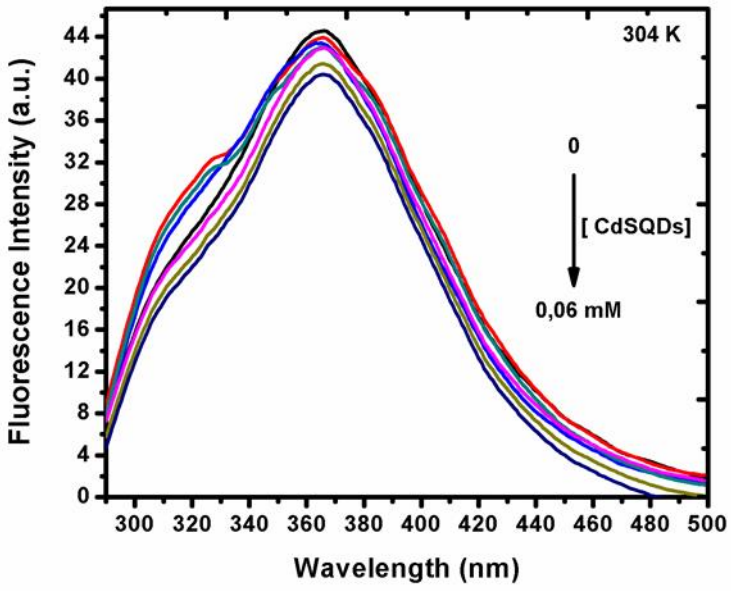

APPENDIX I: fluorescence spectra of HSA-CdSQDs at different temperatures

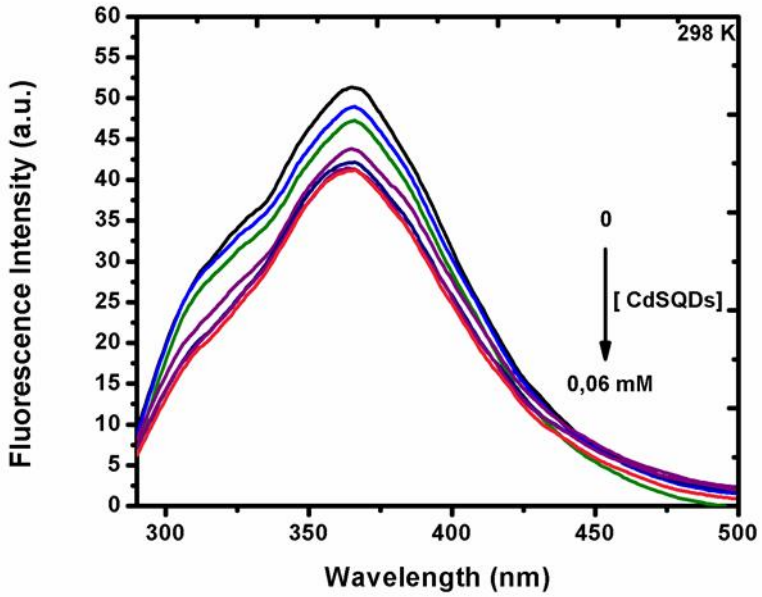

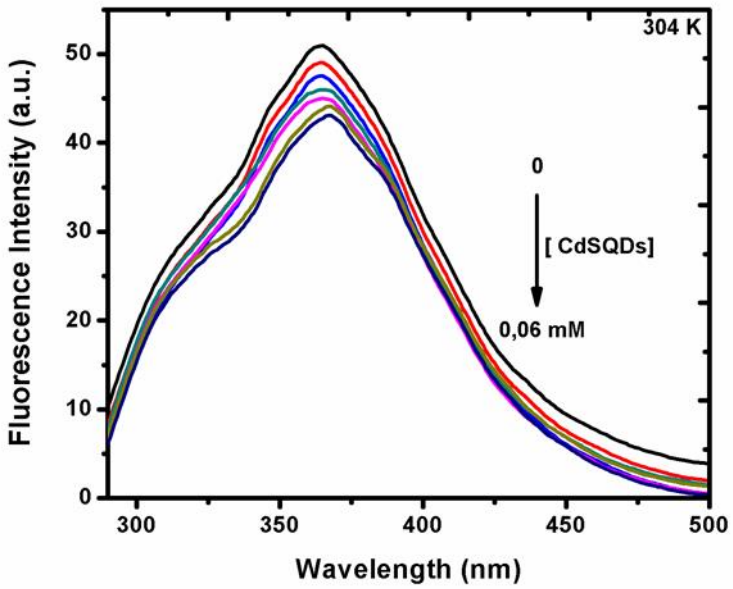

APPENDIX J: Cyclic voltammetry data of 0.02 mM ATP in the phosphate buffers of different pH values. (Scan rate = 100 mV/s)

Table 16.1: Ip_c/Ip_a data of capped and uncapped SeNPs

	GCE/MWCNTs/TRPIDC-CH3 SeNPs			GCE/MWCNTs/SeNPs		
pH	**Ip_a (uA)**	**Ip_c (uA)**	**Ip_c/Ip_a**	**Ip_a (uA)**	**Ip_c (uA)**	**Ip_c/Ip_a**
5	69,07	-71,85	-1,04025	90,11	-111,22	-1,23427
6	44,53	-54,08	-1,21446	77,04	-89,53	-1,16212
7	21,14	-21,56	-1,01987	69,07	-71,69	-1,03793
8	17,37	-16,77	-0,96546	59,52	-56,78	-0,95397
9	16,02	-13,76	-0,85893	55,02	49,94	0,90767

Table 16.2: Ip_c/Ip_a data of capped and uncapped AgNPs

	GCE/MWCNTs/TRPIDC-CH3 AgNPs			GCE/MWCNTs/AgNPs		
pH	**Ip_a (uA)**	**Ip_c (uA)**	**Ip_c/Ip_a**	**Ip_a (uA)**	**Ip_c (uA)**	**Ip_c/Ip_a**
5	15,22	-15,30	-1,00526	18,88	-19,05	-1,00900
6	13,70	-13,46	-0,98248	17,68	-17,56	-0,99321
7	12,82	-10,90	-0,85023	17,02	-13,95	-0,81962
8	9,01	-6,73	-0,74694	10,82	-8,42	-0,77819
9	8,05	-5,66	0,70311	6,06	-3,90	-0,64356

Table 16.3: Ip_c/Ip_a data of capped and uncapped CdSQDs

	GCE/MWCNTs/TRPIDC-CH3CdSQDs			GCE/MWCNTs/CdSQDs		
pH	**Ip_a (uA)**	**Ip_c (uA)**	**Ip_c/Ip_a**	**Ip_a (uA)**	**Ip_c (uA)**	**Ip_c/Ip_a**
5	45,25	-37,10	-0,81989	10,60	-14,50	-1,36792
6	29,00	-23,08	-0,79586	11,86	-14,50	-1,22260
7	22,05	-13,87	-0,62902	10,49	-10,37	-0,98856
8	11,37	-9,79	-0,86104	9,02	-7,48	-0,82926
9	8,25	-6,93	-0,84000	7,64	-5,79	-0,75783

APPENDIX K: cytotoxicity activity of the nanomaterials against the three cells

Table 17.1: Cytotoxicity activity of the nanomaterials against MCF-7

Nanomaterials	Percentage Cytotoxicity **MCF-7**	
	100 µg/ml	**50 µg/ml**
TRPIDC-CH_3 SeNPs	56.9 ± 0.016^{ey}	13.3 ± 0.026^{bx}
Uncapped SeNPs	32.6 ± 0.027^{cx}	40.7 ± 0.003^{ey}
TRPIDC-CH_3 AgNPs	25.8 ± 0.086^{bx}	29.5 ± 0.064^{dy}
Uncapped AgNPs	18.7 ± 0.022^{ax}	18.9 ± 0.012^{cy}
TRPIDC-CH_3 CdSQDs	34.6 ± 0.091^{dy}	11.8 ± 0.029^{ax}
Uncapped CdSQDs	63.8 ± 0.005^{fy}	49.1 ± 0.013^{fx}
Doxorubicin	97.4 ± 0.03^{gy}	94.3 ± 0.05^{gy}

Values are represented mean ±SD, Means of growth inhibition without a common letter differ significantly (P<0.05), a,b,c,d,e,f,g shows differences per row and x ,y shows differences between different concentrations.

Table 17.2: Cytotoxicity activity of the nanomaterials against A549

Nanomaterials	Percentage Cytotoxicity **A549**	
	100 µg/ml	**50 µg/ml**
TRPIDC-CH_3 SeNPs	45.6 ± 0.19^{ey}	9.4 ± 0.13^{bx}
Uncapped SeNPs	60.9 ± 0.13^{fy}	41.2 ± 0.00^{fx}
TRPIDC-CH_3 AgNPs	31.7 ± 0.025^{ay}	27.3 ± 0.01^{dx}
Uncapped AgNPs	38.0 ± 0.04^{by}	3.04 ± 0.07^{ax}
TRPIDC-CH_3 CdSQDs	41.8 ± 0.09^{cy}	22.2 ± 0.06^{cx}
Uncapped CdSQDs	43.7 ± 0.15^{dy}	29.4 ± 0.03^{ex}
Doxorubicin	98.1 ± 0.09^{gy}	89.04 ± 0.01^{gy}

Values are represented mean ±SD, Means of growth inhibition without a common letter differ significantly (P<0.05), a,b,c,d,e,f,g shows differences per row and x ,y shows differences between different concentrations.

Table 17.3: Cytotoxicity activity of the nanomaterials against HEK293

Nanomaterials	Percentage Cytotoxicity **HEK293**	
	100 µg/ml	**50 µg/ml**
TRPIDC-CH_3 SeNPs	-154.1 ± 0.012^{cx}	-93.4 ± 0.009^{by}
Uncapped SeNPs	-159.2 ± 0.022^{bx}	-90.6 ± 0.014^{cy}
TRPIDC-CH_3 AgNPs	1.8 ± 0.005^{dy}	-2.53 ± 0.002^{dx}
Uncapped AgNPs	-172.2 ± 0.01^{ax}	-98.2 ± 0.004^{ay}
TRPIDC-CH_3 CdSQDs	2.04 ± 0.007^{ey}	0.5 ± 0.025^{fx}
Uncapped CdSQDs	2.3 ± 0.007^{fy}	0.25 ± 0.003^{ex}
Doxorubicin	9.7 ± 0.008^{gy}	4.8 ± 0.027^{gx}

Values are represented mean ±SD, Means of growth inhibition without a common letter differ significantly (P<0.05), a,b,c,d,e,f,g shows differences per row and x ,y shows differences between different concentrations.